Silica antireflection coatings with a tailored refractive index for applications of optics and photovoltaics

Yang Liu

A thesis in fulfilment of the requirements for the degree of

Master of Engineering

UNSW

School of Materials Science and Engineering

Faculty of Science

September 2019

THE UNIVERSITY OF NEW SOUTH WALES

Thesis/Dissertation Sheet

Surname or Family name: **Liu**

First name: **Yang**

Abbreviation for degree as given in the university calendar: **Master**

School: **Materials Science and Engineering** Faculty: **Science**

Title: Silica antireflection coatings with a tailored refractive index for applications of optics and photovoltaics

Abstract 350 words maximum:

The antireflection (AR) coatings are of technological importance for applications in optical, electrochemical and sensing devices, however, good performance is restricted to the precise control of the nanoscale structure to suppress the reflection. The applied structures that have been investigated so far are featured by porosity, surface pattern and gradient distribution in the refractive index, but they remain a challenge in large scale fabrication. In this work, an investigation of highly uniform and porous silica AR coating has been systematically presented, and the recent advances of AR technology have also been summarized, including the basic principles of antireflection and its possible applications. A systematic study was carried out to investigate the effect of catalyst and aging time on silica particle size and distribution. It was found that the silica particle size can be tailored well between 9.8 to 91.0nm by the control of the ammonia catalyst ratio. Moreover, to determine the optimal size based on the sol-gel process, a comparative study of the particle effect on the AR properties was undertaken. Where capillary stress was determined to be the dominating factor of the particle assembly, and the refractive index of silica coating was adjusted from 1.16 to 1.47. Based on the current mechanisms of the antireflection and theoretical calculations, two sizes of silica sphere (56.2 and 91.0 nm in diameter) were selected as the main component of the AR coating layer. A peak transmittance achieved 99.57% at the wavelength of 550nm with an average of 98.18% over the visible range (380-800nm). Furthermore, the combination of nano porous AR coatings and the surface pattern on the solar cell covered glass showed vast improvement in the glass transmission efficiency over a wide-angle of incidence ranging from 0 to 68°. The enhancements in the photovoltaic system output efficiency are ≈ 2.5%, as estimated by a comprehensive calculation considering the net effect from transmission spectra, the AM1.5 solar radiation spectrum and silicon solar cell external quantum efficiency spectrum. A freeze test and accelerated weathering stability test showed the strong resistance of the AR coatings which suggests great potential for commercial applications.

FOR OFFICE USE Date of completion of requirements for Award:

ONLY

ORIGINALITY STATEMENT

‘I hereby declare that this submission is my own work and to the best of my knowledge it contains no materials previously published or written by another person, or substantial proportions of material which have been accepted for the award of any other degree or diploma at UNSW or any other educational institution, except where due acknowledgment I made in the thesis. Any contribution made to the research by others, with whom I have worked at UNSW or elsewhere, is explicitly acknowledged in the thesis. I also declare that the intellectual content of this thesis is the product of my own work, except to the extent that assistance from other in the project's design and conception or in style, presentation and linguistic expression is acknowledged.’

Signed.....

Date.....

INCLUSION OF PUBLICATIONS STATEMENT

UNSW is supportive of candidates publishing their research results during their candidature as detailed in the UNSW Thesis Examination Procedure.

Publications can be used in their thesis in lieu of a Chapter if:

- The student contributed greater than 50% of the content in the publication and is the "primary author", ie. the student was responsible primarily for the planning, execution and preparation of the work for publication
- The student has approval to include the publication in their thesis in lieu of a Chapter from their supervisor and Postgraduate Coordinator.
- The publication is not subject to any obligations or contractual agreements with a third party that would constrain its inclusion in the thesis

Please indicate whether this thesis contains published material or not.

☒ *This thesis contains no publications, either published or submitted for publication (if this box is checked, you may delete all the material on page 2)*

☐ *Some of the work described in this thesis has been published and it has been documented in the relevant Chapters with acknowledgement (if this box is checked, you may delete all the material on page 2)*

☐ *This thesis has publications (either published or submitted for publication) incorporated into it in lieu of a chapter and the details are presented below*

CANDIDATE'S DECLARATION

I declare that:

- I have complied with the Thesis Examination Procedure
- where I have used a publication in lieu of a Chapter, the listed publication(s) below meet(s) the requirements to be included in the thesis.

Name	**Signature**	**Date (dd/mm/yy)**

Postgraduate Coordinator's Declaration (to be filled in where publications are used in lieu of Chapters)

I declare that:

- the information below is accurate
- where listed publication(s) have been used in lieu of Chapter(s), their use complies with the Thesis Examination Procedure
- the minimum requirements for the format of the thesis have been met.

PGC's Name	**PGC's Signature**	**Date (dd/mm/yy)**

COPYRIGHT STATEMENT

Signed.....

Date.....

AUTHENTICITY STATEMENT

Signed.....

Date.....

ACKNOWLEDGMENTS

First of all, I would like to express my sincere gratitude and appreciation to my supervisor prof. Sean Li for taking me on as a master student. I learned a lot in every meeting with him, and his expertise in thin-film deposition field helped me all the way in dealing with all kinds of research problems. He is also a very supportive and patient person who generously offered help and guidance in all aspects during my Master.

I would also like to thank my co-supervisors, Dr. Danyang Wang, who kindly gave me useful advice on my student life. Thanks also to our technical staffs, who are Dr. Tan Thiam Tech Tan, Bill Joe, George Yang, Xi Lin, Soo Woo Chong, Jane Gao, for their time and efforts spent on training me to work safely in the laboratory. Special thanks go to members of Australian National Fabrication Facility, NSW Node, and Mark Wainwright Analytical Centre, they are Dr. Mark Gross, Dr. Gordon Bates, Dr. Ute Schubert, Dr. Katie Levick, Dr. Yin Yao, Dr. Qiang Zhu, Mr. Michael Zhi for their training and assistance in laboratory induction, Microscopes operation. Thanks to Ms. Kim Foster for her professional cooperation in all paperwork. Also, I would like to thank Dr. Yajie Jiang for her assistance in the operation of spectroscopic ellipsometry.

Over the last two years, I also received much help from my lovely groupmates. They are Mr. Yichen Liu, Mr. Wei Zhang, Mr. Shuangyue Wang, Miss. Junjie Shi, Miss. Mengyao Li, Miss. Nan Chen, Mr. Bo Qu, Mr. Wenxuan Wang. Thanks to Mr. Yichen Liu for his advice not only on research but more on life. Thanks to Belinda for being my deskmate. I feel lucky to be able to spend the lunchtime with Mr. Wei Zhang, Mr. Shuangyue Wang, and Mr. Hui Kong. I would also like to show my gratitude to Miss. Junjie Shi for her cooperation and accompany.

Lastly, I would like to deeply gratefully to my parents, my uncle, Miss Mingyi Liao and all the other family members for the prayers, love, patience, spiritual support, which helps me get through this journey.

Contents

List of Figures

List of Tables

List of Abbreviations

AR: Antireflection

RI: Refractive Index

SWS: Subwavelength Structures

MSE: Mean-squared Error

EMA: Effective medium approximations

Abstract

Antireflection (AR) coatings are of technological importance for applications in optical, electrochemical and sensing devices, however, good performance is restricted to the precise control of the nanoscale structure to suppress the reflection. The applied structures that have been investigated so far are featured by porosity, surface pattern and gradient distribution in the refractive index, but they remain a challenge in large scale fabrication. In this work, an investigation of sol-gel derived silica-based highly uniform and porous AR coatings have been systematically presented, and the recent advances of AR technology have also been summarized, including the basic principles of antireflection and its possible applications. The fabrication strategies based on polymer, inorganic, and hybrid organic-inorganic materials were also classified, and a systematic study was carried out to investigate the effect of catalyst and aging time on silica particle size and distribution. It was found that the silica particle size can be tailored well between 9.8 to 91.0nm by the control of the ammonia catalyst ratio. Moreover, to determine the optimal size based on the sol-gel process, a comparative study of the particle effect on the antireflective properties was undertaken. Where capillary stress was determined to be the dominating factor of the particle assembly, and the refractive index of silica coating was adjusted from 1.16 to 1.47. Based on the current mechanisms of antireflection and theoretical calculations, two sizes of silica sphere (56.2 and 91.0 nm in diameter) were selected as the main component of the AR coating layer. A peak transmittance achieved 99.57% at the wavelength of 550nm with an average of 98.18% over the visible range (380-800nm). Furthermore, the combination of nanoporous AR coating and the surface pattern on the solar cell covered glass showed vast improvement in the glass transmission efficiency over a wide-angle of incidence ranging from 0 to 68°. The enhancements in

the photovoltaic system output efficiency are ≈ 2.5%, as estimated by a comprehensive calculation considering the net effect from transmission spectra, the AM1.5 solar radiation spectrum and silicon solar cell external quantum efficiency spectrum. A freeze test and accelerated weathering stability test showed the strong resistance of the AR coating which suggests great potential for commercial applications.

Chapter 1 INTRODUCTION

1.1 Background

Reflection occurs at the interface between two different materials with refractive index difference. Some of them are useful, while some of them need to be avoided such like, the reflection happens on eyeglasses, solar cell glass, camera lenses, Light-emitting diode (LED) devices, display screen, et cetera. The theory of antireflection based on the destructive interference of the reflected light from the air-coating and coating-substrate interfaces [2, 3]. For the specular incident light, ideal homogeneous AR coatings need to satisfy two requirements: the thickness of the AR coating equal to $\lambda/4n_c$, where λ is the wavelength of the incident light, n_c is the refractive index(RI) of the AR coating; and $n_c=(n_a \times n_s)^{1/2}$, where the n_a and ns are the RI of the air and substrate respectively. A typical glass has a refractive index range from 1.45 to 1.65 in visible spectral range(380-740nm), which implies that the idea refractive index of the coating n_c is expected to be between 1.20-1.25. In the natural, the magnesium fluoride is known as the homogeneous one-phase material with the lowest refractive index of 1.35. To obtain lower refractive index, theoretically, there are two strategies, one is a fabrication of "moth-eye" surface[4, 5], an alternative solution is to introduce nanopore into the coating material to form a porous structure[6-8]. Based on these principles, AR coating fabrication has developed into a well-established yet very active field of research[9]. Harold Dennis Taylor found antireflection on lenses by acid etching[10] in 1904, since when the AR coating technology has been developing rapidly.

Current industrial AR coating technology relies primarily upon vacuum deposition techniques such as sputtering[11] or physical and chemical vapor deposition[12, 13]. For

sputtering deposition, the substrate will need to bearing high temperatures, which depends on the target materials; this factor limits the range of choice in deposition material and applied substrate[14]. The physical vapor deposition has been developing for the application on advanced optical lens coating, and it is also the most applicable and acceptable approach to realize high-accuracy control of multilayer coating. However, these AR coating technologies are most often used for small size application considering their complicated serial treating processes and expensive instruments. For example, the company Edmund Optics sells a square AR coated N-BK7 window glass with 10 mm side length for about 76 AUD[15]. Therefore, the cost is the primary barrier to large-scale AR production. The sol-gel combined dip coating process is the standard and economical way to produce AR coating as it is possessing the right balance between performance and cost [13,14]. In addition, the sol-gel combined dip-coating method has other advantages in AR technology field: With the strong inclusivity, additives such like polymer PEG-200[16], Pluronic F127[17, 18], CTAB[19], Polypropylene oxide[20], poly(propylene glycol)[21], HDMS[22] can be facilely involved into the sol-gel system and play role as pore generator, surfactant, dispersant, binder and further to achieve lower the refractive index of the coating or improvement of mechanical performance; A nano-porous structure formed after the sol-gel derived particles stack on the substrates during the dip-coating process consequent by the evaporation induced self-assembly behavior [23]. In addition to MgF_2, the most commonly used dip coating material also includes SiO_2 (n=1.46), which performs better on mechanical properties and weatherability[3].

1.2 Challenge

The application of sol-gel combined different coating process has been widely used for the preparation of single- or double-layer antireflective coating on different substrates. However, most of the optical system, such as eyes glasses, camera lens, et cetera, require multilayer AR coating to realize high transparency over a wider incident angel and also safe durability. The sol particle self-assembly behavior during the wet coating process is influenced by many factors including the chemical parameters (e.g., initial soil composition, pH, aging time) [24] and the processing ones (e.g., partial vapor pressures, convection, temperature, relative humidity[25]). The uncontrolled particle assembly creates many problems like non-uniformity, insufficient bond strength, crack, shrinkage, etc., and these problems have impeded the development of sol-gel process on fabricating AR coating with high aspect ratios over large areas. For dip coating process, the gradient solvent evaporation rate and capillary pressure lead to the thickness irreproducibility during the large-scale production[26], and also the film shrinkage induced by capillary pressure and ions interaction force cause the strong fluctuation of the refractive index[27]. Accordingly, the major challenge and also potential opportunity for sol-gel combined dip-coating process application on optical coating felid are how to realize high accuracy control of multilayer deposition based on the understanding of particle assembly and find an optimal match among the materials considering the practical use.

1.3 Thesis outline

Our work tackles the challenge of preparing highly uniform, large scale AR coating based on the systematic study of the sol-gel chemistry and particle assembly during the coating process. AR technology and new process have been reviewed in chapter 2, and chapter 3 gave the detail experimental procedure and applied characterization technologies. Chapter 4 presented the study of sol-gel process in preparation of silica sol with varying parameters, including catalyst and aging time. Chapter 5 introduced the simulation results based on the Bruggeman Effective Medium Approximations (EMA) dispersion models. Based on the experimental and simulation results in previous chapters, sol-gel combined dip-coating derived single layer silica coating on soda-lime glass with excellent AR performance has been comparatively studied in chapter 6. The characterization of the particle size effect on the film structural evolution during the dip-coating process and the antireflective performance of the coating were assessed by combining various techniques including spectroscopic ellipsometry measurement, VASE32 software optical simulation, and other electron microscope observations. In Chapter 7, the silica AR coating was applied into the solar cell cover glass to achieve higher output efficiency, and the durability of the coating was evaluated by accelerated-aging test in a humidity chamber, freeze test. The last chapter 8 assess and summarized the main results of this topic. The conclusion pointed out the limitation and advice in this work and research prospect were given to improve the current practice in AR technology.

Chapter 2 LITERATURE REVIEW

2.1 Introduction

The antireflection technology has gone through a long period of more than one century so far. AR coatings have been widely studied and can be mainly divided into three groups: Polymer-based, organic-based, and Organic-inorganic hybrid based as well. In the early time, MgF_2 was regarded as an ideal candidate material, having the lowest nonlinear refractive indices among the existing optical material, for the fabrication of the AR coating.[28, 29] A promising alternative to MgF_2 is porous SiO_2, which might be deposited cost-effectively onto large areas and which features a low refractive index that can be varied between 1.10 and 1.46 via the porosity of the films. Xi et al. [13] achieved the adjustment of the refractive index of the TiO_2 nanorod layer, which ranged from 2.7 to 1.3 by Oblique-angle deposition, and near-perfect antireflection was achieved by the graded-index layer consisting of TiO_2 layer and SiO_2 layer. Alternatively, the subwavelength structure (SWS) has been adopted to create the graded refractive index and minimize surface reflections, Bernhard discovered that. [30] Not only that, board band and Omnidirectional antireflection can be realized via the building of SWS.[31] The organic polymer materials[5, 8, 32-47] attracted much attention to the fabrication of SWS based AR coating due to their good mechanical and optical properties, lightweight, and flexibility. Poly (methyl methacrylate) (PMMA) is a typical material which has been extensively applied to the fabrication of a transparent layer in a variety of optics and optoelectronic devices. Gan et al. [44] fabricated the PMMA-coated graphene as transparent conductive electrodes, resulting in G/Si solar cells with excellent PCEs of more than 11.12% after HNO_3 doping. Choi and Park et al.[5] realized a high AR

performance on PMMA with the formation of nano-tailed SWS. However, it is still significant challenges for polymer-based AR coatings' outdoor applications due to the ultraviolet degradation and thermal incompatibility between coating and substrate. Recent years, hybrid organic-inorganic materials offer a creative conception of optimizing the properties of AR coatings. Schulz et al. [48] fabricated AR coating comprising inorganic layers and organic nanostructure and achieved wideband antireflective property.

The etching process is used initially to produce porous AR coatings. Acid treatment is the most commonly used and can be traced back to 1887.[49] After then, the deposition method has gradually replaced the old etching process because of the environmental constraints. Obtain AR coatings with broadband Antireflective Properties by depositing multilayer coatings were significant breakthroughs. Therefore, the deposition method entered a new stage of rapid development. Chemical vapor deposition (CVD),[12, 50-52] physical vapor deposition[53-56] were developed to prepare AR films with SWS. In the meantime, a sol-gel process combining different coating method (Dip coating,[57-60] spin coating,[44, 61, 62] spray coating[63, 64]) also attracted much attention. To obtain board band AR coatings, other methods such as laser interference lithography, electron beam lithography, nanoimprint lithography, et cetera, have been developed to prepare Nano-arrayed structures and SWS on the substrate.

Here review on the advances in study on antireflection technology offer insights on the potentialities and its challenges to practical application. The first segment briefly described the antireflection mechanism. We then presented the strategies to realize the antireflection and in details the structure of the AR coating. The third segment mainly focuses on different types of AR coatings, including polymer-based, organic-based, and Organic-inorganic hybrid-based, respectively. The fourth part presented the variety of fabrication technologies used to produce AR coatings and given a comparative study

among different technologies in the particular advantages or drawbacks. Also, there given a discussion of the AR properties in terms of the durability and reliability in practical application, and also introduced some related improvements. Finally, the practical applications of AR coatings such as windows glasses, solar collectors, and photovoltaic modules and display devices will be discussed (new function/application). The understanding of mechanism and summarization of current AR technologies defines the actual limitations of the technique, and brings forward the farther research work perspectives, in terms of improving the mechanical performance, to be environmentally friendly, and realize low-cost coating in large scale.

2.2 AR (antireflection) Mechanism

Reflection, the optical phenomenon, happens between the interface of two media with different refractive index (RI). The Fresnel equation offers the basic preliminary mathematical model of reflection and refraction. The condition for antireflection happened in the thin film/substrate system, as shown in Figure 1, can be deduced by the mathematical model [5], which based on the following assumptions:

- There is no absorption in the layers.
- Only consider one reflection from each interface.

The elimination of reflection occurs when the two reflected waves R1 and R2 satisfy a destructive interference. The conditions for this are the following:

- The phase difference, d (between two reflected waves) is $n\pi/2$.

- All the layers had an optical thickness (nd) of λ/4 where λ is the wavelength of the incident light.

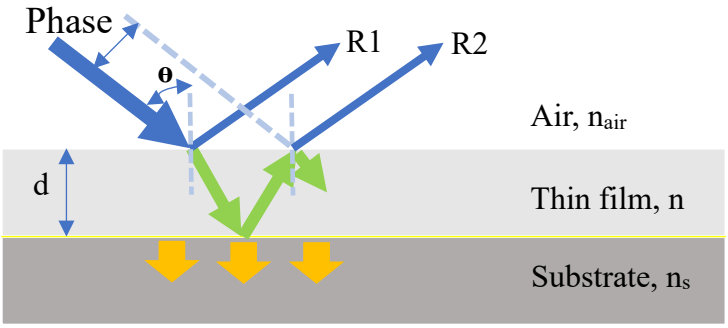

Figure 1. The transmit of light on single-layered film on a substrate (ns > n)

Based on the above two essential criteria, the equation governing phase difference is $d=2\pi n_d \cos\theta/\lambda$. Thus, we get θ=0, which is represented by normal incidence. The reflectance at the interface between two layers as follows,

$$R=\left[\frac{n_{air}n_s-n^2}{n_{air}n_s+n^2}\right]^2 \quad (1)$$

Where n, n_{air}, and n_s are the refractive indices of film, air, and substrate, separately. For the reflectivity R to be zero, the index of coating must satisfy the condition $n=(n_{air}n_s)^{1/2}$. This result was done based on a single layer on the substrate. However, even when the R is zero, it is only achieved at a specific wavelength because the refractive indexes of the single-layer film are all the same. Therefore, the elimination of reflection only happens at a specific wavelength. According to optical theory,[3] the antireflection happened in the multi-layered ARC must meet several conditions:

- All the layers had an optical thickness (nd) of λ/4, where λ is the wavelength of the incident light.

- The reflective indices of all layers should decrease gradually from the substrate to the air.

2.3 Strategies and Structure

2.3.1 Strategies

As we mentioned in the above section, a zero reflectance for a single film is only achieved when meeting the index of the coating (n_c) equal to the square root of the index of the substrate (n_s) and the surrounding medium (n_0). Consequently, for an AR film at the interface between the substrate and the air, the refractive index should in the range of 1-n_s. However, due to the limitation of the available low-refractive materials, especially in the optical films with a refractive index less than 1.3. [3] One solution to lower the index of the film is to introduce porosity to it, that is, this homogeneously distributed pores, which size is far below the wavelength of light, will suppress light scattering. To achieve such porous structures, many approaches have been developed, including phase separation and etching processes,[4, 32, 33, 65] oblique angle deposition,[53-56, 61, 66, 67] sol-gel techniques,[43, 57, 68-70] and sacrificial organic pore generators (e.g., dendrimers and amphiphilic block copolymers).[71-75] For the convenient single layer AR film, however, an effective reflectance is typically limited to a small range of incident angles and a narrow wavelength. An alternative solution of eliminating reflectance is to achieve a gradient of refractive index (GRIN) in the coating film, and it can impart ultra-broadband and omnidirectional antireflection to an interface. There are three main ways –precisely controlled thickness of each layer to realize a destructive interface or treating the film surface to form periodic subwavelength structures(SWS), which take inspiration

from the nanostructure of the corneal lenses found in moth eyes.[4, 76-78] However, the multilayer AR coatings often deteriorate over time on account of thermal mismatch and poor adhesion.[36] In contrast, the single component and integration make SWS more robust. There are a variety of such textured structured mimicking the moth's eye, including Nanorods, Nanotips, Nano-grass, Nano-cones, et cetera., have been fabricated through different methods, which are reactive ion etching (RIE) processes,[76, 79, 80] lithography,[77, 78, 81] electron-beam evaporation,[53, 82] template method,[83, 84] Hydrothermal growth method.[85]

2.3.2 Structure

Normally, AR coatings are made of Inorganic materials with the refractive index close to the value of the square of the $\sqrt{n_i n_s}$ (where n_i and n_s are the refractive indices of the incident medium and the substrate, respectively), or alternatively the subwavelength structure, including the porous structure and nanostructure-arrayed surface (moth-eye structure).[86, 87] In early time, people mainly used the etching process to fabricate the AR film, particularly on the glass. To obtain low reflectance over broad wavelength regions, alternative concept, depositing inorganic materials (MgF_2, TiO_2, SiO_2) to form a thin film as an AR coating, was appeared with the research on the inorganic materials and the development of technology in the deposition process. The refractive index of Porous SiO_2 thin films can be adjusted between 1.1 and 1.5, which allows the deposition of single or multilayer antireflection (AR) coatings even on material with a low refractive index such as glass. There are some studies[88, 89] demonstrated that deposit a porous SiO_2 thin film on glass can reduce by 4% reflection at the air-glass interface, therefore increasing the amount of light transmittance and lowering the reduction effect. Apart from

the porous SiO_2 thin films, the excellent AR performance also be realized by the nanostructure-arrayed silicon, such as Silicon Micropillar Arrays,[80] Silicon Nanorods,[82] Silicon Nanotips,[31] Pyramid arrayed silicon,[90, 91] shown in Figure 2.

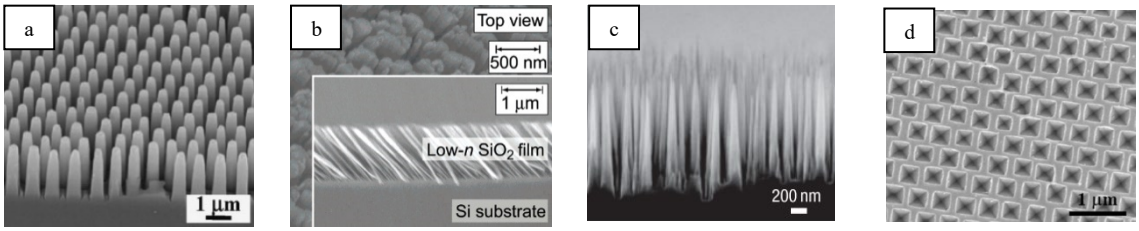

Figure 2. The SEM image of (a) silicon Micropillar Arrays, [80] (b) Silicon Nanorods, [82] (c) Silicon Nanotips, [31] (d) Pyramid arrayed silicon. [90]

MgF_2 has been attractive internationally in the field of AR coatings as its low refractive index (1.38).[92] Recently, Dhadala Karthik et al.[59] synthesized ink-bottle mesoporous MgF_2 nanoparticles via a deformation-reformation route from rough commercial MaF_2 hydrate powder and obtained nearly 100% transmittance within visible range (615–660 nm), average transmittance of 99% and 97% in the visible (400–800 nm). This simple synthesis approach of MgF_2 nanoparticles and AR coatings formation have excellent repeatability and are very suitable for the production on a mass scale. To date, various inorganic materials as AR coating have been developed to match different substrate, the Table 1 summarized the typically used materials such like MgF_2[92], CaF_2[57], SiO2[53, 65, 93, 94], Si[90, 95], TiO_2[13], ZnO[96], Indium Tin Oxide(ITO)[55] et cetera..

Table 1. The materials usually used to fabricate AR coatings.

Reference	Structure		Materials	Refractive index	Substrate	Method	Wavelength, nm	Transmittance	Reflectance
[92]	Single layer	Mesoporous	MgF2	1.23	Glass	Sol gel	500-600	99.40%	~0.24%
[57]	Single layer	Porous	CaF2	1.37	Float glass	Sol gel	600	98.4-98.7%	
[53]	Single layer	Nanorod	SiO2	1.08	Silicon	Oblique-angle deposition			
[93]	Single layer	Porous	SiO2	1.39	Glass	Sol gel	500	97.50%	
[94]	Single layer	Mesoporous	SiO2	1.28	Glass	Sol gel	590		0.07%
[96]	Gradient layer	Nanorod arrays	ZnO	~1-2.0	Silicon	Chemical solution deposition	400-1200		6.6% (Weighted
[90]	Gradient layer	Pyramid arrays	silicon	1.0-1.7	Silicon	Chemical etching process	600		<2%
[65]	Gradient layer	Porous	SiO2	~1.07-1.52	Patterned PV glass	Chemical etching process	380-1180	99.03%	
[95]	Gradient layer	"Moth eye"	silicon	~1.0-3.5	Silicon	Plasma-reactive ion etching	400-1000		<1%
[55]	Gradient layer	Nanorod	ITO	1.17-1.29	Silicon	Oblique-angle deposition	250-2000		<2%
[13]	Gradient layer	Nanorod Nanorod	SiO2 TiO2	1.05-1.27 1.67-2.03	AIN (n=2.05)	Oblique-angle deposition	574-1010		<0.5%

2.4 Materials

2.4.1 Polymer-based

A Polymer is a large molecule, or macromolecule, composed of many repeated subunits. The polymer film nanostructure can be obtained by adjusting the molecular-level structure, secondary structure (aggregation structure), and tertiary structure (self-assembly or self-organization) based on their micro-phase separation, self-assembly, or self-organizing properties.[97] In 1976, T. Wydeven and R. Kubacki[98] presented to use perfluorobutane-2 monomer to prepare single antireflection films by plasma polymerization, the monomer has the refractive index of 1.39 at wavelength λ=589.2nm, made them potentially attractive antireflection coatings for polymethylmethacrylate (PMMA) substrates, which have a refractive index of 1.49 at 589.2 nm. Afterward, to optimize the polymer-based antireflection film to work in more range of wavelength and broader angle, people focus more on the nanostructure and topography of the film. The property of antireflection of such polymer films mainly results from the subwavelength structure (SWS) with periodic arrays which are shorter than the visible wavelength, and these textured structures lead to a continuous transition of refractive index from air to substrate. To date, many approaches to fabricate such textured antireflection films have been explored, including phase separation,[39] etching processes,[99] interference lithography,[100, 101] electron beam lithography,[102] and colloidal lithography.[103] Recently, a promising technology to fabricate SWSs is roll-to-roll UV nanoimprint lithography[45] where a pre-fabricated mold with an inverse of the desired patterns is pressed onto a resist-coated substrate to replicate pattern via direct mechanical deformation. UV imprint is capable of fabricating nanostructures on the polymer substrate surface. However, if vacuum condition cannot be satisfied during both processes, air may

be trapped in the cavity, which will result in bubble defects. Injection molding, an industrially established technique, is capable of replicating micro/ nanostructures on polymer surfaces without air entrapment.[104-109] In the meantime, rapid fabrication of antireflective pyramid structure on polystyrene film combining electroless plating, electroplating, and microinjection compression molding has been reported.[46]

Polymer-based materials have great practical value and broader applications in the fabrication of AR coatings comparing with inorganic materials because they are flexible enough to adhere to the substrate and can be made in large-area. However, incompatible mechanical and thermal properties of polymer antireflective surfaces and their durability pose major operational challenges for outdoor applications. For the coated polymers, the main challenge is the crack initiation sensitivity of coatings results from a mechanical and thermal incompatibility between the organic-based substrate and hard, brittle polymer-based material, this may results in polymer contraction and form the polymer islands (de-wetting[110]), which will deteriorate the AR performance.

2.4.2 Organic-inorganic hybrid

With the development of soft inorganic chemistry processes, organic-inorganic hybrid materials have received considerable attention. The broad definition of them is molecular or nano-composites, a mixture of inorganic and organic components, where at least one of the component domains has a dimension ranging from a few angstroms to a few tens of nanometres.[111-114] Organic-inorganic hybrid materials play a significant role in improving the broadband antireflection performance of optical elements. Kevin C Krogman et al.[35] presented a facial method of using aqueous colloidal dispersions of

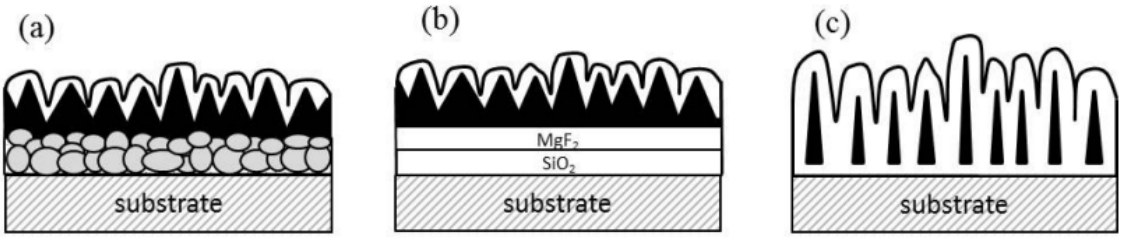

Figure 3. Advanced broadband AR coatings on glass: (a) two textured organic layers on the glass; (b) Combination of Inorganic layers with an organic nanostructure; (c) Embedding Organic nanostructure into inorganic material. [48]

metal oxide nanoparticles to fabricate AR coatings stacks on plastic substrates, the highlight of the approach is the graded concentrations of metal oxide nanoparticles on the film can tailor the refractive index of the polymer film over a wide range. Colorless polyimide-silica and polyimide-titania hybrid thin films have been synthesized successfully by the combination of the organic polymer (silane coupling agent) and nano-sized inorganic precursor, which can suppress the thermal expansion coefficient, and generate a controllable refractive index.[115] Schulz[48] fabricated AR Coatings on glass comprising the inorganic layers and organic nanostructures, as shown in Figure 3. In this way, the air-substrate index layers are decomposed into smaller and smaller steps. Therefore, the original uniform film with a single refractive index becomes a gradient

film with a continuous refractive index, and this film exhibits broadband antireflective properties from 400 nm to 1200 nm. Graphene has been a research hotspot for several years since the Nobel Prize for Physics, 2010 was awarded to Andre Geim and Konstantin Novoselov. Recent research presented that directly use Polymer-coated graphene films as transparent electrodes in G/Si solar cells can enhance the absorption of light. More notably, power conversion efficiencies of Polymer-coated graphene can reach up to 13.34% after HNO_3 doping.[44]

2.5 Performance and Improvement

AR films have been widely applied into optical fields, particularly in solar power generation, thus, apart from the low refractive index, an ideal AR film should also satisfy series condition from the aspects including durability and reliability.

Hardness and adhesion reflect the durability of the AR films. Even scratch to the surface or interior will affect its final antireflective properties. The films should meet enough abrasion resistance and have excellent adhesion with the substrate in order to prevent the film from mechanical damage scratch. For the porous AR films, however, it is hard to keep a balance between high transmittance and good mechanical properties because of their poor hardness and low abrasion resistance. As early as 1947, Moulton[116] found that adding a soluble siloxane binder to a silica suspension can enhance the abrasion-resistance of colloidal silica AR coatings. Besides, Philippe F. Belleville et al. [117] demonstrated that ammonia-treatment could improve the abrasion-resistance of colloid-based porous silica AR coatings. Nowadays, more flexible AR coatings have shown their tremendous potential for low cost electronic and photovoltaic devices. In 2006, Zhizhong Wu et al. [37] successfully fabricated porous silica-based AR coatings on the surface of

thin, flexible Poly(dimethylsiloxane) membranes. This AR coating can keep good durability during and after substrate deformation, even after multiple deformations–relaxation cycles. Recently, Kostantinos Kourtakis et al. [118] developed a novel method of combining fluoroelastomer with silicon oxide nanoparticles to fabricate AR coatings, which is mechanically robust and extremely scratch-resistant. A scratch adhesion test on two fluoroelastomer layer, one without the silica nanoparticle and the others have. The result indicated that the film without the nanoparticles appears delamination when the load up to 2 mN, while the film with nanoparticles does not fail until a much high load of 20 mN. The abrasion resistance of the film benefits from the bilayer structure, which is formed when nanoparticles with an olefinic alkoxysilane are introduced.

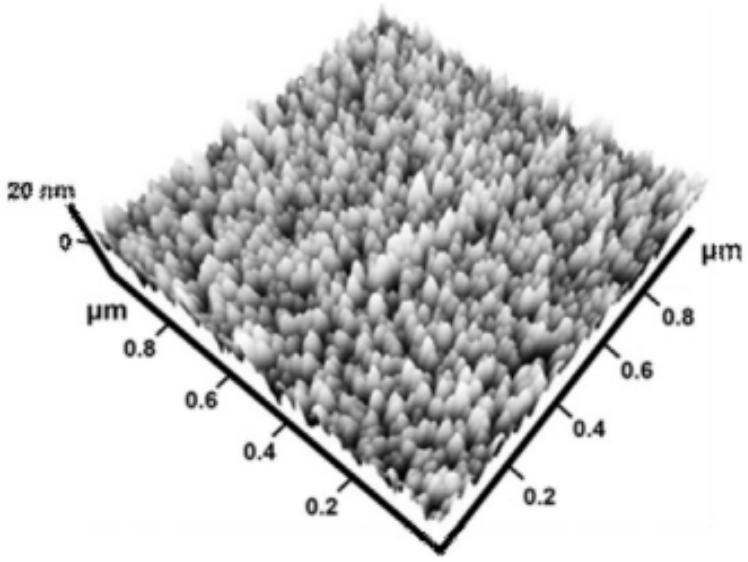

Figure 4. The 3D AFM images of silica nanoparticles coated glass slides. [51]

As the low mechanical durability of Sol-gel derived SiO_2 antireflection (AR) coating, the alternative material has been considering replacing the amorphous SiO_2, such as zeolite. Chen et al. [119] used aggregated zeolite nanoparticles as skeleton and zeolite precursors as binder synthesized AR coatings with more than 6H pencil hardness via a steam processing.[120, 121]

The AR films are widely used in outdoor, therefore, in addition to possessing qualified strength and abrasive resistance, the contamination resistance and the function of antifogging are imperative to the durability and reliability of AR films. The fog formed from the condensation of the water vapor onto the surface of the transparent substrate will result in light scattering further weaken optical transmission. Accordingly, an antifogging and self-cleaning transparent silica-based AR coating has been fabricated by one-step chemical vapor deposition.[51] The antifogging property and high transparency benefit from the well-ordered silica nanoparticles, shown in Figure 4, which can magnify the hydrophilicity and suppress the reflection when the roughness reaches to 3.23nm. In addition, there are various methods, including solution-phase[122] and vapor-phase salinization,[123] ammonia-water vapor treatment[124] and fluorine modification[125] to fabricate contamination resistant AR coatings.

2.6 Fabrication technologies

As we already discussed in section 2.3, the strategies to realize antireflection include the formation of a porous thin film with low RI, creating periodic subwavelength structures with graded RI, et cetera. The fabrication technologies to execute those strategies can be broadly divided into two kinds: Additive bottom-up techniques and subtractive top-down (Figure 5).

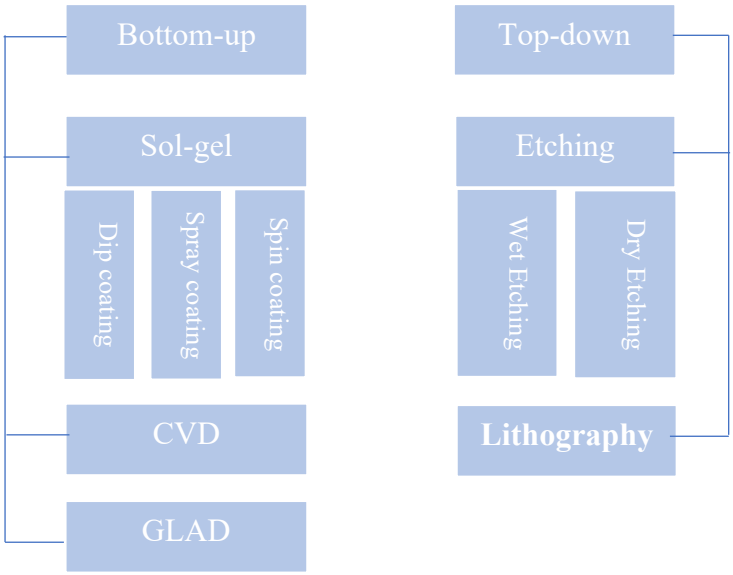

Figure 5. Fabrication techniques for AR coatings discussed.

2.6.1 Bottom-up approach

2.6.1.1 Sol-gel processing.

Typically, sol-gel processing can be introduced by using inorganic salts or metal alkoxides as precursor reagents, which when they are mixed with aqueous and catalyst hydrolysis and polycondensation reactions occur. The different reactions have been reviewed by Brinker and Scherer.[27] In general, the large area coating can be accessed by the combination of the sol-gel method with a different coating process such as dip coating, spin coating, spray-coating, lay-by-lay self-assembly (LBL). Traditionally, the

refractive index of sol-gel derived thin film is regarded as a uniform distribution due to the homogeneous structure. As a result, the ideal transmittance is achieved only at a specific wavelength in theory. However, Yao Xu et al. [126] fabricated sol-gel derived broadband antireflection silica AR films via dip coating and spin coating. SiO_2 particles and polyvinylpyrrolidone gradually distributed inside such film endow it with broadband anti-reflectivity, 315nm, and 559nm corresponding to dip coating and spin coating respectively. These coating processes for depositing sol-gels films will be discussed in brief below.

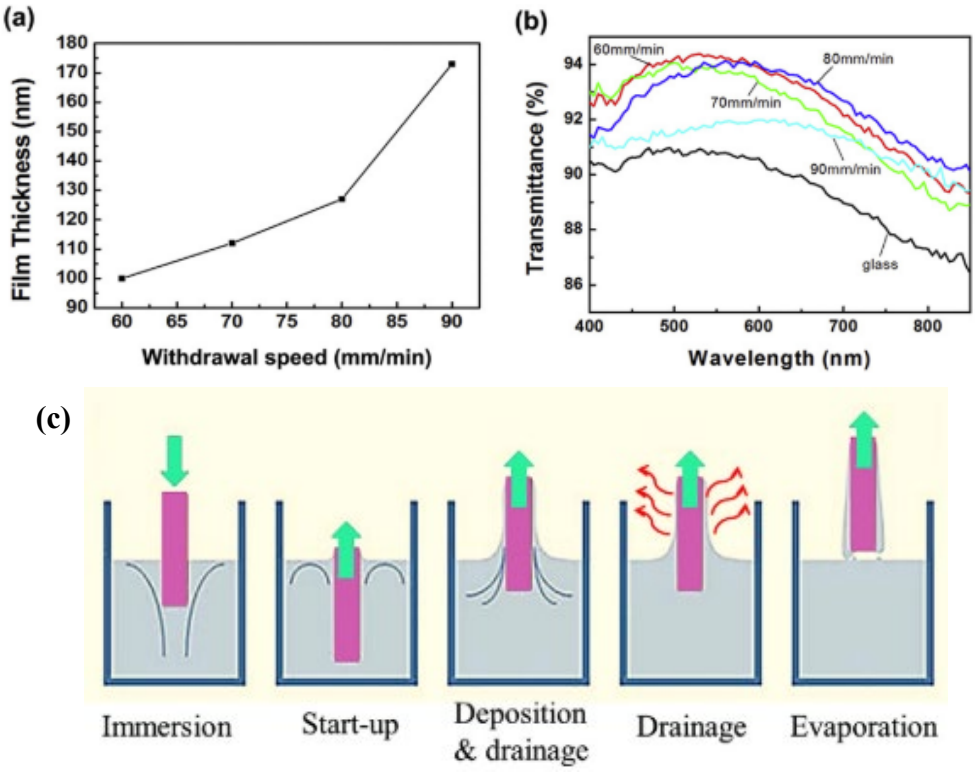

Figure 6. Effects of withdrawal speed on (a) film thickness and (b) transmittance. (c) The process of dip-coating. [58]

Dip coating. Many advantages contribute to its high adoption by an industrial coating process, including easy-to-use, saving raw materials, and uniform film formation.[93, 127] The steps in the process can be divided into five segments: immersion, start-up, deposition, evaporation, and drainage, as shown in Figure 6 c. The thickness of the film is adjustable

by changing the withdrawal speed during the dip-coating process.[27] Q.Z. Huang et al. [58] used dip-coating approach to prepared sodium water glass-based AR coatings. They demonstrated a strong positive relationship between the coating thickness and withdrawal speed, as shown in Figure 6a, as a result of the increasing viscous drag with faster withdrawal speed while larger viscous drag leads to the thicker deposited film.[27] However, thicker AR coating does not do good to antireflection performance because thicker film causes higher absorption. The Figure 6b tells that the AR coating with thickness of 127nm obtained by the withdrawal speed of 80 mm/min shows the best antireflection property.

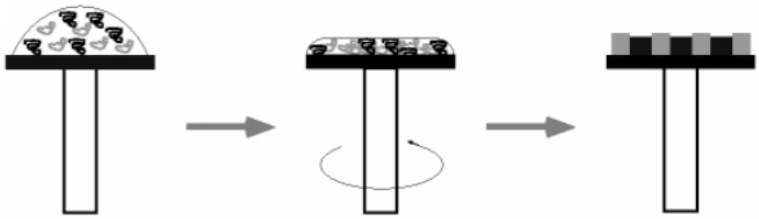

Figure 7. During spin-coating, phase separation sets in. [128]

Spin coating. It is a common method of preparing thin films on flat or marginally curved substrates. In the spin coating process, a small puddle of viscous film material is first deposited on the substrate and subsequently followed by the substrate spinning at the desired rotation speed. The puddle flows radially, and the excess spread to the edge of the substrate is owing to centrifugal centripetal force (Figure 7). The film continues to be thinner slowly until the film turns solid-like and reaches balance because of the rapidly increasing viscosity from solvent evaporation. An excellent expound of the fundamental theory of the spin-coating was given in a review by Stillwagon, L.E., Larson et al.[128] Stefan Walheim et al.[32] used a spin coating to accomplish phase separation and thus create porous films with high performance antireflection. The highlight of their method is the demixing of a binary polymer blend during spin coating (Figure 7). To date, the

spin coating method for fabricating AR film has been widely studied.[8, 44, 48, 61, 62, 103, 129]

Spray coating. Spray coating is quite a facile method, and there are no special requirements for the substrate. The method for preparing AR film has the advantage of a simple process, easily available material, non-vacuum system, and suitable for large-area

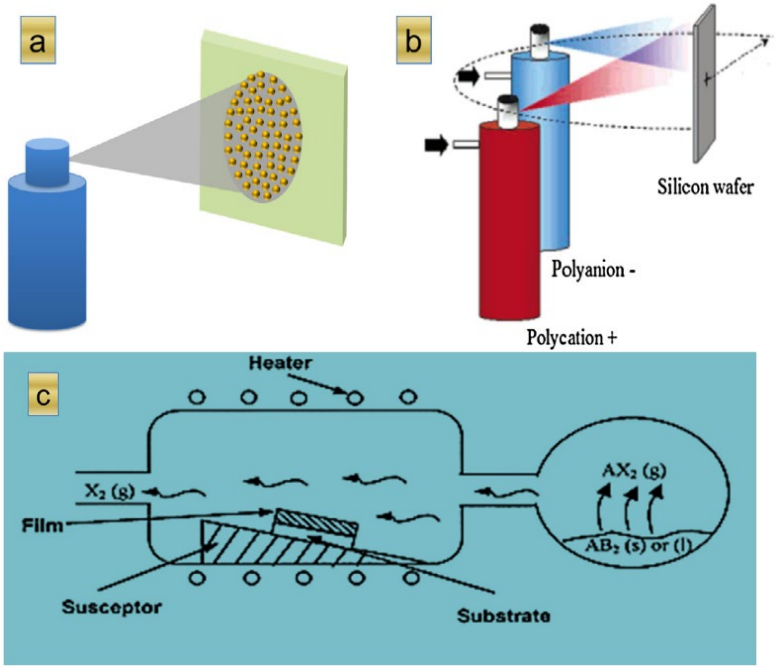

Figure 8. (a) Schematic illustration of the spraying process, (b) spraying process setup for the fabrication of multilayer coating [136], Copyright 2005 American Chemical Society. (c) Schematic diagram of chemical vapor deposition [137], Copyright 2003 Elsevier.

fabrication. The general process of spray-coating is shown in Figure 8a.[61] Compared with spin coating, the spray coating can form a denser film, because a thinner layer of the material is deposited at each deposition pass.[130] In addition, it is also practical for the fabrication of multilayer coatings with multiple components, as Figure 8b shows.[131]

2.6.1.2 Chemical vapor deposition (CVD)

The method is known as a chemical process that use one or more gas-phase compounds or elementary substance to react together on a specific substrate. It has been developed maturity and been applied to the semiconductor industry to produce thin films with high density, proper stoichiometry, uniformity. Generally, the process of CVD on a substrate to generate a film can be described as Figure 8c.[132] Recent years, plasma-enhanced chemical vapor deposition (PECVD) has been widely applied to preparing AR coatings in the industry. The creation of plasma of the reacting gases enables the deposition to

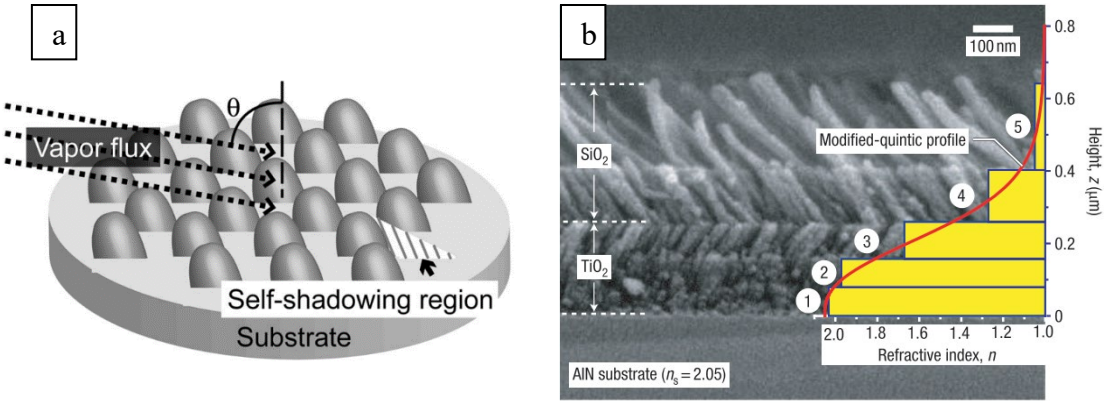

Figure 9. (a) Mechanism diagram of oblique-angle deposition. (b) the SEM image of the graded-index coating in section. [13]

occur at a lower temperature than that of standard CVD. Jian Yu et al.[133] have fabricated SiOx/tungsten-doped indium oxide (IWO) double AR coating for silicon heterojunction (SHJ) solar cell via PECVD. The Double AR coating shows an excellent performance over 500-1200 nm wavelength range. The impressive efficiency can reach up to 23.08% with high short circuit current density.

2.6.1.3 The glancing angle deposition (GLAD) technique

The Mechanism of the glancing angle deposition technique is shown in Figure 9a.[53] Basically, it belongs to physical vapor deposition (PVD) technique which is applied to

produce nanostructured thin-film materials with adjustable porosity.[134-137] This technique is featured by the tunable vapor flux incident angle, and an array of oriented rods with controllable porosity is obtained by self-shadowing effect and surface diffusion.[138] The relationship between the density of an obliquely deposited film and the incidence angle is given by Tait et al.,[139] Therefore, we can take advantage of GLAD and use the angle of incidence as a means of adjusting the porosity and hence the refractive index of the AR coating. Adjusting the vapor incident angle, J.-Q. XI et al. [13] found that the refractive index of a TiO_2 nanorod layer and SiO_2 nanorod layer can be controllably varied from 2.7 to 1.3, 1.46 to 1.05 separately. Moreover, they combined these two nanorods by GLAD and obtained a five layers coating with near-perfect antireflection characteristics on a one side-polished AlN substrate, which is shown in Figure 9b.

2.6.2 Top-down approach

2.6.2.1 Etching process.

The etching process can be recognized as a subtractive way that causes a selective dissolution or ablation of a surface or substrate. Fundamentally speaking, the etching process can be divided into two kinds: wet etching and dry etching.

Wet etching This process usually uses the water-based chemical solution as dissolution, and selective removing the soluble material can obtain the desired structure which is made by the undissolved material. Li-Qiang Liu et al.[65] proposed a creative two-step etching process to fabricate broadband and omnidirectional, nearly zero reflective photovoltaic glass. The etching agent using in the first step are low concentration acid (H_2SO_4, HNO_3,

HF), which reacted with Na_2O and CaO selectively and thus left pore inside the glass (see Figure 10). The uniform layer is dominated by nano-sized framework and pores (20–30 nm) (see Figure $10b_{2,3}$). During the second etching process, besides the corrosion of Na_2O and CaO, the etching of amount of SiO_2 from the SiO_2 skeleton play the dominating role in the creation of voids that decrease the size gradually along the etching direction, in turn, inducing a gradient in the refractive index. The final etching film is shown in Figure $10c_{1–3}$.

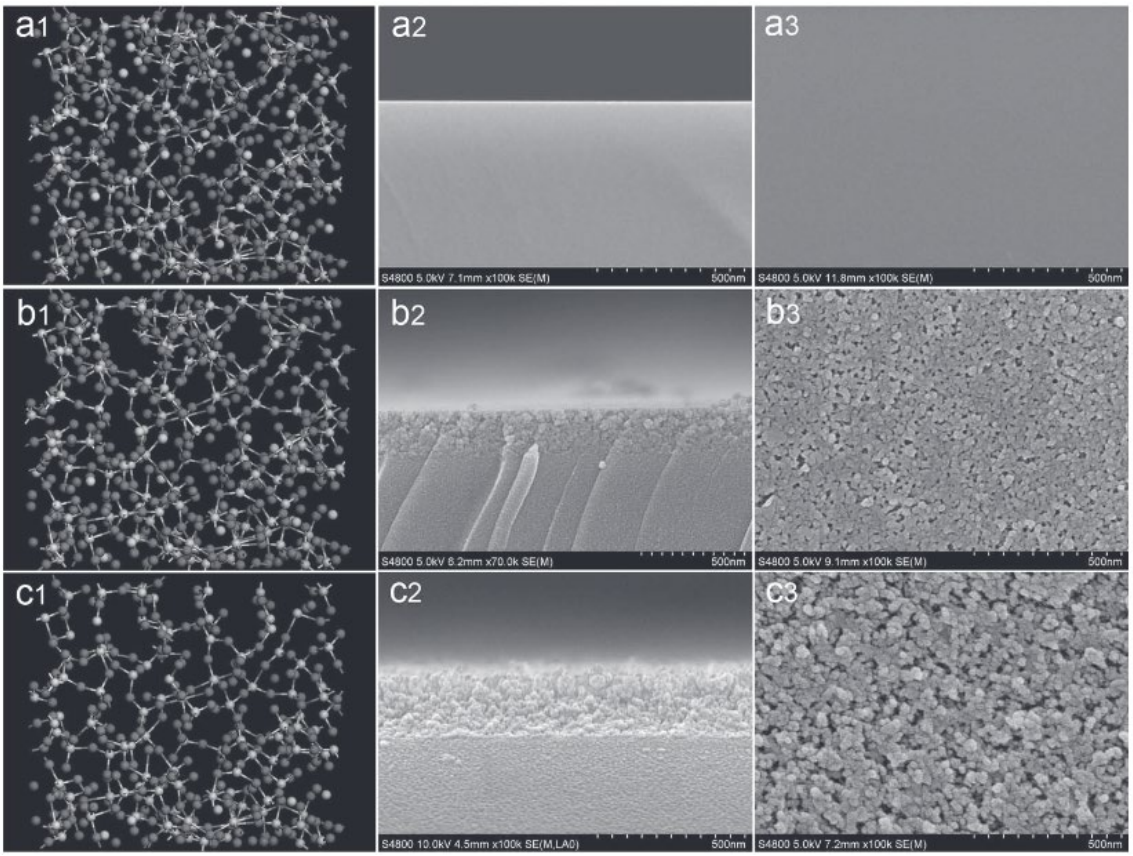

Figure 10. Skeleton (a1, b1, c1), SEM images of cross-sections (a2, b2, c2) and surfaces (a3, b3, c3) of the top layer of a PV glass layer. Original glass (a1-3); after first step etching (b1-3) and second step etching (c1-3). [65]

Dry etching works in a vacuum condition, and the surface removal is accessed by ablation or volatilization through the bombardment of ions (plasma of a reactive gas such as fluorocarbons, oxygen, et cetera..). The benefits of dry etching are low chemical hazard and contamination, and ease of process automation and tool clustering.[140] The plasma

etching is demonstrated for the fabrication of periodic nanostructured materials. Seulgi So et al.[47] prepared polymer poly (3,4ethylenedioxythiophene)(PEDOT) nanocone arrays with electrochemically modulated broadband antireflective properties by the oxygen plasma etching process. PEDOT nanocones, distributing homogeneously with a spacing of 200 nm and a height of 350 nm, exhibited a low broadband reflectivity of <1.5%

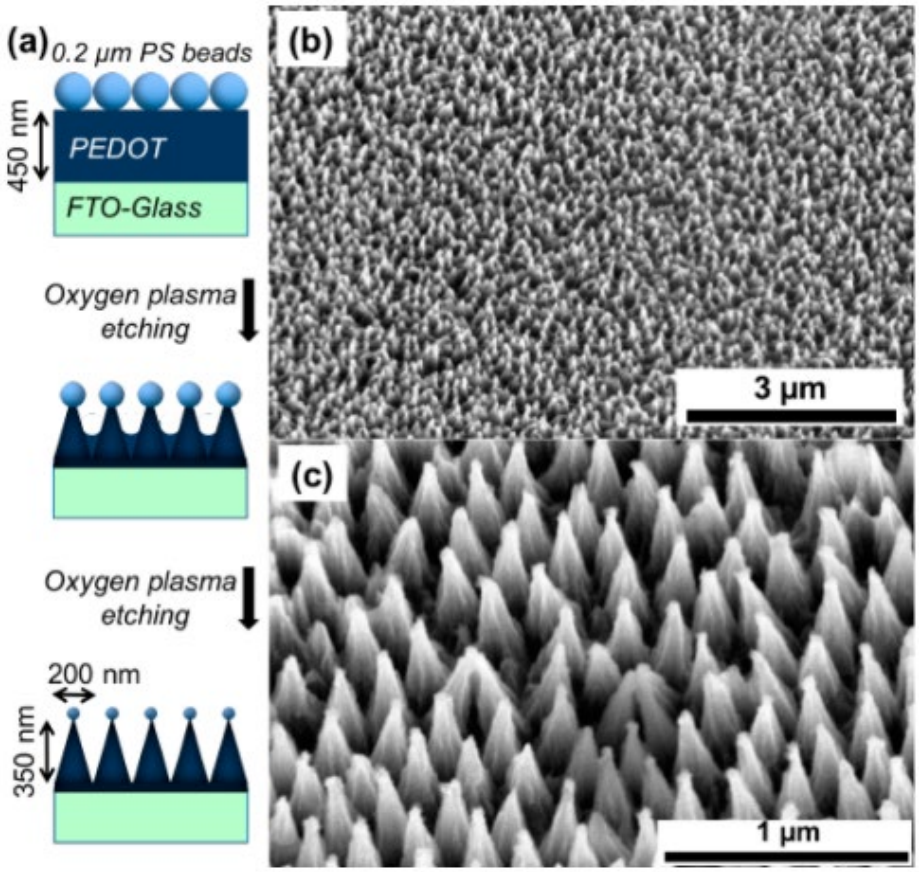

Figure 11. (a) The oxygen plasma etching of fabricating PEDOT Nano-cone arrays (height: 350 nm, spacing: 200 nm). (b) SEM image of PEDOT Nano-cone arrays (c) detailed SEM image of PEDOT Nano-cones. [47]

from 550 to 800 nm. The mechanism diagram for the fabrication of PEDOT Nano cone arrays by an oxygen plasma etching process is shown in Figure 11.

2.6.2.2 Lithography.

Patterning etching masks with nano-arrayed structures and SWSs can be achieved by lithography techniques such as laser interference lithography and electron beam lithography.[141, 142] However, the limitation of the e-beam lithography and laser beam lithography are the patterned area cannot be large as high manufacturing costs arising

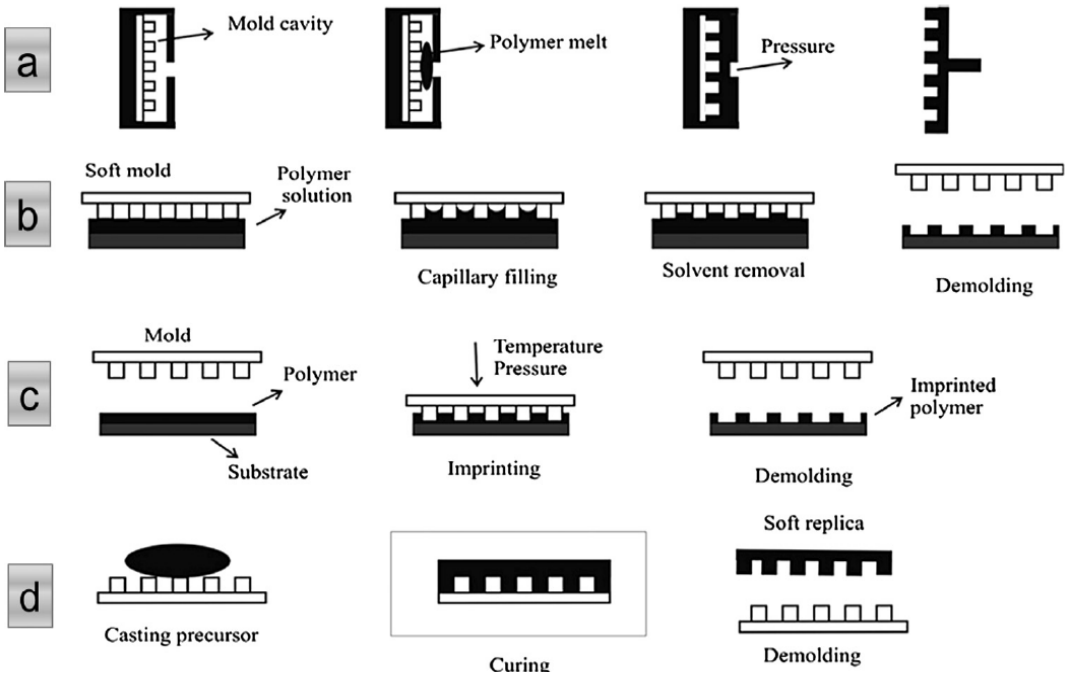

Figure 12. Available lithographic process for fabrication of SWS in large area.[148,149] (a) Injection molding, (b) solvent-assisted molding, (c) hot embossing, and (d) soft lithography, Copyright 2008 American Chemical Society.

from the need for sophisticated equipment. Afterward, low-cost lithography techniques, colloidal lithography were explored.[103] Nevertheless, the size of the nano-arrayed structures is difficult to control over a long-range, thus hindering the scaling up of this technology. Recent years, various lithography processes including, nanoimprint lithography,[45] soft lithography[143] based on molding, embossing, and printing have been developed to Pattern micro- and nanostructures. The mechanisms of some lithography approaches are shown in Figure 12.[144, 145] Cheng‐Hsin Chuang et al.[45]

developed a high-performance antireflection coating with SWSs via a roll-to-roll UV nanoimprint lithography. It has a reasonable prospect of industrialization as compared with other imprinting techniques because it is a continuous process adapting to patterning large area substrates, possessing significantly higher throughput.[146]

2.7 Applications

2.7.1 Architectural windows and glasses.

Multifunctional AR coatings are the development tendency in response to the diverse requirements such as selective AR, thermal transmittance, solar factor, and maintenance of glasses.[147] In daily life, benefiting from the high transmission, AR glasses play significant roles in various aspects, including building roofs, eyes glasses, shop windows, museum, and archaeological paths, et cetera. For instance, Schott's AR glass (Amiran) is produced by the sol-gel combined dipping process. The double-side coated Amiran AR glass possesses a very high light transmittance (~98%) in the visible range and 100 color rendering index (Ra). The glass possessing good AR performance and strong contamination resistance is developed to require the practical application. In 2001, Pilkington Glass first fabricated the AR self-cleaning windows, and it has great potential for big maintenance cost-saving, especially for tall buildings.[148] Usually, the self-cleaning modification on the glass is mainly realized by two ways, hydrophilicity, and photocatalysis, respectively. Inspired by the same principle, Saint-Gobain produced a self-cleaning glass named Bioclean, the coating on the glass consists of TiO_2 and other inorganic materials (SiO_2, MgF_2), the TiO_2 is known as hydrophilic and can decompose organic dirt and prevents mineral dirt from adhering to the surface of the glass when

exposing under the UV rays present in daylight. Hydrophilic surface means that when it rains, the water molecular has the priority to attach the glass surface and spreading over the surface without forming droplets, and the broken down dirty residues can be easily washed away.[149] However, there are also some limits on the available technologies, such as the durability of treated glasses when exposed to the external environment.

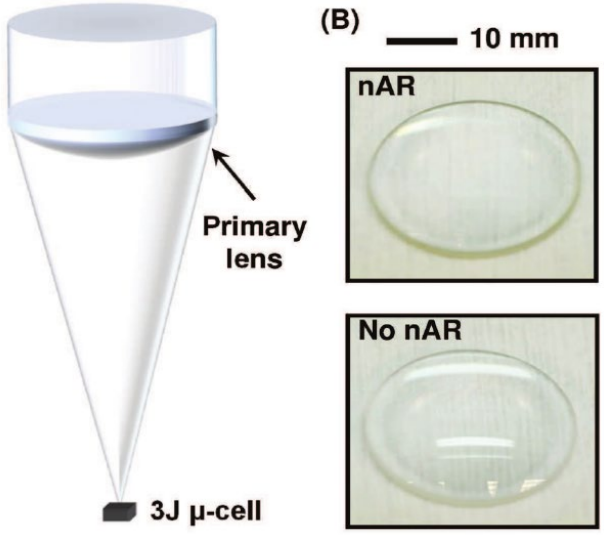

Figure 13. Primary plano-convex lens focusses the incident light onto 3J microcell. [7]

2.7.2 Solar collectors and photovoltaic modules.

The photovoltaic device such as solar cell produces a direct current of electricity when photons with enough energy interact with semiconductor and excite electrons into the conduction band. However, due to reflection, the visible light transmittance of low iron glass, commonly used for the photovoltaic cells, is only ~92%.[150] Therefore, the significance of antireflection coatings cannot be recanted in the solar cell fabrication process as it gives a necessary improvement in solar cell efficiency.[151] ZnS thin films have been widely applied as antireflection coatings for the solar cells,[152] The ZnS coated solar cell shows apparent improvement in spectral response and current-voltage curves.[153]

Recent advances have made concentration photovoltaics (CPV) technology increasingly attractive for utility-scale power generation. Contrary to conventional photovoltaic systems, the advanced systems have three main competitive advantages: less photovoltaic material requirement; less dependent on the immature silicon supply chain because of the availability of standard materials; high photovoltaic conversion efficiencies come from multijunction solar cells. However, the optical loose mainly comes from the Fresnel reflections has a negative effect on the performance of CPV. Take CPV modules made from Semprius factors for an example, and such losses are above 12% because of the presence of three optic/air interfaces.[154] Yuan Yao et al.[7] exploited the optimized bilayer AR coating onto lenses within CPV architecture improved photo-current by 8.2% from 3J microcells, as shown in Figure 13, employ the same 3J cells into CPV module with 35.5% energy conversion efficiency, the conversion efficiency is estimated to grow by 3 %.

2.7.3 Display devices.

Olifierczukol showed us how important is the elimination of harmful reflections in reflective TN displays.[155] He obtained the contrast ratio and luminance in on-state for a reflective TN display working in real conditions basing on a large amount of program has been worked out, the final results indicated that the application of AR films could increase the value of contrast ratio (CR) about four times. In the latest displays, the application of functional surface coatings with antireflective property is a standard solution. Also, the self-cleaning function may add new merits to the devices. For automotive display applications, to cut down the reflection on the surface of the instrument panel and to be more clarity and recognizable, typically, there require a curved

cover and a hood on the meter.[156] Automobile designers have been seeking a low reflection hoodless-type display, which is appropriate for various places on the dashboard. An ideal display should not only provide improved safety through quicker recognition by the driver but also have a more straightforward structure and lightweight. The further possible applications for AR coatings are expected to go in the direction of working on a flexible substrate. Therefore, the integration of super-hydrophobicity and antireflection into the surface is very desirable for various displays.

2.8 Summary

Nowadays, the antireflective films have been widely used in all fields of society, such as lenses, eye-glasses, military equipment, lasers, solar cells, diodes, multipurpose narrow and broad band-pass filters, cathode ray tubes, television screens, sensors for aeronautical applications, window glasses and anti-glare glasses for automotive applications and so on. The antireflection technology has gone through a long period more than one century so far, the significant progress of the development of antireflection technology has been summarized below:

Along with the increasing study of different materials and rapid development of advanced facilities. The preparation technology of AR coatings appears diverse and more economical and practical. The etching process is initially used to produce AR coatings, and now then the deposition method of fabricating thin films has gradually instead of the initial etching process considering the environmental problem. The high durability of deposited films to obtain AR which works well over broad wavelength regions by using multilayer coatings were essential breakthroughs. Therefore, the deposition method entered a new stage of rapid development. Chemical vapor deposition (CVD), physical

vapor deposition (such as glancing angle deposition) were developed to prepare AR films. In the meantime, a sol-gel process combining different coating method (Dip coating, spin coating, spray coating) also attracted much attention as the ability of coating in a large area. An alternative mature concept to AR coatings is employing SWS to the films. There are various nano-lithographic techniques has been applied to fabricate SWS, such as laser interference lithography, electron beam lithography, colloidal lithography, also including nanoimprint lithography, which has attracted lots of research recently. However, most of the fabrication technologies mentioned above are still limited to laboratory research and not suitable for industrial-scale production. One challenge is making mechanical properties satisfy for practical use because the mechanical wear on the surfaces could destroy the microscopic structures, resulting in a decline or complete loss of their optical property. Second, multistep procedures and harsh conditions adding cost. Therefore, in the near future, people should pay more attention to such research direction:

- Fabricating AR coatings with high mechanical strength and abrasion resistance by cost-effective techniques is the crucial point for large-area industrial production.
- Further improvement of current preparation technology considering the Environmental issues. Especially for organic-based approaches. Therefore, AR coatings are preferable for widespread use.
- Develope advanced materials and coating technology, which would enlarge the scopes of applications.

These challenges should be overcome for practical applications. Hence, more work needs to conduct the technical development and fundamental investigations of AR coatings in future work.

Chapter 3 Experimental procedure and Characterization technologies

3.1 Sol-gel process of preparing silica particle

Materials

Tetraethyl orthosilicate (TEOS, ≥99.0%, GC), Poly(ethylene glycol)(mol wt 200), Absolute Ethanol were purchased from Sigma Aldrich. Ammonia (30%) was purchased from Chem-supply, respectively. The coating substrate is a glass slide (soda-lime glass), which was cleaned by deionized water and followed by 15mins UV irradiation on each side.

Preparation of Catalyst Stock Solutions.

Catalyst stock solutions were prepared as follows; each base catalyst (30 wt% ammonia solution) was mixed with an amount of pure ethanol to lower the concentration to 15wt%. They were stored in a tightly sealed bottle to maintain their pH for a long time.

Synthesis of Silica Nanoparticles by sol-gel processing

The sol-gel processing can be divided into two stages or reactions: hydrolysis and condensation.[157] The synthesis of silica nanoparticle by the sol-gel process is generally accepted by the following process:

$$\equiv Si-OR + H_2O \rightleftharpoons \equiv Si-OH + R-OH \quad (1)$$

$$\equiv Si-OH + HO-Si\equiv \rightleftharpoons \equiv Si-O-Si\equiv + H_2O \quad (2)$$

$$\equiv Si-OR + HO-Si\equiv \rightleftharpoons \equiv Si-O-Si\equiv + R-OH \quad (3)$$

Where the eq 1 is the reaction of hydrolysis, and eq 2 and 3 represent for condensation, releasing water or alcohol. However, catalysis is required due to the low reaction speed, which is caused by the low polarity of the Si-O bond in silicon alkoxides[158]. Both

reactions can be catalyzed by base or acid[159]. Here, we use Ammonia (30%) as a catalyst, TEOS as a precursor and mixed with absolute ethanol, deionized water, then magnetically stirred for 1h at 45 degrees Celsius. After that, the solution was aged for different days to obtain sol. The synthesis of silica nanoparticle is illustrated by the flow chart (Figure 14).

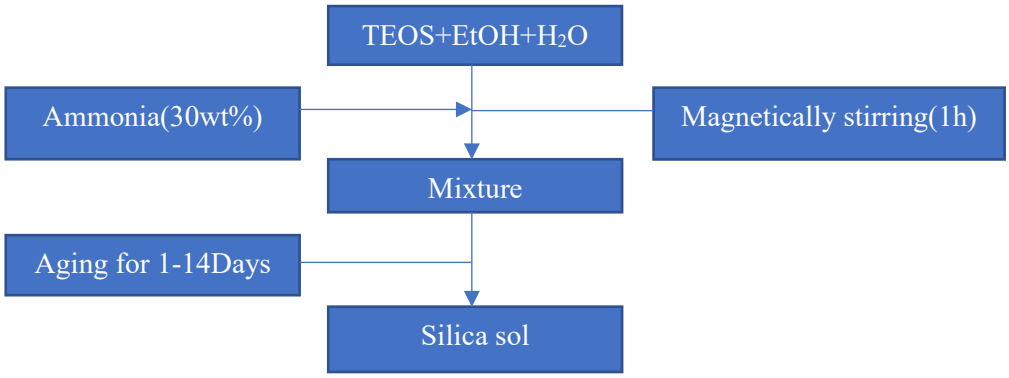

Figure 14. Procedure for preparation of silica sol.

3.2 The fabrication of thin film

As we mentioned in the above chapter, the dip-coating process generally has three stages: Immersion & dwell time, Deposition & Drainage, Evaporation. Substrate cleaning is one of the significant steps to ensure contiguous uniform film when in a deposition, the glass slide without adequate cleaning will lead to the discontinuous and non-uniform film. The cleaning process is the following: Firstly, the glass slides were clean by ethanol (100%) and followed by DI water with ultrasonication for 15 mins. Secondly, heat the prewashed glass slides at 100 degrees for 15mins. Last steps, we have two choices, one is to transfer the heated glass slides into UV oven for 30min on each side (Figure 15a), the alternative way is to put them into oxygen plasma (500w) for 5mins on each side (Figure 15b). The cleaning effect of UV oven on glass is based on strong oxidation power from singlet

atomic oxygen O1(D), which are generated by the decomposition of Oxygen and Oxygen in the presence of UV emissions in 254nm and 185nm. The oxygen plasma (O^{2+}, O^{2-}, O_3, O, O^+, O^-, ionized ozone, metastable excited oxygen, and free electrons) are highly reactive and will react with the organic residue on the substrate and form water vapor and volatile carbon oxides. All removed contaminants are pumped out under low vacuum

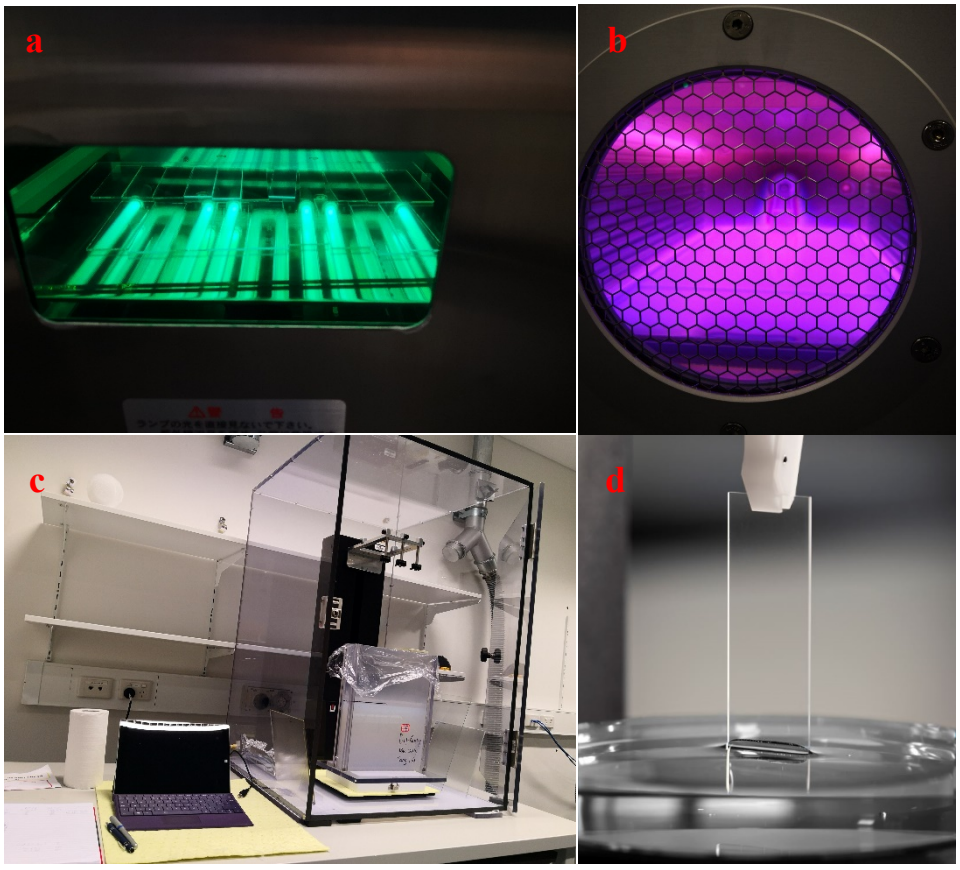

Figure 15. (a) The UV cleaning process. (b) Plasma treatment for the surface of the glass. (c) Dip coating process to prepare the thin film. (d) close-up image of the withdrawing step during dip coating.

system. Another gas commonly used for plasma treatment is argon, which is capable of physical cleaning via ion bombardment. Therefore, Argon plasma is sufficient for many types of contamination, such as Fluorine, organic contamination, and metal oxides.

The well-cleaned glass will be used for deposition of the film. Here, we use Nadetech ND-DC Dip Coater to fabricate our thin film, as shown in Figure 15c. The adjustable

parameters are the initial and final position, immersion speed, submersion time, withdrawal speed, drying period, and the number of cycles. Figure 15d shows the interface between the glass and solution when in the withdraw process. More details will be discussed in chapter 4.

3.3 Characterizations of particle size and distribution

Particle size characterization technologies mainly include Microscopy observation (optical and electronic), sedimentation size analysis, light scattering analysis, laser diffraction analysis, Acoustic & Electroacoustic analysis. Here we will combine Laser diffraction analysis system with Microscopy observation which are performed by Scanning Electron Microscope (SEM), Transmission electron microscope (TEM), to observe the silica particle in the sol.

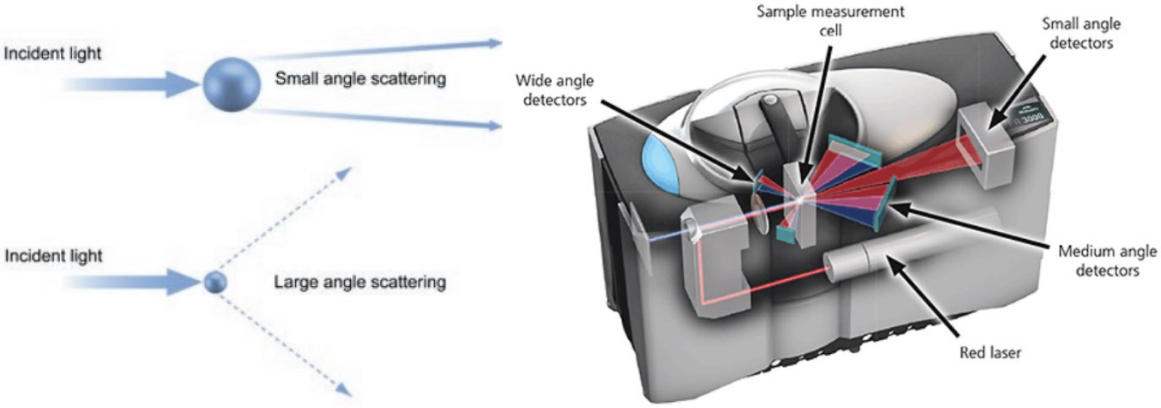

Figure 16. The schematic diagram of the working principle of Malvern Mastersizer 3000

Malvern Mastersizer 3000 - Laser Diffraction (LD): The particle size is determined from the measured variation in the intensity of scattered light as a function of scattering angle. As Figure 16 shows, large particles scatter light at small angles relative to the laser beam

and small particles scatter light at large angle. The angular scattering intensity is then analyzed to that created scattering pattern using the Mie theory of light scattering. The particle size is reported as volume equivalent sphere diameter. The basic setup of the Laser diffraction measurement system can be seen below in Figure 16b. There combine two light sources (blue and red) to measure the particle with different size.

Different from the laser diffraction and Dynamic scattering analysis method, Microscopy observation is a direct method of particle size analysis since it observes the morphology of individual particles. Here, Field-emission scanning electron microscope (FE-SEM450) and Field emission transmission electron microscope (Philips CM200) was used to observe the accurate particle size and surface characteristics, and the particle size distribution (PSD) of particles are obtained from Image analysis with the Image J software assistance. The image theories of the SEM and TEM are based on the interaction between electron and sample. However, SEM focuses on the sample's surface and its composition because it collects the scattered electron (backscattered secondary electrons) while TEM is based on the transmitted electron below the sample thus it provides more details about internal composition and structure like crystal structures, specimen orientations and chemical composition of phase.

Sample preparation for SEM: The silica particles were deposited on the glass slide via dip coating. Then, the silica-coated glass was heated at 100 degrees for 2 hours. Once the coating is thoroughly dried, we cut a small piece of glass and mount it on an SEM stub with conductive double-sided carbon tape, which connects the stub and glass so that the charge does not build up. To make the surface more conductive and obtain a good image, we coated the sample with 20nm platinum thin layer which provides a conductive coating to dissipate charging artifacts without much impact on the surface morphology.

Sample preparation for TEM: The silica sol was diluted by pure ethanol with a ratio of 1:1. Gently transfer a 10ul drop on the carbon grid (dark side face up), then dry it at room temperature overnight. The preparation of a thin-film sample for cross-section observation will be discussed in the next section.

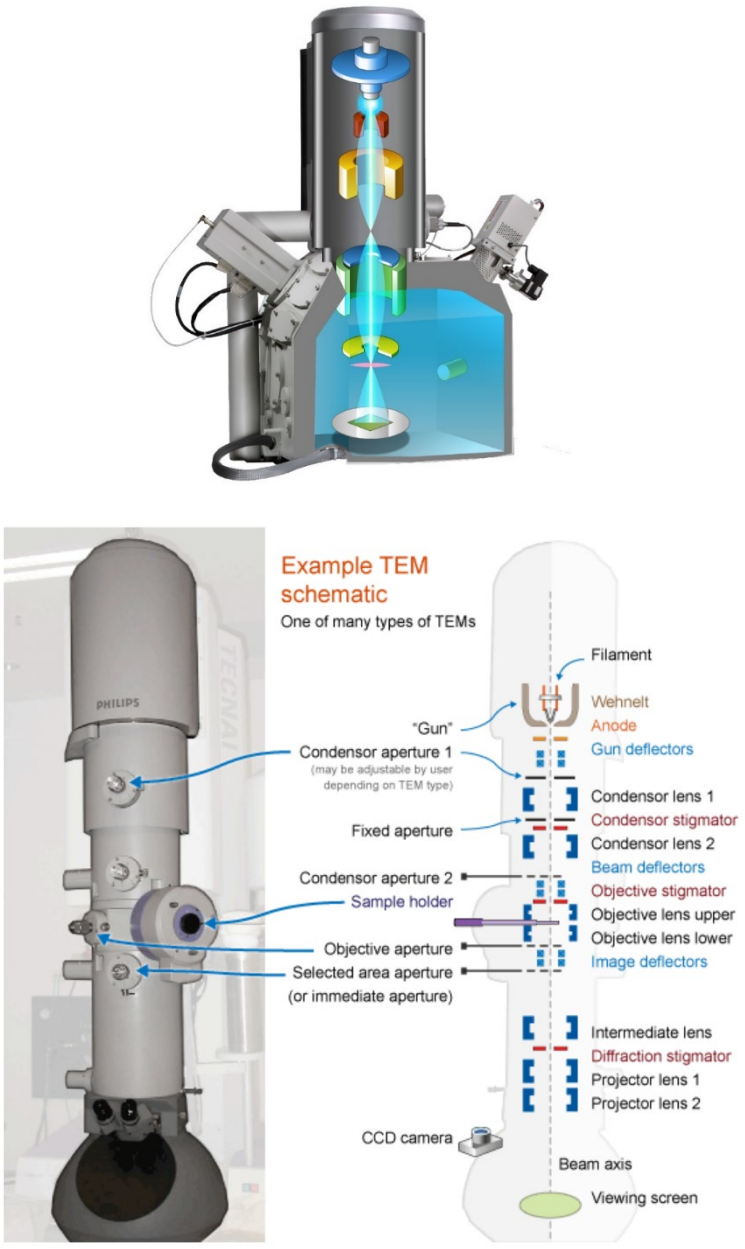

Figure 17. Generalized cut-away diagrams of the internal structure of scanning electron microscopy and transmission electron microscope alongside an example of a modern instrument. Copyright 2019 Microscopy Australia.

3.4 Characterizations of thin film

3.4.1 The optical property study by UV-VIS spectrometer

The investigation on the optical property, including transmittance and reflectance of the thin film coating on the glass, will be performed by PerkinElmer 950 UV-vis spectrometer (Figure 18 A). In general, for roughness surface, when the light hit the surface, there is specularly reflected light, diffused reflected light, absorbed light, specularly transmitted light, diffused transmitted light based on physical optical principle. PerkinElmer 950 UV-

Table 2. The setting parameters for operations on the Lambda 950.

Parameter setting		
Scanning Range		380-1100nm
Scanning Intervals/speed		4nm
Monochromator		860.80nm
CBM		100%
Slit	PMT	2nm
	Pbs	2nm
CBD		selected
Detector Change		860.80nm

vis spectrometer is equipped with three kinds of accessory module, Standard transmission module (STD), Integrating sphere module and Universal reflectance accessory (URA), of which, former two corresponds to specular transmittance measurement and reflectance measurement with different incident angle while the Integrating sphere module can sort out the testing of total transmittance and reflectance, diffuse transmittance and reflectance as well. Here, to capture diffuse and specular light, the integrating sphere (150nm) module was applied on the measurement of the total transmittance and reflectance of the coated

glass, the detailed testing procedure was shown below. (To obtain stable light sources, warming up the instrument for a half-hour before each testing)

Instrument setup was followed by the manual book. The measurement parameters were included in the following Table 2. After parameters set up, a baseline correction was

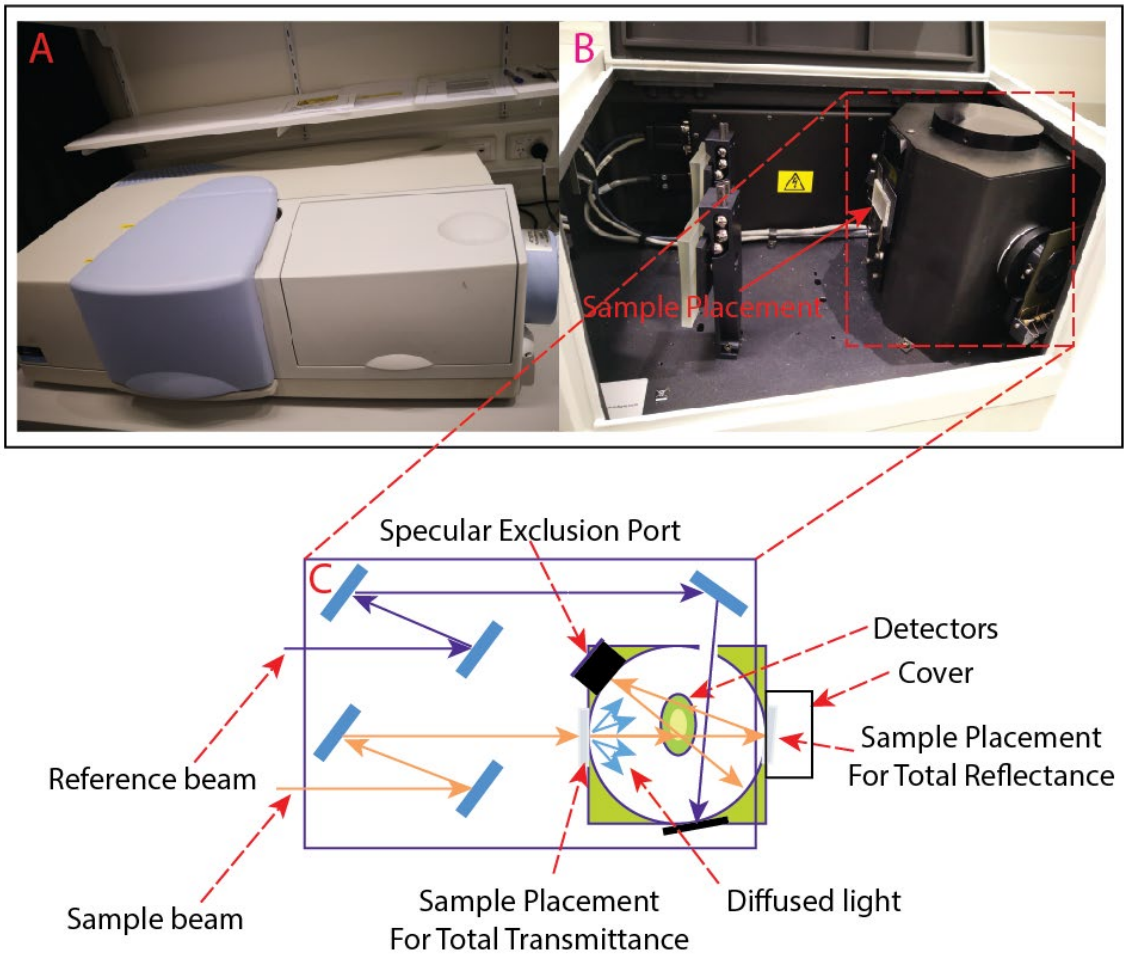

Figure 18. (A) The image of PerkinElmer 950 UV-vis spectrometer. (B) The compartment of the sample placement for transmittance testing and integrating sphere. (C) The schematic of the light path in measurement with the integrating sphere.

required to account for the effect of instrument noise and light-scattering particulates in the sample that can cause an offset in the testing results. For total transmittance measurement, Baseline at 100% transmittance was assessed by making blank testing in the air, and baseline at 0% transmittance will be performed by using the internal attenuate

to block the light. After standardizing baseline, we placed the sample glass on the detecting window on the Integrating sphere compartment as Figure 18B showed and started measuring. For total reflectance measurement, the specular exclusion port plug should be in place, and also the baseline correction is different as the sample placement is different, which can be seen in Figure 18C. Therefore, a reference white plate (calibrated 99% reflective sintered PTFE polymer disc) was placed on the sample mount position to perform the 100% total reflectance baseline, while for the 0% reflectance correction. We were not using the internal attenuator to block the beam. Instead, we simply removed the white reference plate from the reflectance port and replaced the cover. The spectra results analysis will be discussed in later chapters.

3.4.2 The surface topography observation by AFM

For micro observation, the most well-known types of microscopes are optical and electron microscopes, as we mentioned in previous sections. However, the image information from these two kinds of microscopes is two dimensional. In 1981, G.Bing and H.Rohrer invented a new type of the microscope named Scanning Tunnelling Microscope(STM), which is capable of providing high spatial resolution imaging of the order of 0.01nm based on the Tunnelling effect, a quantum mechanical property. The success of STM gives birth to a large family of instruments, generally referred to as Scanning Probe Microscopes (SPM).

Atomic Force Microscope, as one of the SPM, was developed to overcome a primary drawback with STM- it requires the sample to be conductive or semiconductive. AFM uses atomic forces to image the tip-sample interaction rather than tunneling effect. It can detect differences in height with a resolution of a nanometre when the integrated detector-

probe assembly scanning above the sample, as Figure 19A shown. In general, the scanning mode on the AFM can be separated into contact mode, tapping mode, and non-contact mode. Contact mode operates by scanning across the sample with the tip touching

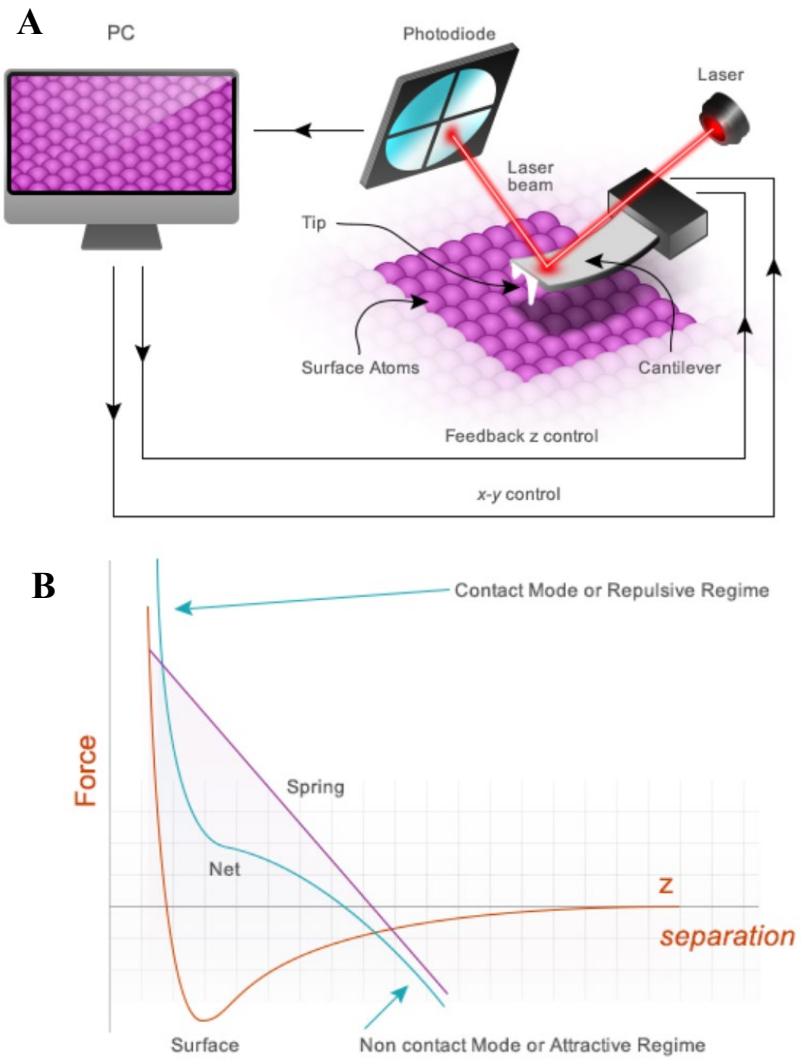

Figure 19. (A) Schematic illustration of an atomic force microscope connected to a computer. (B) Various forces curves at play in AFM. The purple straight line is the force curve for the cantilever. The force (the attraction and repulsion) versus distance curve between two atoms (brown) is the Lennard-Jones type curve. The blue line represents for the net force measured by AFM. Copyright 2019 Microscopy Australia.

the sample surface, with constant force or constant height. In order to monitor the change in cantilever deflection with a split photodiode detector, the constant force was obtained by a feedback loop, which will generate a plot of z (height) as a function of the tip x-y

position. The z values are used to build an image. Contact mode/Constant height is operated by maintaining the z (height) and monitoring the change in cantilever deflection by the split photodiode detector to directly image the surface topography. The advantage of this method is the relative simplicity of its technology, however, there are disadvantages: the sample can be damaged as the sharp tip raster-scanned over the surface as the lateral force exerted can be quite high as the Figure 19 B shows, while it also grinds down the tip which reduces the image quality.

In tapping mode, the cantilever is oscillated at or near its resonance frequency with an amplitude ranging from 20nm to 100nm, thus avoiding the issue of high-lateral forces. The tip lightly “taps” on the sample surface during scanning, contacting the surface at the bottom of each oscillation. As the tip approaches the surface, interactions between the tip and the surface caused the oscillation amplitude of the cantilever to decrease, the feedback loop corrects for these amplitude deviations and constructs an image of the surface topography. Accordingly, tapping mode gains the advantage of imaging soft sample or sample with soft surface. Moreover, the tip with tapping mode can maintain a long-lasting sharpness for a longer lifetime. However, from the net force curve in Figure 19B, the changing of z value leads to smaller changes in force, and hence the resolution of images from tapping mode is not as high as images from contact mode.

In our research, we tried both two scanning modes, contact and tapping mode, to get the non-conductive silica surface topography information. The results comparison will be discussed in later chapters.

3.4.3 The thickness measurement

Thin films are layers of materials with thickness ranging from a nanometer to micrometers. For optical coatings, semiconductor devices and thin-film photovoltaic devices, the thin film thickness is absolutely a key parameter to be well-defined. In our research, the silica thin film study was approached by spectroscopic ellipsometry, AFM, TEM combined Focus ion beam cutting technology.

Spectroscopic Ellipsometry: Ellipsometry is one of the optical techniques to determine thin-film optical thickness (physical thickness and optical constants) by measuring the interaction between the films and incident light. However, it is an indirect measurement technique requiring the combination of computer analysis and the results rely critically on a proper modeling of the physical sample. According to the working principle, a monochromatic polarized light beam is directed under a certain angle α on the specimen, the intensity or the change polarization state will be detected by ellipsometry, the measured values are expressed as psi (ψ) and delta (Δ), where ψ is the ratio of the amplitude diminutions, and Δ is the phase difference, as shown schematically in Figure 20A. Refer to the equation (2) which is the fundamental of Ellipsometry, the psi (ψ) and delta (Δ) is connecting with Reflectance polarized in P and S (R^p and R^s).

$$\rho = \frac{R^p}{R^s} = \tan\psi e^{j\Delta} \tag{2}$$

Therefore, we will need to construct a model which contains the parameters such as layer thickness and optical constants, which are expected to be known. In the system, the Rp/Rs can be calculated based on the input parameters according to the Fresnel Reflection equation[3], and we wish the data calculated from the model can matches the experimental data as closely as possible. The evaluation of the best-fit model is

represented by the mean-squared error (MSE), which comprehensively considered the experimental and model calculated values of φ, Δ, and the standard deviations. In general, the smallest MSE means the best fitting results, which will be regarded as the

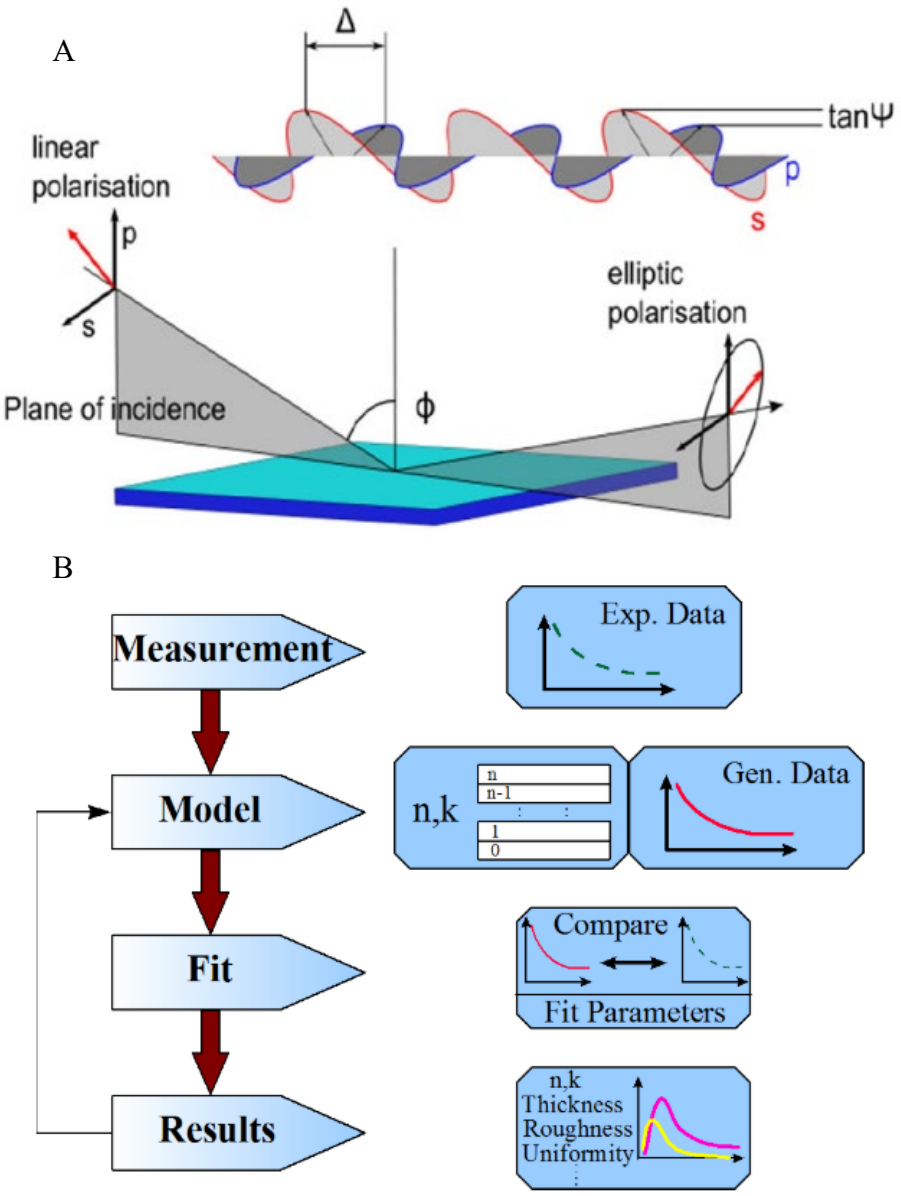

Figure 20. (A) Principle of Spectroscopic ellipsometry. (B) Basic procedure to determine film thickness from experimental data.

measurement results. The whole process to determine the thickness has been displayed in Figure 20B. Therefore, we can only hope that by making the ellipsometer and model as accurate as possible, the results will be accurate as well. In all cases, when a questionable result is obtained from ellipsometry modeling, it is advisable to corroborate the

ellipsometry results with data from other experiments such as Rutherford backscattering, transmission electron microscopy, and atomic force microscopy.

AFM: The working mechanism, accuracy, advantages, and disadvantages of AFM have been discussed in previous section. For thickness measurement, we used tapping mode and did a line scanning over the interface between the film and bare glass substrate. The interface was created by a scratch using plastic tweezer before the heat treatment of the wetting film.

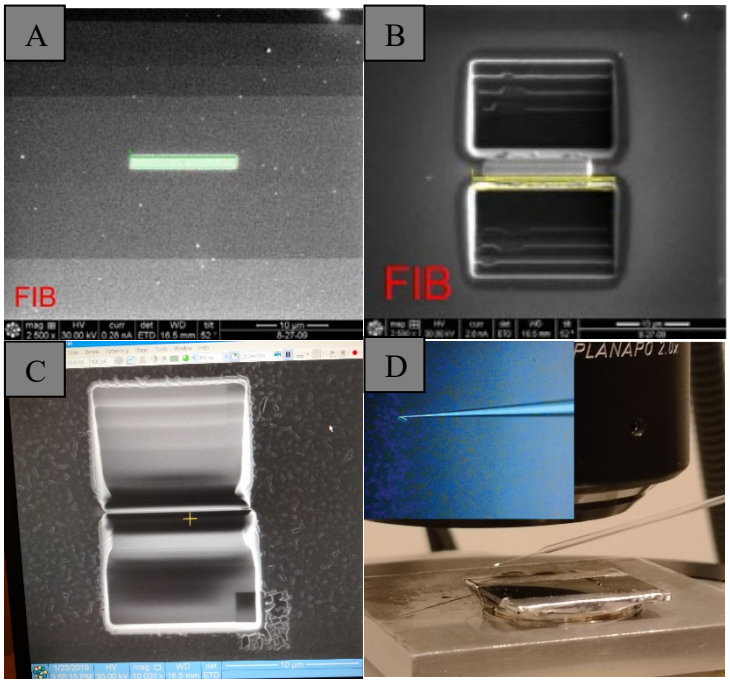

Figure 21. The preparation of a thin cross-section for TEM by FIB

TEM combined Focus ion beam cutting technology: To observe the thickness of the silica layer coating under TEM, we need to make a cross-section piece for the sample, the final thickness requires less than 100nm for a high-resolution image in TEM. The procedure of preparing a thin silica cross-section by FIB can be divided into four steps: Pt deposition, bulk out, thinning, cleaning, lift out, which corresponding to image A-B-C-D in Figure 21 respectively. The lift-out operation involves manipulating the sample slice either

within the machine (in situ) or from the sample block once outside the machine (ex-situ), here we use the second method performed on a benchtop light microscope and a long glass needle as shown in Figure 21D. The sample slice can be adhered on the needle because of the electrostatic force and then flat the slice on the support grid. After the lift-out, the thin cross-section sample will be put on copper mesh grid which can be sent for TEM imaging.

Chapter 4 Synthesis of Silica Nanoparticles with controllable size by Sol-Gel process

4.1 Experimental Procedures

Synthesis of Silica Nanoparticles by sol-gel processing

The sol-gel processing can be divided into two-stage: hydrolysis and condensation.[157] The investigation of the effect on the size and distribution of silica from reactants and reaction condition was studied by a series of the experiment at different amount of TEOS, water, the catalyst ammonia, as well as the aging time respectively. Here, we use TEOS as a precursor, mixed with absolute ethanol, deionized water, Ammonia (30%) with a certain volume ratio then magnetically stirred for 1h at 45 degrees Celsius. After that, the solution was aged for different days to obtain sol. The experiment parameters are tabulated in Table 3.

Table 3. The molar ratio of the experimental parameters.

Sol	TEOS	NH^{4+} (15wt% NH3•H2O)	Ethanol(100wt%)	DI water
1	1	0.28	38	2
2	1	0.33	38	2
3	1	0.38	38	2
4	1	0.43	38	2
5	1	0.48	38	2
6	1	0.53	38	2
7	1	0.58	38	2
8	1	0.88	38	2
9	1	0.98	38	2
10	1	1.18	38	2

Preparation of Silica xerogel by solvent evaporation

The silica sol was converted into xerogels by evaporative drying: For SEM observation, 20μL of sol 1-6 were transferred into soda-lime glass slide, then the glass slide was placed into an air furnace at 120℃ for 24hrs. The nitrogen adsorption-desorption experiments require at least 50mg of one sample. Thus, a certain amount of sol 1, 5, 9, 10 was poured into four glass Petri dishes and covered with pierced plastic wrap. Then these dishes were placed into an air furnace at 120℃ for 24 hrs.

4.2 Results and Discussion

4.2.1 Catalyst effect on the sol.

To study the ammonia effect on the formation of silica sol, we prepared the sol with different NH^{4+} / TEOS molar ratio by mixing a certain amount of TEOS, ammonia, Ethanol, H_2O and then followed by magnetic stirring for 2 hours and aging seven days. The molar ratio of $NH4^{+}$ / TEOS is presented in Table 3. The TEM results of different silica sols are shown in Figure 22. As we introduced in chapter 3, TEM sample preparations proceed in similar conditions: 1ml of the sample sol is transferred into a small glass tube and mixed with 1ml pure ethanol, followed by 5 mins ultrasonic vibration. Then, 10ul of the mixture was dropped on the carbon grid for TEM observation. Figure 22A-J reveals not only the particle size but the particle distribution. In Figure 22A-C, the nano-silica particle exists severe crosslinking; the average particle size is 9.8, 12.6, 14.8nm, respectively by the image J statistical analysis. According to Flory-Stockmeyer theory[160], even though there are four reactive sites on the TEOS monomers under basic condition, there are not enough NH^{4+} to help the hydrolysis of TEOS on four sites at the

same time. Thus, the hydrolyzed TEOS monomers may only have one or two reactive sites for condensation reaction. This does not favor the formation of the larger particle but the linear structure of small particle which is shown in Figure 22A. Therefore, crosslinking can be explained by the smaller particle having a relatively larger fresh surface wherein the active sites inducing condensation happened. As we can see in Figure 22K, the mean particle size increases from 9.8nm to 91nm when the molar ratio of $NH4^+$ to TEOS increases from 0.28 to 1.18. However, according to previous research, the

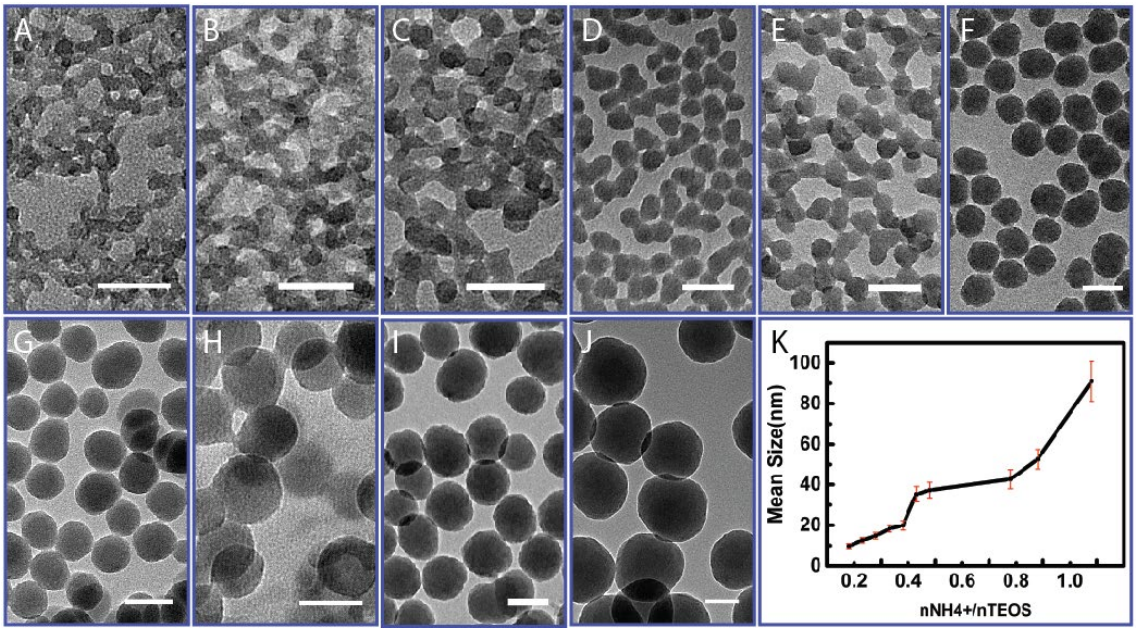

Figure 22. The TEM images of different silica sol, (A-J) corresponding to Sample 1-10, and (K) is the Mean size of silica particle with the molar ratio of NH4+ / TEOS. Scale bars 50nm.

change of particle size is primarily due to the effect of the hydroxy group[161, 162]. Obtained by simple stoichiometry calculation, the initial concentration of hydroxy groups in sol one is 0.11246 mol/L thus the pH value is 9.2. Then, the hydroxy concentration and pH corresponding to the rest sol systems (2-10) increases linearly as present in Figure 29. The hydroxyl concentration increase leads to an increase of hydrolysis and condensation, but their ratio decreases[163, 164]. As a result, the increase of particle size[165-167] is

associated with the ratio of hydrolysis speed to condensation speed according to the following equation[164]:

$$r \sim \left(\frac{1}{k_0}\right)^{1/6} = \left(\frac{k_p c_0}{k_h}\right)^{1/6} \quad (3)$$

Where r, k_0, k_p, k_h, c_0 represents the final particle size, hydrolysis rate constant, Polymerization rate, the hydrolysis rate, the initial concentration of the unhydrolyzed monomer. Therefore, the amount of ammonia directly determines the initial hydroxyl concentration, which affects the ratio of the rate constant of hydrolysis and condensation, further causing the difference in particle size.

Table 4. Particle size and distribution of the silica sols with different nNH4+ /nTEOS.

Sol	Aging	n_{NH4+}/n_{TEOS}	Particle size	PdI
1	7	0.28	9.8 ± 1.2	1.5%
2	7	0.33	12.6 ± 1.3	1.1%
3	7	0.38	14.8 ± 1.6	1.2%
4	7	0.43	18.2 ± 1.6	0.8%
5	7	0.48	19.9 ± 2.3	1.3%
6	7	0.53	35.3 ± 3.8	1.1%
7	7	0.58	37.3 ± 3.8	1.0%
8	7	0.88	42.7 ± 4.7	1.2%
9	7	0.98	52.6 ± 4.9	0.9%
10	7	1.18	91.0±9.8	1.2%

Moreover, we compared the stability of different sol using the polydispersity index (PDI) as the reference. PDI can be calculated as the following,

$$PDI = (\sigma/XC)\ ^2 \times 100\% \quad (4)$$

Where σ is Standard deviation of particle size distribution, and XC represent the Average particle size. The polydispersity index (PDI) of all the samples are around 0.01, shown in

Table 4, demonstrating a good mono-dispersity. Therefore, the increase of ammonia catalyst increases the particles size while does not change the particle distribution. We also believe the different particle size will affect the pore size or morphology of the silica xerogels. Therefore, we designed the following experiment: the xerogels derived from sol 1, 5, 9, 10 were characterized by SEM and nitrogen adsorption-desorption isothermal experiments.

4.2.2 Morphology observation and porosity characteristics of silica xerogels

The film cross-sections were created by scratching the film using a blade, and then we observed the debris which is in an upright position by dynamic focusing model in SEM. Figure 23A-F is corresponding to the SEM images of xerogels derived from sol 1-6, respectively. We noticed that all the film consisted of large silica aggregates. However, the TEM image of sol 1-6 (Figure 22) gave the results of gradually increasing particle size from 9.8 to 35.3nm in diameter. Based on the observation results from SEM, the average diameter of this silica cluster was calculated from the statistical histogram are ranged from 42.5-58.4nm. Accordingly, we are led to infer that the nano-silica particle aggregated into a large particle during the conversion from sol into xerogel. The inefficiency packing of silica particle aggregates introduced many pores, and we can see the porous structure become more apparent from Figure 23A to F.

The silica xerogels thickness is more than 1 μm, and the drying rate difference perpendicular to the substrate cannot be ignored. It creates the capillary tension gradient on the xerogel film body, resulting in non-uniform shrinkage of the network[168]. In image F, which corresponds to sample xerogel from sol 6, there appear some macropores (>50nm) marked by red circles, and even a crack spreads along these macropores.

According to the Laplace equation[169], the larger pore structure in xerogel (sol 6, image F) leads to lower capillary tension. Besides, the film composed of large particle bearing a low elasticity modulus, the stress concentration induced by the capillary tension gradient can be not released, and the crack occurs[170]. However, for thin film with thickness below 1μm, the crack can be suppressed to a great extent. It is mainly caused

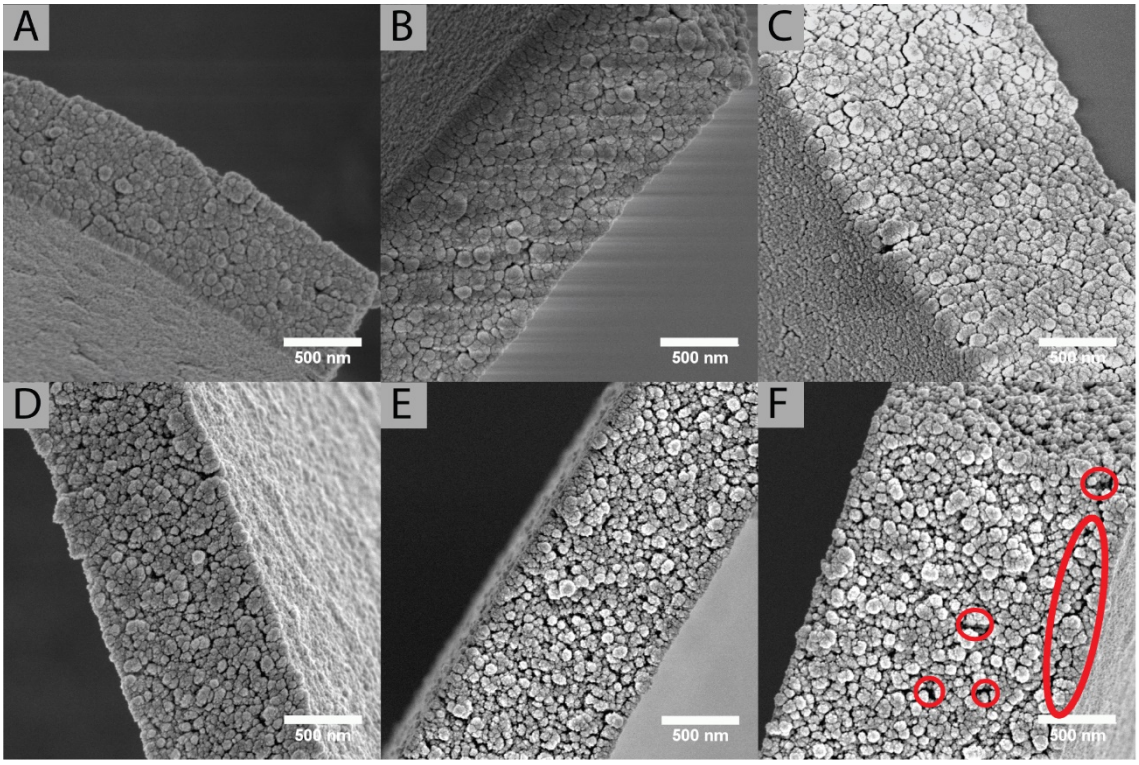

Figure 23. The SEM cross-section image of silica xerogels from (A)sol 1, (B)sol 2, (C) sol 3, (D) sol4, (E) sol5, (F) sol 6. (Scar bar, 500nm.) The macropores (>50nm) and a crack spread along these macropores marked by red circles.

by the lack of energy when the crack compensates for the energy expended in mechanical damage at the crack tip[168].

Besides, it was observed on the magnified SEM image (Figure 24A) of xerogel (from sol 10) that the xerogel is composed of spherical silica particle with the size range of 70-100nm in diameter, which is a good response to the TEM results, average diameter size 91nm with 9.8nm standard deviation. More interestingly, the spherical particle looks

smooth on the top while the side is rough and has many bumps. Considering previous inference that the particle aggregates together during solvent evaporation drying, we would consider that the smooth top was caused by the 30nm thickness platinum (Pt) coating to get a better conductivity surface because the Pt layer was deposited on the

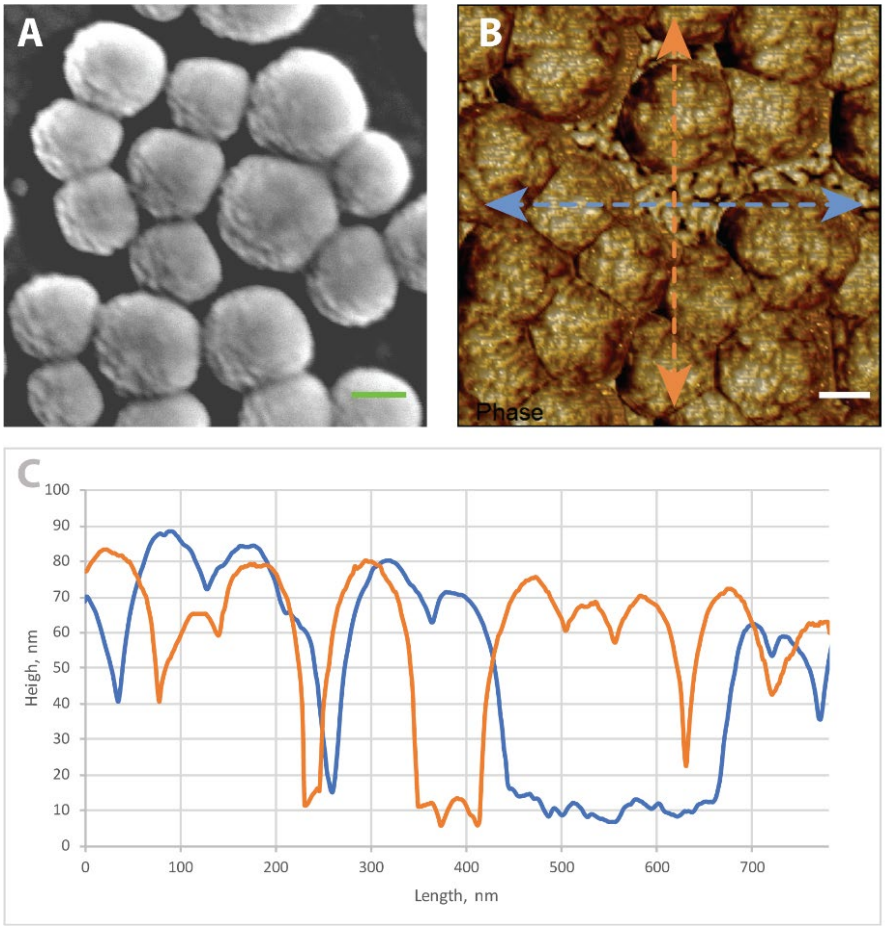

Figure 24. (A), (B) are the SEM images and corresponding AFM phase image of silica xerogels (sol 10) on glass substrate respectively, scale bar 50nm. (C) The section height along the two line in the AFM image (B).

sample surface by sputtering Pt target on the top of the sample stage. Then, a topography of the xerogel particle without Pt coating was obtained by AFM on scanning mode. The result (Figure 24B) shows the whole spherical silica particle looks rough, and the small bumps are everywhere on the surface. Therefore, we can reasonably conclude that the

spherical silica particle on xerogel is formed by the aggregation of smaller silica particles during solvent evaporation drying process.

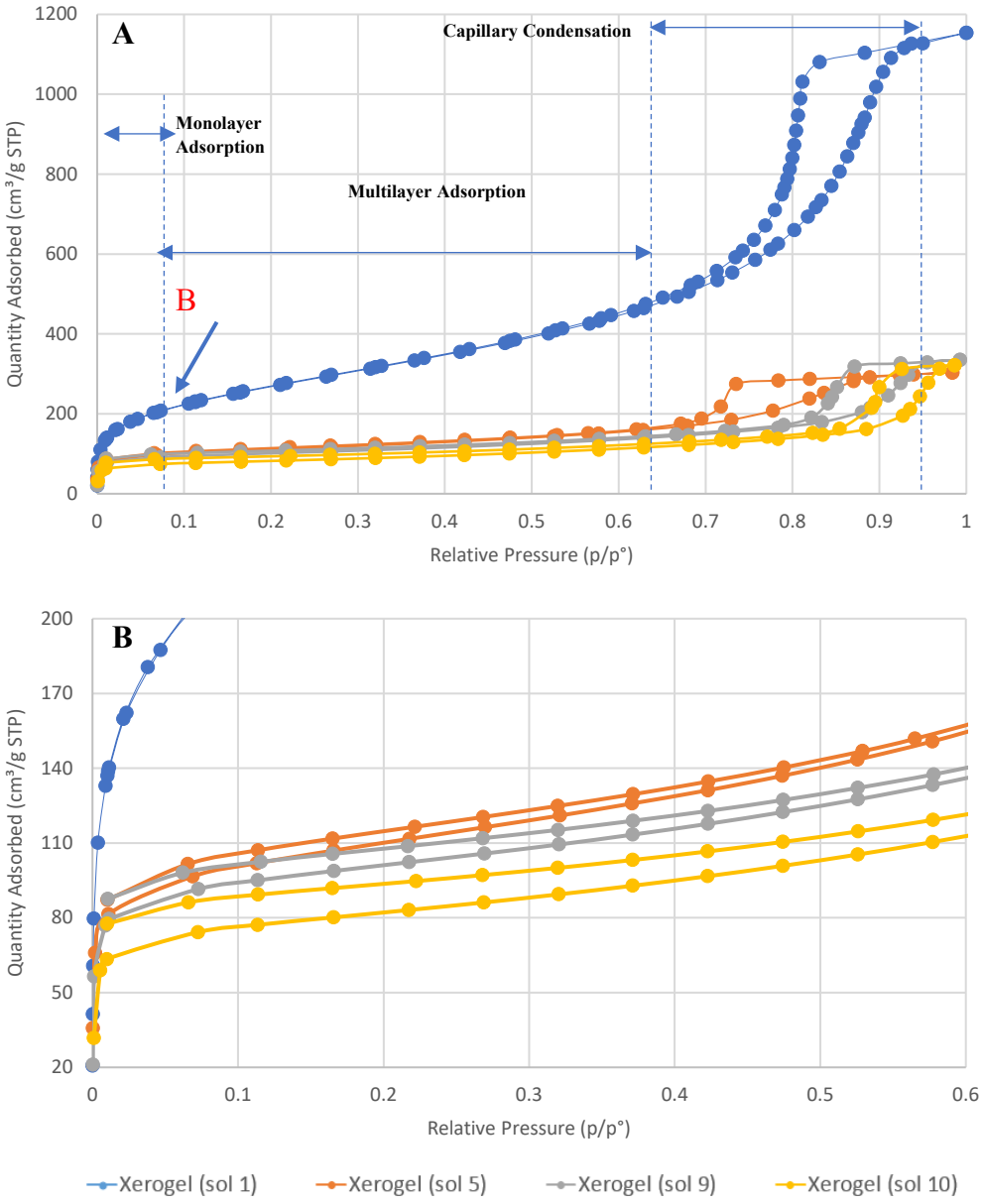

Figure 25. (A) Nitrogen adsorption-desorption isotherms of xerogels obtained by solvent evaporation of silica sols 1, 5, 9, 10. (B) The enlarged adsorption and desorption isotherms from P/P0~0 to 0.6.

After making a general observation on the surface morphology, a more thorough assessment of the silica xerogel internal porous structures in terms of pore size and volume is undertaken in the measurement of gas adsorption and desorption isotherms. In

the context of physisorption, the pore can be classified by the size: pores with widths exceeding about 50nm, between 2nm and 50nm, and less than 2nm are called macropores, mesopores, micropores, respectively[171]. In our experiments, the adsorptive gas is nitrogen, and adsorbent is the silica xerogel. Each sample (silica xerogel) is degassed at 150℃ for 3 hours. The nitrogen adsorption and desorption isotherms of four xerogels are plot together and shown in Figure 25A. The isotherms for xerogel (sol 5, 9, 10) belong to type IV, which is characterized by its high-pressure hysteresis loop. For the xerogel derived from sol 1, it shows a combination of type I and IV because of the increasing trend of the adsorption at high relative pressure. To take xerogel (sol 1) as an example, the initial part of the isotherm, corresponding to horizontal axis P/P0 value from 0 to about 0.09, is associated with the monolayer adsorption. At low relative pressure, the nitrogen molecular begins to be adsorbed on the surface of micropore (<2nm) because of the strong adsorption forces (Physical adsorption). With the increase of relative pressure, the monolayer adsorption is complete at the arrow point B, where is the beginning of the multilayer adsorption. The monolayer adsorption is the direct contact between the adsorbent and adsorptive gas (nitrogen), while the adsorption space enables more than one layer of nitrogen molecular in multilayer adsorption. Therefore, the monolayer capacity which reveals the amount of adsorptive gas molecular occupies the surface of the absorbent can be used to calculate the surface area of absorbent according to BET theory[172]. It was noted that the absorption rate increased dramatically when the relative pressure is up to 0.65, and

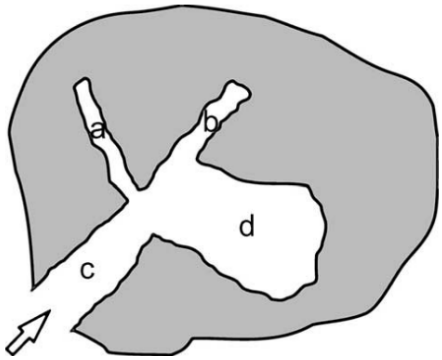

Figure 26. The pore network leading to the adsorption hysteresis, (a-b) small pores, (c) the connecting pore, (d) large pore.

hysteresis loop occurs during the relative pressure of 0.65-0.95, which is associated with the appearance of capillary condensation in mesopores(2-50nm). The detailed explanation of the high-pressure hysteresis loop can be given by the pore network effects that some pores play a role as an intermediate connection of the small pores and semi-closed large pore to out surface. The connecting pore size is relatively smaller than the large pore. Thus the emptying of adsorptive molecular happened in the small pore firstly while for the semi-closed large pores a lower pressure will be required, the illustration seen in Figure 26 [173]. Therefore, capillary condensation and capillary evaporation often do not take place at the same pressure, which leads to the appearance of hysteresis loops. In most case, the capillary condensation will stop once the mesopores were filled up as the xerogel (5, 9, 10) isotherms shows. However, we observed that the isotherm for xerogel (sol 1) seems to retain an increasing trend, and it may be caused by the appearance of big holes induced by structure collapse when the relative pressure reaches more than 0.95.

Additionally, we noted the low-pressure hysteresis phenomenon, the adsorption and desorption isotherms do not coincide at the initial part, among the enlarged isotherms for four xerogels from sol 1, 5, 9, 10 (Figure 25 B). Our experiment was performed by nitrogen at 77 K, and the capillary condensation induced hysteresis closure point should be above the P/P0~0.4[174], corresponding to the nitrogen boiling point. The xerogel (sol 1) isotherms completely close at about P/P0~0.6 which is above 0.4. Traditionally, this low-pressure hysteresis is attributed to the comparable pore size to the width of the adsorptive molecule and the swelling of the nonrigid structure[175, 176]. However, herein, we would like to consider this phenomenon as indicative of lack of equilibrium in the adsorption branch, in other words, there is no enough time for nitrogen molecular to diffuse into the constricted micropore network in adsorption whereas the desorption

branch would be under perfect equilibrium conditions[177]. In a case like this, we are suggested to increase the dwelling time to ensure the micropore network can be occupied entirely or to try other adsorptive like CO_2 since the CO_2 molecular size is somewhat smaller and easier to diffuse into the pore network, though there may be much difference in final results.

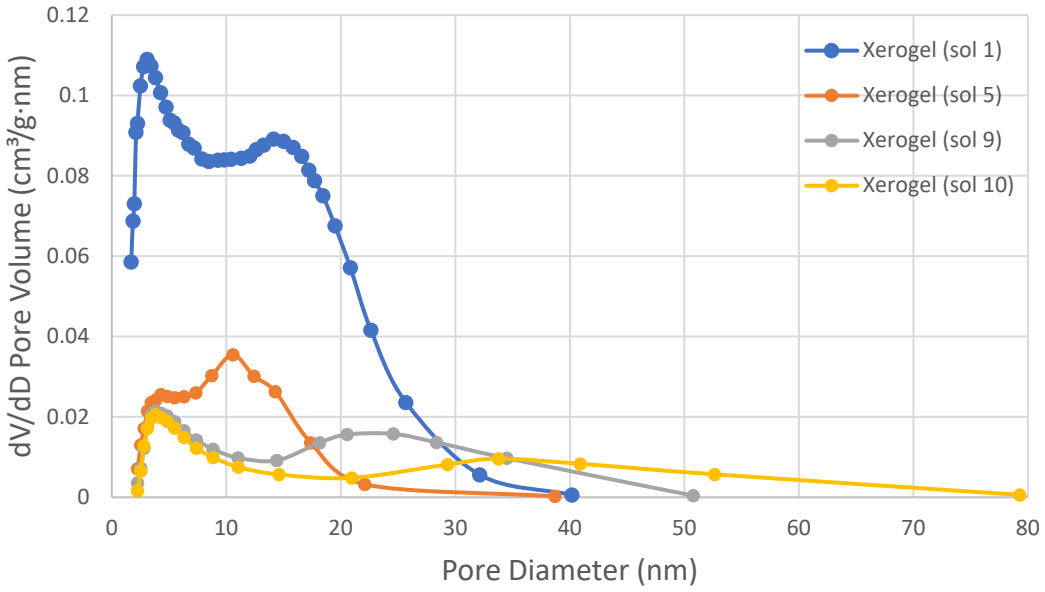

Figure 27. Adsorption pore size distribution curves calculated by BJH method.

To further confirm the presence of disordered mesopores on the solvent evaporation derived xerogels, we calculate the pore size distribution curves (Figure 27) from the adsorption isotherm curves using the Brunauer-Joyner-Halenda (BJH) method[178, 179]. The particle size distribution curves show not only one peak. For xerogel (sol 1), it can be observed two peaks, evident one position in the range of 0 to 10nm and another relative lower peak between 10 to 20nm, and these evidenced the disordered mesoporous structure (2-50nm). For xerogel (sol 5), we can see the pore size around 10nm becomes the main part of the pores. The xerogel (sol 9) has a certain amount of large pore with a diameter size of 20-50 nm, and the peak goes near to 25nm. In xerogel (sol 10), there appear macropores, and the pore size range enlarges to 2-80nm. The BET surface area and BJH

derived pore volume and pore average diameter were summarized in Table 5. The BET surface area shows a decrease among these four xerogels (sol 1, 5, 9, 10), the xerogel (sol 10) bearing the lowest surface area, 269.07 m^2g^{-1}, the xerogels (sol 9, 5) having a relatively larger surface area, 330.04 and 366.29 m^2g^{-1} respectively, but what is worth noting is that the BET surface area on xerogel derived from sol 1 dramatically increase to 977.84 m^2g^{-1}, and the pore volume is 1.86 cm^3g^{-1} which is much bigger than the values, 0.41, 0.45, 0.45 m^2g^{-1}, corresponding to xerogel (sol 5), xerogel (sol9), xerogel (sol10),

Table 5. Textural properties of four xerogels from sol 1, 5, 9, 10, respectively.

Sample	S_{BET} /m^2g^{-1}	Pore volume /cm^3g^{-1}	Pore diameter /nm
xerogel (sol 1)	977.84	1.86	7.85
xerogel (sol 5)	366.29	0.41	7.84
xerogel (sol 9)	330.04	0.45	11.28
xerogel (sol 10)	269.07	0.45	13.09

separately. Combined with previous SEM and TEM results, we have reasons to believe that the nano-silica particle aggregates to large cluster during solvent evaporation, and large silica particle(20-90 nm in diameter) in sol 5, 9, 10 tend to form the xerogel with non-uniform large pore, whereas the sol 1 made by nano-silica (9.8nm in diameter) are able to produce xerogel with uniform distribution and high percentage of mesopores.

4.2.3 Growth Mechanism and Aging Effect

Besides the ammonia effect on the silica sol, we investigated the effect of sol aging time as well. Here we studied the conversion of solution 1-10 into sol and gel with increasing aging days, 1-60 days. The solution 1 with a molar ratio of NH^{4+} and TEOS lower than

0.28 undergoes a slow initiation Step (relative slower hydrolysis and condensation). It tends to obtain a linear structure initially (Figure 22A) according to Flory-Stockmeyer theory, which has already been discussed in the previous section. The nucleation occurs everywhere in the solution and consumes the presence of soluble silica or active monomer (hydrolyzed monomer), thus depress the growth of the small particle. Therefore, the solution forms a silica sol. With the increased aging time, there will progressively form a branched cluster by the additional cross-linking of the unreacted hydroxy group and methyl groups on the small particle when the solvent gradually evaporates[180]. Afterward, the sol system reaches the gel point when these branched clusters grow and link with each other and further form a three-dimensional network structure, as shown in Figure 31D [181]. The solution 2-9 remain a stable sol system with pH value ranging from 9.3 to 10 after 60 days. In this case, the particle crosslinking still can be depressed by the consuming of the small particle (Ostwald ripening) and the steric hindrance, which comes from negatively charged silica particle adhered by the amount of hydroxy group and these silica particles repel each other[182]. The hydroxy group in the sol system

plays essential roles not only in base-catalyzed hydrolysis and condensation but also in depressing the aggregation of silica particle by the electrostatic effect.

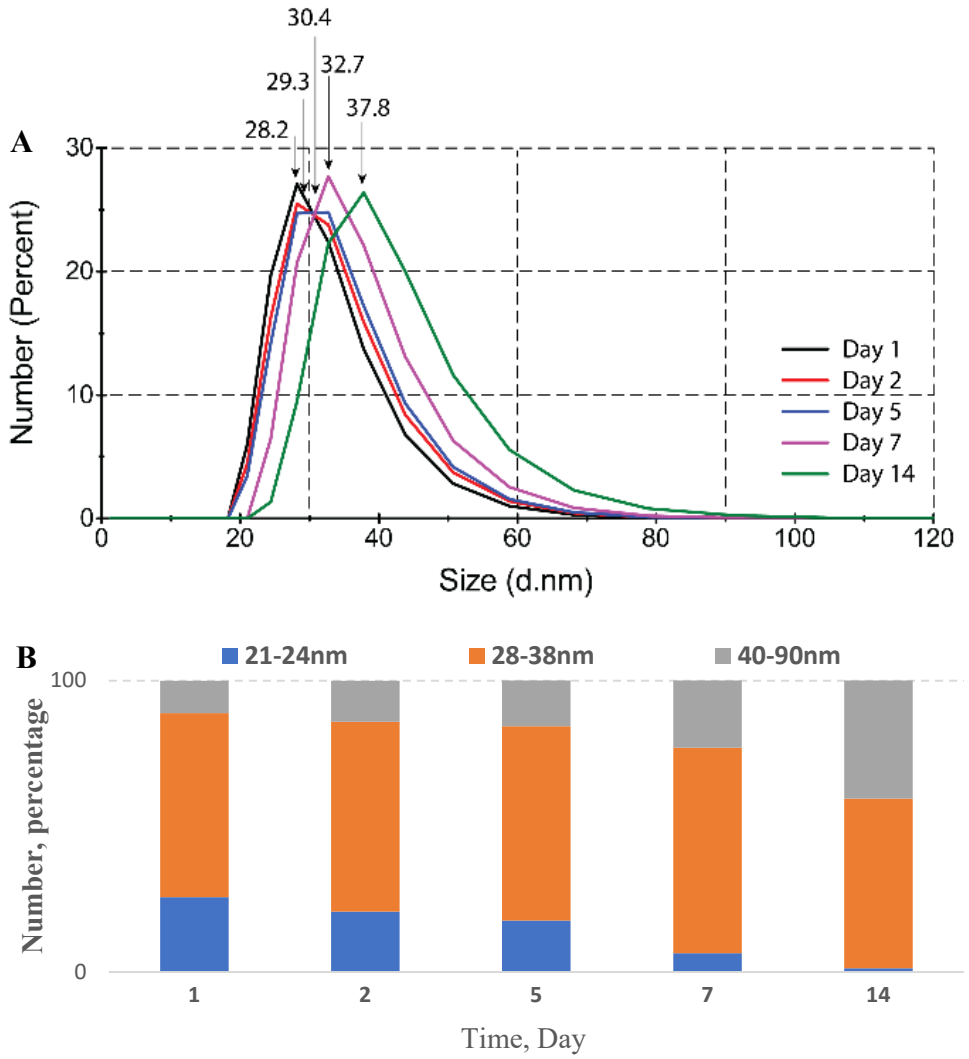

Figure 28. (A) The particle size and distribution data measured from Zetasizer based on dynamic Light Scattering. (B) Percentage of silica particle in three size range, 21-24nm, 28-38nm, 40-90nm.

Ostwald ripening(OA) theory was accepted by many pieces of research for a discussion of the growth mechanism in sol-gel system, and it can be described as the small sol particles dissolve into smaller molecular or component and redeposit or combined onto larger sol particles[158, 161, 162, 182]. Specific study on sol 6, the particle size distribution has been analyzed by Zetasizer, and the results are shown in Figure 28 (A).

The size distribution measured in different days has been sort together, the black line corresponding to the measurement on the first day, and the red line represents for the second day's results. The blue, purple, and green line record the size distribution in five, seven, and fourteen days after the begin of aging. In the first day, the particle with 28.2nm in diameter has a significant portion, and one day later, the peak of size distribution curve shift to 29.3nm. After two weeks, the particle diameter of 37.8nm takes the major part in the sol. Apparently, the particle size distribution range gradually move to the large size area.

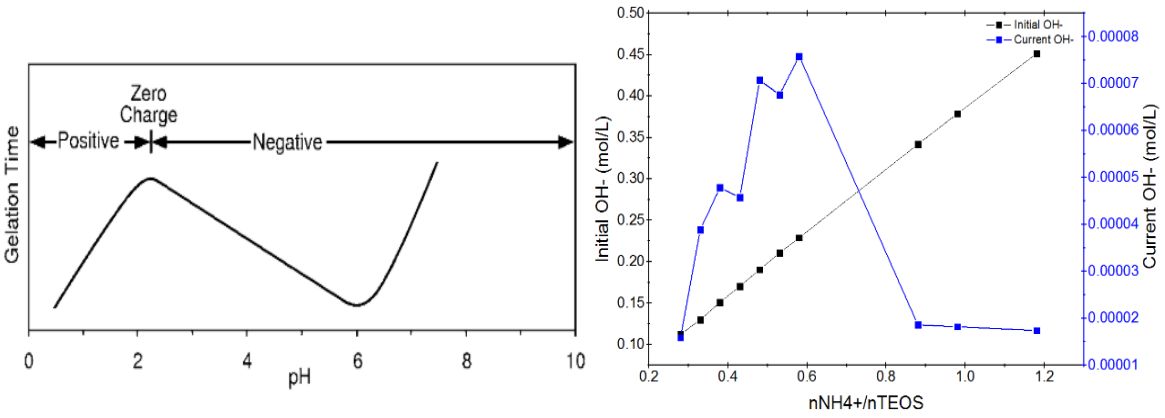

Figure 29. The pH effect on Gel time in silicate sol–gel system[1].The initial OH- mole concentration and the OH- mole concentration after 60 days.

In our case, the particle with 28.2nm in diameter appears and takes a major part after one day later. We did not focus on recording the initial transition from TEOS derived hydrolyzed monomers into oligomers and thus form nuclei. However, much of the research applied the advanced characterization technologies (in-situ TEM, SAXS, DLS) into the observation the sol-gel particle growth. It was generally agreed that the silica nanoparticle formation could be dived into three stages[161, 162]: (1) the polymerization of the hydrolyzed monomers leads to oligomers which becomes a seed for further nucleation. (2) the resulting nuclei (few nanometers) enters a growth stage wherein the

Ostwald ripening occurs. (3) The aggregation of the silica particle before the endpoint of the ripening. Therefore, it is safe to make two assumptions: The polymerization of hydrolyzed TEOS monomers proceeds throughout the whole process from beginning to the end of ripening; The hydrolyzed monomers and small particle can be consumed or re-deposited onto the large particle. Then, we separate the particle size into three groups, 21-24nm, 28-38nm, 40-90nm, respectively. The proportion of these group in different days has been illustrated in Figure 28(B). The blue part is the particle with a diameter range between 21-24nm, and it shows a decreasing trend and eventually nearly disappears after two weeks. It may be caused by two reason or individual one of them, the aggregation behavior among this small particle[183] and the hydrolyzed monomers or oligomers deposited onto the surface of particle by curvature effect and made it grow up[182]. The orange bar represents for the particle diameter range between 28-38nm, which shows a slight decline but still taking up more than half percentage, this can be explained by the same reasons for the change of blue bar. The silica particle(21-24nm) grew and was included into the larger size range(28-38nm) while the particle(28-38nm) also grew and became even larger particle, and the different growth speed makes the difference. The grey one is for large particle, 40-90nm in diameter. It is noted that the grey part goes steadily up to about 40% from only 10%. The percentage increase of the large particle(40-90nm) and high homogeneity most probably means the close to the end point of ripening.

Also, the aging days-dependent changes in particle size and distribution has been obtained in the statistic of TEM images (Supporting information Figure S 1) and summarized in Table 6. We can see the particle size increased from 32.5nm to 33.4nm and the PDI decreased from 2.0% to 1.4% during the first 5 days. There is a slight deviation compared with the results given by DLS (Figure 28 A), and it should be acceptable considering the instrument error and manual measurement of the particle size by image J software. After 14 days, the disperse stability index(PDI) remains a lower value (1.5%) relative to the

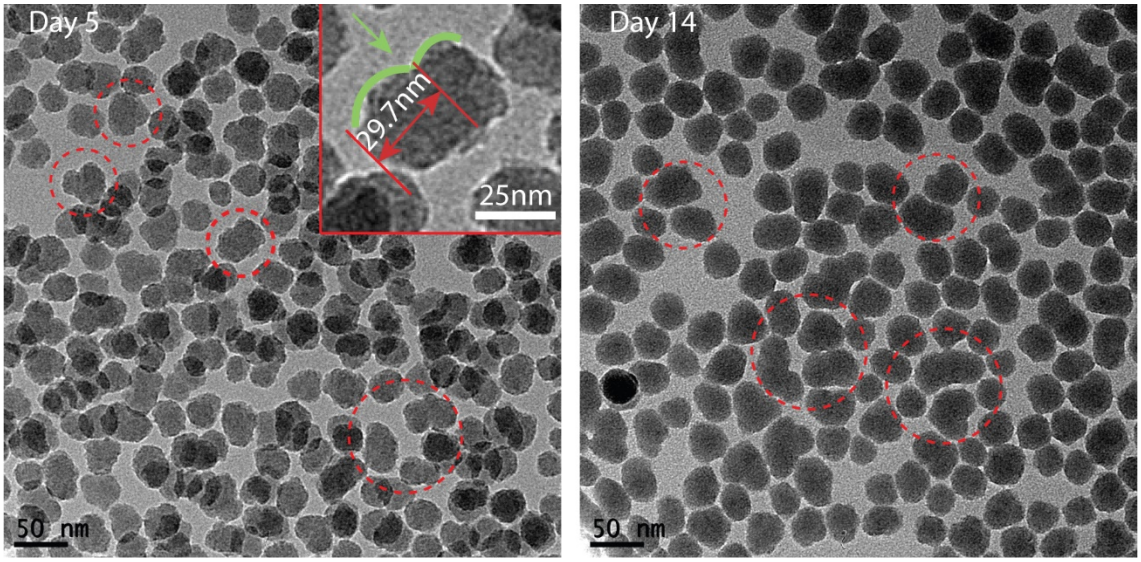

Figure 30. TEM images of silica particles derived from sol 6 in 5 (left) and 14(right) days. The red dash line circles spontaneous self-organization of adjacent particles. Inset is an enlarged image of a circled area.

first few days results, which also matches well with the analysis results from DLS(Figure 28 B), meaning the aging nearly stops[184]. The TEM image (Supporting information Figure S 1 D30) of the sol particle further confirmed that the ripening nearly stops in two weeks, the average particle size increment was almost negligible and the PDI clam down to the lowest value, 1.1% (Table 6).

We already discussed the initial formation of the small particle(<10nm) according to Flory-Stockmeyer theory, which explained the crosslink among these small particle results from the reaction between the surface-active site, and it also suggests that the nucleation occurs when the crosslinked oligomers grow up to molecular weight and become unstable. After silica nuclei appear, the growing pathway was recorded by days on TEM. Figure 30 presents the high-resolution TEM images of silica particles (sol 6) on the fifth and fourteenth day.

Table 6. Particle size and PDI of the silica sol 6 with increasing aging days in statistics from TEM observation.

Sol	Aging time(day)	n_{NH4+}/n_{TEOS}	Particle size (nm)	PdI
6	1	0.53	32.5 ± 4.2	1.7%
6	2	0.53	31.2 ± 3.9	1.6%
6	4	0.53	31.5 ± 4.4	2.0%
6	5	0.53	33.4 ± 4.0	1.4%
6	14	0.53	36.4 ± 4.4	1.5%
6	30	0.53	35.3 ± 3.7	1.1%

Take an overall look at these two images, where the silica particle experienced 14 days' ripening is smoother than the particle in five days. Michael T. Harris[185] and Van Blaaderen et al.[186] proposed that the larger siloxane groups result in a roughness structure and the smooth boundaries on large particle benefit from the much smaller molecular or oligomers addition. Most significantly, we observed many silica aggregates(circled area in Figure 30), which are composed of two or more single silica sphere. From the enlarged image, it clearly showed the joining of two-particle (29.7nm). These two particles have been reacted with each other and form a fusion which has no

physical contact. This phenomenon is similar to the self-organization of adjacent nanocrystal particles based on an oriented attachment mechanism [187]. However, the silica particle is amorphous, so there is not a share of common crystallographic orientation. Moreover, unlike the aggregative growth model[185], which shows a double peak in distribution curve because it says that the particles aggregate to a large spherical particle rapidly relies on the electric double layer theory, the distribution curve for our samples

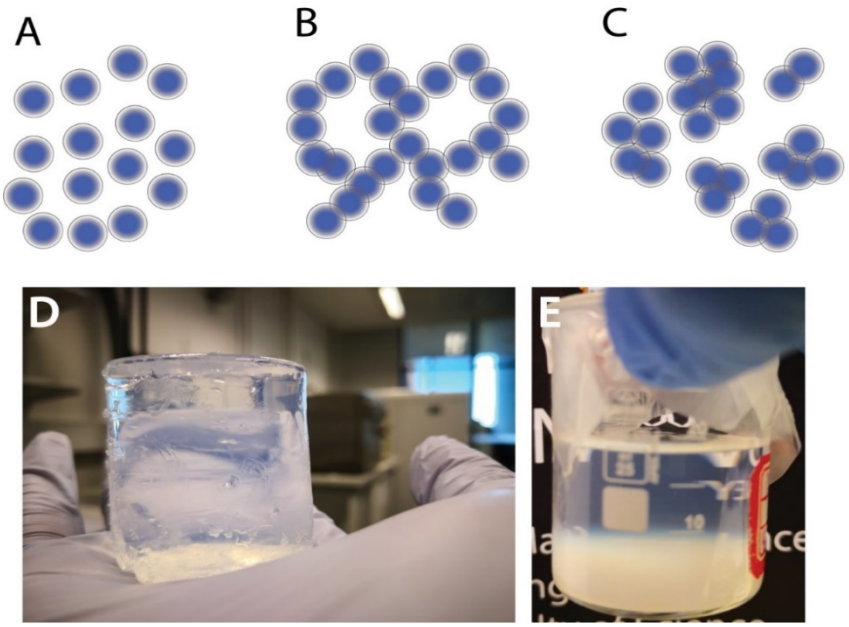

Figure 31. A-C Structure differences among sol, gelation, and precipitation from a sol. D The image of silica gel from sol one after 60 days of aging time at room temperature. E The precipitation from sol ten after 60 aging days at room temperature.

shows only one peak and with a low PDI. Therefore, we prefer to give an analysis and explanation of this phenomenon from the OA theory. In the inset image (Figure 30), polymerization of the small monomers or oligomers occurs most rapidly near the points (arrow mark) of contact between these two particles in the agglomerates because of the solubility difference induced by the negative radius of curvature[182, 188, 189]. We believe the nucleation happened throughout the ripening process, but once the nuclei concentration is up to a limitation at which the growth dominants the ripening while the

nucleation decays to insignificant levels[190], the monomer or oligomer addition drives the growth of silica particle or aggregates.

In practical observation by naked eyes and TEM, the solution 2-9 transform into silica sol with uniform particle distribution and high stability with the aging time from the first day to the fourteenth day. However, the transition of sol to gel should be distinguished from a precipitation mechanism in which separate aggregates are formed in contrast to the continuous three-dimensional particle network. The silica solution 10 after 60 days at room temperature appears an evident stratification in Figure 31 image E. The bottom layer is the larger silica particles (>100nm) which settle down suffering from the imbalance between the particle interaction and system steric hindrance. In the solution 10 with a molar ratio of NH^{4+} and TEOS up to 1.18, the reaction of hydrolysis and condensation goes faster than all previous solution, but the nucleation and growth occur all the time. After the solution converted into the sol completely, the aggregation is still going forward due to there still are enough NH^{4+} and hydroxy group[191]. The increasing particle size (more than 100nm in diameter) eventually broke the balance between the particle interaction and steric hindrance, which further lead to precipitation happens.

We conclude that, while not fully understood, reactions occur in the base solution which give rise to the transition from silica sol to gel or precipitation and that these reactions mechanism can be explained by the synergy between the monomer addition model[164] and aggregation model[191]. A stable sol system relies on the balance between the particle interaction and steric hindrance, which can be achieved by precise control of base catalyst and aging time.

4.3 Summary

It has been demonstrated that the ammonia catalyst controlling sol system can be easily used to obtain a stable silica sol with uniform particle distribution and wide selected size range. The experimental results indicate that the initial pH value of the synthesis system is the main factor affecting the particle size in the sol. The pH change performed by adjusting the mole ratio n_{NH4+}/n_{TEOS}, which ranged from 0.28 to 1.18, results in a great change of particle size (10-100nm in diameter). For a sol system sustaining for longer than 60 days, the ratio range should be narrowed down to 0.33-0.98 while the mole ratio among other raw materials including TEOS, Ethanol, DI water are fixed. Nevertheless, to confirm our observation and to qualitatively study the catalyst effect on the formation of silica sol and the conversion from suspension to sol or gel, further spectroscopic investigation (NMR, FTIR, BET, etc.) needs to be carried out. The as-made silica sol can be applied to the fabrication of silica thin film combining with other coating technologies. The results showed that the particle size vs. catalyst concentration might be a key parameter to monitor when searching for an optimal coating solution for thin film deposition.

Chapter 5 Design and simulation of Silica-based Antireflection coating system by spectroscopic ellipsometry & WVASE software package

5.1 Introduction

The development of optical-electrical technology and micro electricity extend the application of thin-film, which is defined as a layer of material of thickness ranging from hundreds to even tens of nanometres. The physical thickness and optical constants (refractive index and extinction coefficient) determine the thin film optical properties involving transmission, reflection, absorption and etc. Silica thin film plays a significant role in the field of microelectronics, particularly in silicon solar cell technology, due to its feature of low absorption, unique structure, high thermal stability, excellent corrosive resistance, and etc. Silica thin film is the only reliable material which is able to lower the Si surface electronic state levels to ensure high quality and reliable device operation (below 10^{10}•ev^{-1}•cm^{-2})[192, 193]. Needless to say, the accurate acquisition of silica thickness and optical constants is essential, and the most common and reliable technique is Ellipsometry[194]. As we discussed in Chapter 3.4.3, accurate and reliable results (optical constants) are critically dependent on a proper modeling of the physical sample. For example, D. E. Aspnes et al. [195] carried out a comparative study on the microscopic surface roughness by spectroscopic ellipsometry with different effective medium approximation (EMA) theory, involving Bruggeman[196], Maxwell Garnett(MG)[197], and etc. In this work, spectroscopic ellipsometry is applied to the determination of the refractive index of the soda-lime glass substrate by Cauchy model and exploratory research for the feasibility of silica-based porous structured antireflection coatings on soda-lime glass with the aid of Bruggeman EMA theory.

5.2 Selection of the method (Cauchy model, Effective medium approximations)

As we already discussed in part four-chapter three, the experimental data derived from ellipsometry are expressed as psi (ψ) and delta (Δ), where ψ is the ratio of the amplitude diminutions, and Δ is the phase difference before and after the reflection. Having accomplished a measurement, the establishment of a physical model is a critical step for acquisition of the thickness and optical constants. The physical model consists of wavelength range and angle of the incident light, the polarization state of the incident beam, and also some parameters to be measured such as physical thickness, refractive index and extinction coefficiency. After the development of a physical model, a fitting process will be performed to vary the unknown parameters and make the generated data to match with the experimental data. The evaluation of the fit results is defined by the mean squared error (MSE), only if the minimum MSE value is within an acceptable range, the fit results can be regarded as the approximate value to real materials.

The absolute refractive index of a material can be defined as the ratio of the light speed in vacuum to the speed in the material, which can be written as $n = {}^{c}/_{v}$. The Maxwell theory relates the light speed, materials' permittivity(ε) and permeability(μ) by $v = 1/\sqrt{\varepsilon\mu}$, which reveals that the material properties affect light transmission. Combined above two equations, there is $n = {}^{c}/_{v} = \sqrt{\varepsilon\mu}/\sqrt{\varepsilon_0\mu_0} = \sqrt{\varepsilon_r\mu_r}$, where ε_r, μ_r are the relative permittivity and relative permeability. Except for magnetic materials, most materials have $\mu \approx \mu 0$, $\mu_r = 1$. Therefore, it is customary to introduce $n \approx \sqrt{\varepsilon_r}$. Initially, the development of effective medium approximation theory is usually ascribed to MG [198] and Bruggeman[196]. They proposed different mixing formulas which aim to give an

effective electric permittivity of the heterogeneous medium in terms of the permittivity and volume proportions of the individual constituents. Their difference is the choice of host materials, and this will be explained in the next few sections. Based on the relationship between the refractive index and electric permittivity, the MG and Bruggeman EMA theory is usually applied into the optical modeling.

Cauchy model

The Cauchy model is typically used for transparent materials in visible wavelength range at which the absorption can be ignored. The refractive index n and can be connected with wavelength (in nm) via following Cauchy dispersion equation:

$$\begin{cases} n = A + {}^{B}/_{\lambda^2} + {}^{C}/_{\lambda^4} \\ k(\lambda) = 0 \end{cases} \tag{5}$$

Where A, B, C do not have any physical meaning, the k represents the extinction coefficient that equals to zero when the material has no optical absorption in the visible wavelength range. The parameters in Cauchy dispersion formulation are empirically linked with each other, and they do not consist of Kramers-Kronig relations. Therefore, the Cauchy formulation cannot be directly applied to the metals and semiconductors. In addition, the Cauchy model presented above can only be used for evaluating the approximated thickness and refractive index, whereas the absorption coefficient cannot be obtained. For weakly absorbing materials, the non-zero absorption coefficient expression can be upgraded into the above Cauchy equation, and then, a new Cauchy dispersion formulation can be given as:

$$\begin{cases} n = A + {}^{B}/_{\lambda^2} + {}^{C}/_{\lambda^4} \\ k(\lambda) = 10^{-5}D + 10^{4}E/\lambda^2 + 10^{9}F/\lambda^4 \end{cases} \tag{6}$$

In this work, the Cauchy model may not be suited for modeling the nano-porous structure silica thin film, but it can be used as a good starting point for building a model for soda-lime glass substrate.

Effective medium approximations

The effective medium approximation is developed to model the effective electric permittivity of heterogeneous media, which is treated as homogeneous media. The relationship between the permittivity and refractive index introduced this approximation into the modeling of optical constants of heterogeneous materials. There gives a brief introduction of the most common use models involves Maxwell-Garnett, Bruggeman.

Maxwell-Garnett:

$$\frac{\left(n_{eff}^2-n_1^2\right)}{\left(n_{eff}^2+2n_1^2\right)}=(1-f_1)\frac{(n_2^2-n_1^2)}{(n_2^2+2n_1^2)} \tag{7}$$

Where n1 and n2 are the RIs of two constituent layers, f_1 and f_2 (=1-f_1) are the corresponding volume fractions. It should be noted that, in the case of MG model (equation 11), the layer (RI=n_2) is regarded as an inclusion layer surrounded by the host material (RI=n_1). The refractive index of the effective medium has different values if n_1 is interchanged with n_2 even though the relative proportion remains unchanged. Also, the MG model is limited by the volume fraction which should not be more than 52% due to that the spheres start overlapping occur beyond that value [199]. But the MG model is the most realistic in the condition of the host material occupying the absolute dominant fraction compared with inclusions.

Bruggeman:

$$f_1 \frac{\left(n_1^2 - n_{eff}^2\right)}{\left(n_1^2 + 2n_{eff}^2\right)} + f_2 \frac{\left(n_2^2 - n_{eff}^2\right)}{\left(n_2^2 + 2n_{eff}^2\right)} = 0 \quad (8)$$

The MG model is restricted by the limited range of porosities, while Bruggeman considered to let the effective medium layer act as a host material and replace ε_1 host material with ε_{eff}, and the Bruggeman equation can be derived with the further substitution of the ε_r by n^2. Unlike from the MG model, the Bruggeman model is self-consistent due to no concerning of the highest constituent fraction of the component. It is good to make up the limitation of the MG model when there is no constituent to forms a clear majority of the materials. It has been demonstrated the reliability and capability of the Bruggeman EMA to deal with the modeling of surface roughness[200]. Also, the incorporation of multilayer Bruggeman EMA with different proportion of void and underlying material can be used to model a thick surface layer[201].

Figures of Merit

As introduced in Figure 20 (B), after chosen of a model, the parameters fitting is the critical process to determine film thickness and optical constants. However, the fitting process is not the last step, and it should provide not only the fitted results but also relevant error estimates and a statistical measure of goodness of fit. If the last two items suggest the model is not suited for the measurement data, then we may need to reconsider the choice of the physical model. The evaluation of the fitted results is expressed by Figures of Merit, which normally involves the mean squared error (MSE) and the reduced χ^2. The corresponding calculation formula is given as follows:

$$MSE = \sqrt{{}^{1}/_{(2N-M)} \sum_{i=1}^{N} \left(\frac{\psi_i^{mod} - \psi_i^{exp}}{\sigma_{\psi,\mathrm{i}}^{exp}} \right)^2 + \left(\frac{\Delta_i^{mod} - \Delta_i^{exp}}{\sigma_{\Delta,\mathrm{i}}^{exp}} \right)^2} = \sqrt{{}^{1}/_{(2N-M)} \chi^2} \quad (9)$$

In the above equation, N is the number of measured data points (psi (ψ) and delta (Δ) pairs), and the number of fit parameters[194] is M. The ψ_i^{exp} and Δ_i^{exp} are the experimental data point taken at λ_i wavelength while the ψ_i^{mod}, Δ_i^{mod} are calculated from the chosen model based on the same experimental parameter at λ_i wavelength. The

Table 7. The MSE calculation based on different fit weighting schemes.

Fit weighting	**The mean squared error (MSE)**
Experimental Standard Deviation	$\sqrt{{}^{1}/_{(2N-M)} \sum_{i=1}^{N} \left(\frac{\psi_i^{mod} - \psi_i^{exp}}{\sigma_{\psi,\mathrm{i}}^{exp}} \right)^2 + \left(\frac{\Delta_i^{mod} - \Delta_i^{exp}}{\sigma_{\Delta,\mathrm{i}}^{exp}} \right)^2}$
Psi and Delta	$\sqrt{{}^{1}/_{(2N-M)} \sum_{i=1}^{N} \left(\frac{\psi_i^{mod} - \psi_i^{exp}}{1} \right)^2 + \left(\frac{\Delta_i^{mod} - \Delta_i^{exp}}{1} \right)^2}$
Tan (Psi) and Cos (Delta)	$\sqrt{{}^{1}/_{(2N-M)} \sum_{i=1}^{N} \left[\left(\tan\psi_i^{mod} - \tan\psi_i^{exp} \right)^2 + \left(\cos\Delta_i^{mod} - \cos\Delta_i^{exp} \right)^2 \right]}$
Psi only	$\sqrt{{}^{1}/_{(N-M)} \sum_{i=1}^{N} \left(\psi_i^{mod} - \psi_i^{exp} \right)^2}$
Cos (Delta) only	$\sqrt{{}^{1}/_{(N-M)} \sum_{i=1}^{N} \left(\left(\cos\Delta_i^{mod} - \cos\Delta_i^{exp} \right)^2 \right)}$

calculated data ψ_i^{mod}, Δ_i^{mod} are denoted by $y(x_i,\vec{a})$, where the x_i includes all model parameters (physical thickness, angle of incidence, optical constants) and $\vec{a}$ consists of all variable model parameters. $\sigma_{\psi,\mathrm{i}}^{exp}$ and $\sigma_{\Delta,\mathrm{i}}^{exp}$ represent for the experimental standard deviation of every single point. Therefore, a noisy measurement corresponds to a larger standard deviation, which will not be strongly weighted in the fit. Moreover, the fit-

weight, the numerator in the equation, can be adjusted to several other kinds of schemes such as, Psi and Delta(equation 1), Tan(Psi) and Cos(Delta) (equation 1), Psi only (equation 1), Cos(Delta) only (equation 1), etc., as shown in Figure 32. The MSE calculation based on various weighting schemes has been summarized in Table 7. For the weighting schemes which "Psi and Delta" is chosen, the standard deviation is replaced by 1 for all measured data, compared with the schemes using experimental standard deviation as fit weight, the former mode places a heavier weight on Δ value than ψ. In the "Tan (Psi) and Cos (Delta)" weighting scheme, the MSE calculation is associated with Tan ψ and Cos Δ. The MSE is calculated with respect to ψ value and cos Δ in "Psi only" and "Cos (Delta) only" mode respectively.

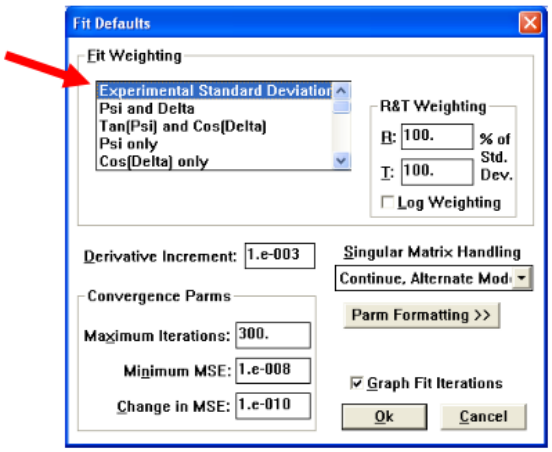

Figure 32. The Fit Defaults dialog box.

5.3 Spectroscopic ellipsometry characterization of the soda-lime glass substrate

To build an optical thin film coating system, we start from the substrate. The substrate here we are using is soda-lime glass. In general, the refractive index of glass is above 1.52, which is an average value in the visible range as the refractive index is various for different wavelength light. Moreover, the refractive index of glass can be different because of the ratio of the elements or ions. Therefore, the spectroscopic ellipsometry is applied to the study of the soda-lime glass optical constant. The basic working principle and procedure of the instrument have been introduced in chapter 4. The following describes how we got the optical constant of the soda-lime glass.

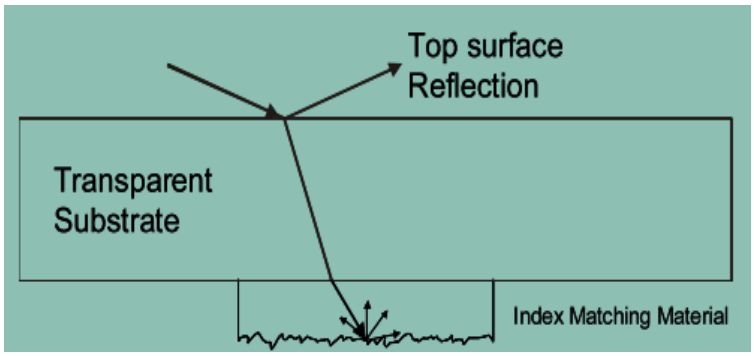

Figure 33. Suppress backside reflections from transparent substrates via index matching with semi-solid materials.

Ellipsometry measures the change in the polarization state of light reflected from (or transmitted through) the surface of a sample. Therefore, the back reflection which occurs in the backside is unwanted because it may overlap the front reflected light which is desired to be detected. To eliminate the backside reflection, we adhere the backside with scotch tape, which is rough and has a similar refractive index as soda-lime glass[202]. In this way, the light hitting the backside of the glass would be scattered and transmitted out, as shown in Figure 33. The incident beams ranged from 380 to 800nm, hit the substrate

with three different angles, 55° 65° 75°, in such a way to obtain more spectroscopic data (φ-Δ) allows for fitting with the Cauchy dispersion model.

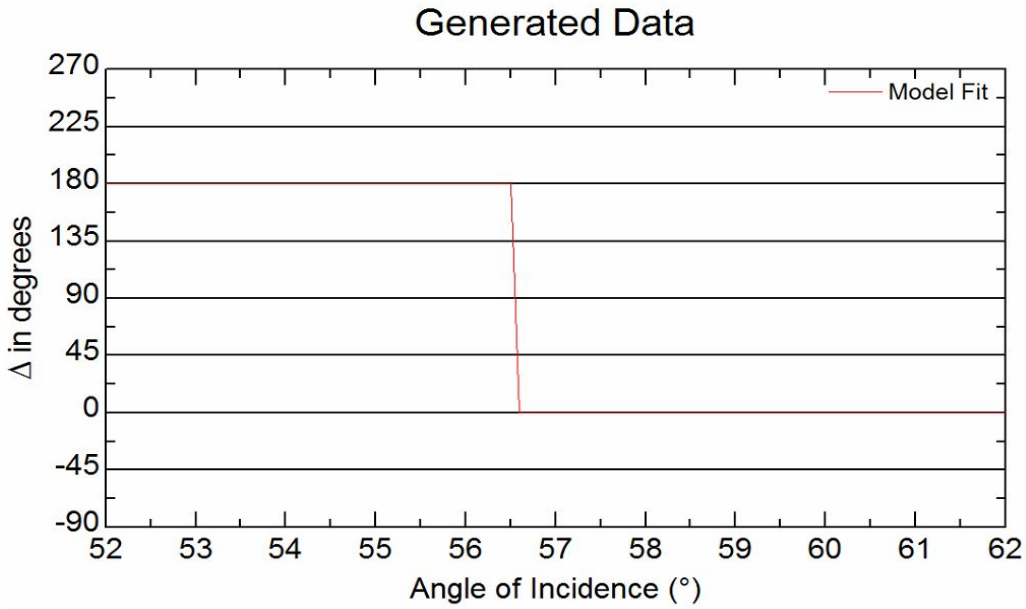

Figure 34. The change of delta data calculated from the soda lime glass model layer based on Cauchy dispersion over angle of incidence (52-62°).

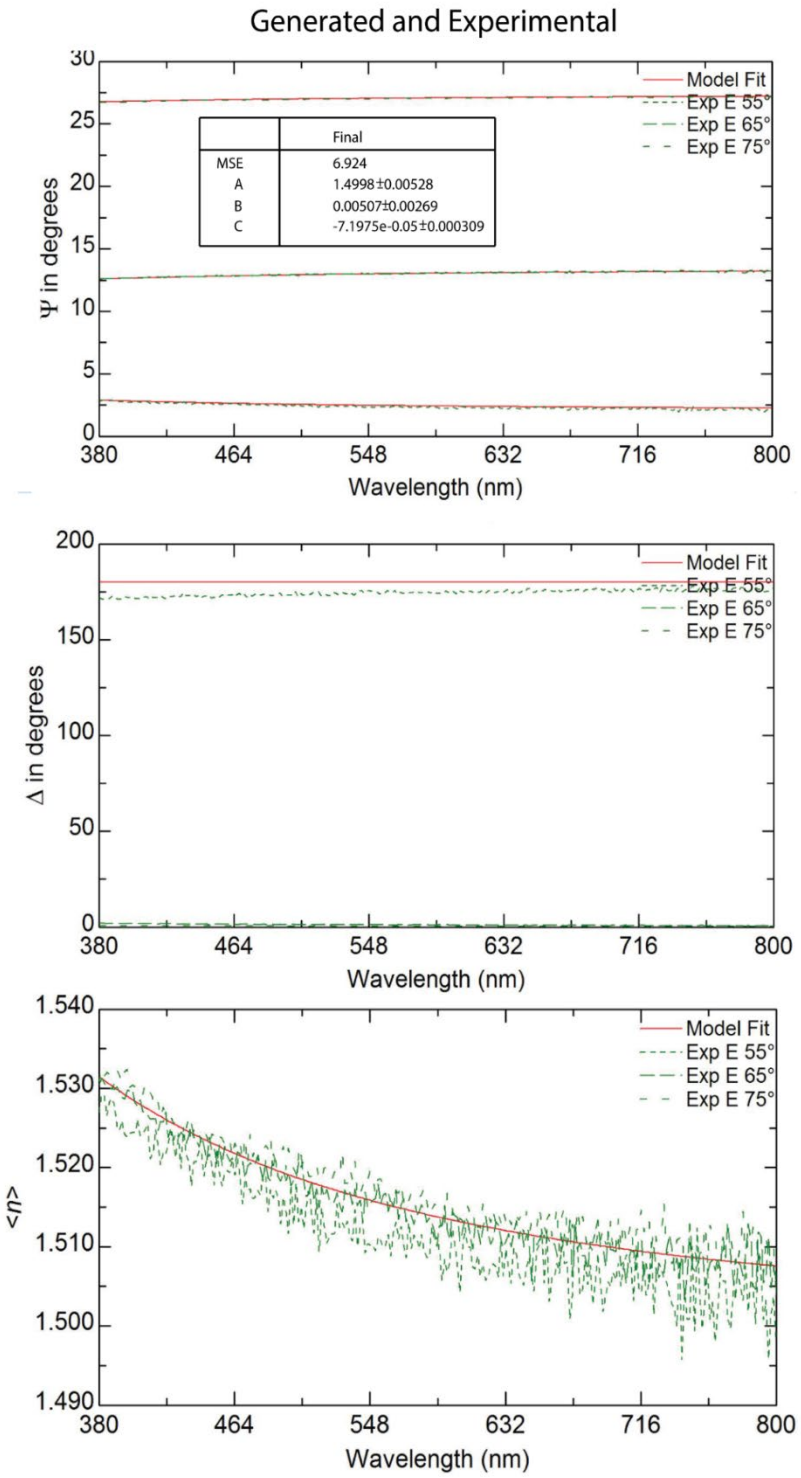

Figure 35. Generated and experimental ellipsometry φ-Δ and refractive index data from soda lime glass.

The input thickness is 1.3mm measured by Micrometer. The experimental φ-Δ-n data and the fitting curves based on Cauchy model shows in Figure 35. In general, the reflection coming from the backside of the glass will lead to three features in the psi and delta

spectra, the first is a jump which occurs in the psi spectra at 320nm wavelength, the second is a constant offset of the delta at wavelength greater than 320nm, and the last is the offset almost similar at different incident of angle. In Figure 35, the experimental psi spectra match well with the modeling data, no evident jump at ~320nm or offset neither. However, the delta spectrum does not fit well with the modeling spectrum (180°) at an incident of angle 55°. The delta spectra dependent on the angle of incidence has been presented in Figure 34, wherein the brewster angle of soda-lime glass is approximately 56.5°. Therefore, in theory, the delta spectra should always be either 180° (at the angle of incidence lower than 56.5°) or 0° (at the angle of incidence greater than 56.5°). The

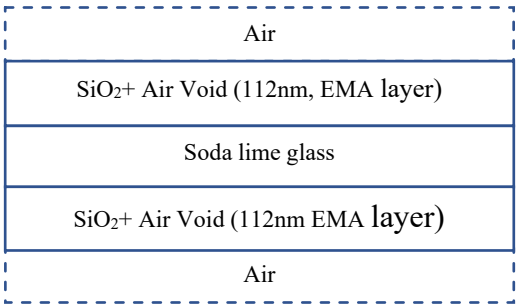

Figure 36. The three-layer optical model of the double-side EMA layer with fixed 112nm thickness.

deviation between experimental delta spectrum and modeling spectrum may be attributed by the effect of instrument noise and backside reflection. Nevertheless, the final Mean squared error (MSE) is 6.9, which is still within the acceptable thresholds (15). Thus, the average refractive index of the soda-lime glass we used is 1.52 with the wavelength in the range of 380 to 800nm. The optical constants and thickness of the soda-lime glass are saved as a layer model for further AR coating system design.

5.4 Design single layer silica antireflection coating: Effective Medium Approximations

Now we have already obtained the optical constant of soda-lime glass. For single-layer antireflection coatings, there are two requirements, the thickness and refractive index. The mechanism of AR coatings is based on the deconstructive phase matching of beams reflected from the coating surface and the coating-substrate interface. Here we aim to

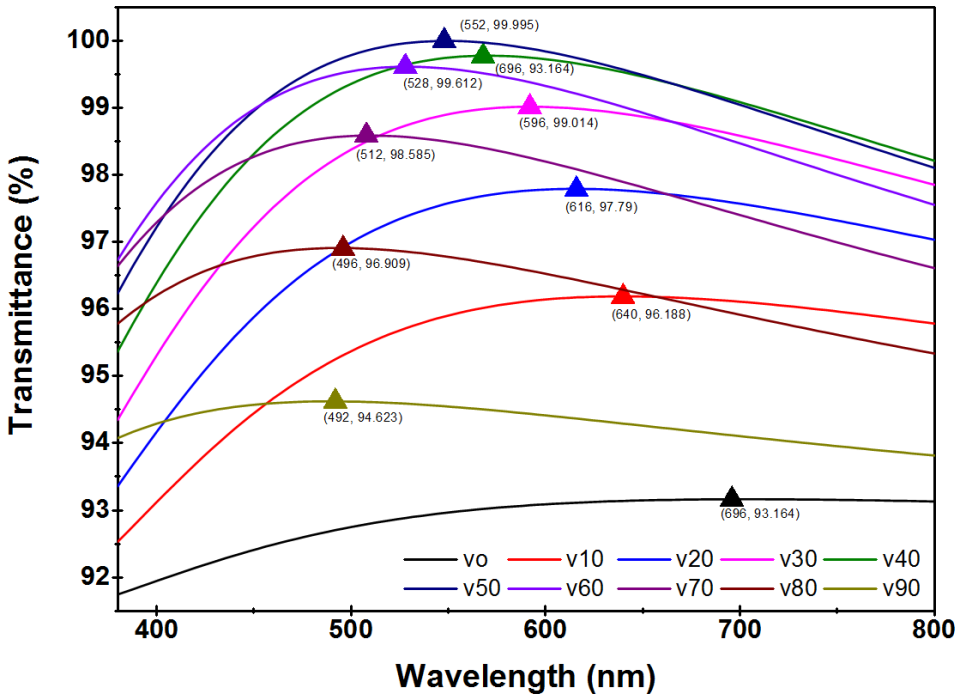

Figure 37. The Total Transmittance spectra of double side coated porous silica mixed with different percentage of air void based on Bruggeman Effective Medium Approximations.

design an AR coating at the interface between air (n_{air}=1) and the soda-lime glass slides (n_{sub}=1.52). For a representative wavelength of 550 nm (the best-resolved color and most readily distinguished wavelength perceived by human eyes), the optimal conditions for maximum transmission of specular incident light would be $n_c = (n_{air} n_{sub})^{1/2} = (1*1.52)^{1/2} = 1.23$ and $d = \lambda/4n_c = 550/4*1.23 = 112$nm. The three-layer

model was created (Figure 36), the middle layer is a soda-lime glass layer, and the top and bottom layers are silica coating. In the modeling, the thermal silica [203] was regarded as the dense silica layer with 0% void, with the average refractive index above 1.46 in the visible wavelength range.

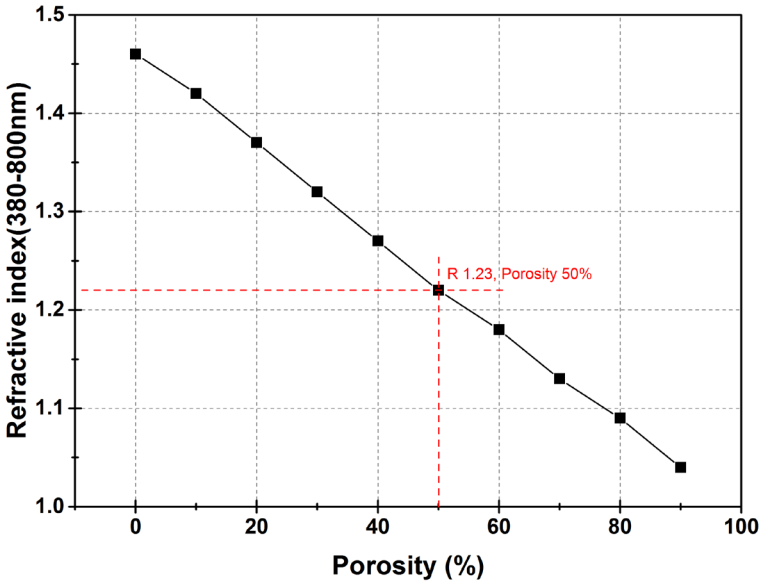

Figure 38. The Bruggeman EMA theory derived the average refractive index of silica mixed with different percentage of air void.

Our strategy is to impart porosity to the dense silica film and to lower the refractive index. Here we introduced Bruggeman Effective Medium Approximations (EMA) dispersion models to simulate the pore effect on the refractive index[204]. The Effective Refractive index n_{eff} can be calculated based on the Bruggeman approximation equation[196].

The thickness was fixed at 112nm and the transmittance over visible range changes as the porosity change. The modeling results have been illustrated in Figure 37, and the transmittance peak increases first and decreases afterward with the overall shift to blue, and the highest value goes up to 99.99% when the air void accounts for 50%. In Figure 38, it shows a good linear relation between RI and porosity (air void percentage), and

when the porosity increases, the RI decreases. It is noteworthy that the refractive index goes down to the ideal value 1.23 when the porosity is up to 50%, which is consistent with the transmittance spectra movement in Figure 37. Therefore, the desired porosity can be determined preliminarily. Fixing the air void percentage as 50%, a new model, double side coated porous silica layer on soda-lime glass, was created, and it has been

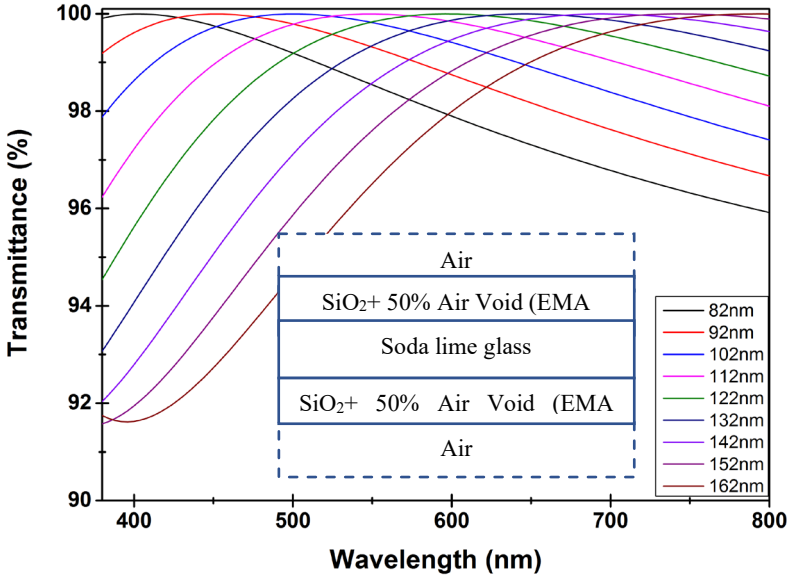

Figure 39. The Total Transmittance spectra of double side coated porous silica (silica + 50% air void) on soda-lime glass with varying thickness based on Bruggeman Effective Medium Approximations

evaluated that the transmittance spectra (380-800nm) change in series of thickness. The simulating results were presented in Figure 39, in which we can see that transmittance peaks of all curves are up to 99.99%, and the corresponding wavelength λ is close to 4nd referring to Fresnel law. The peak with the highest transmittance moves to longer wavelength with the thickness increase. When the porous silica thin film thickness reaches 112nm, the range of transmittance of 99.99% moves to 548-552nm. Therefore, the optimal parameter of a double-side coated single layer silica antireflective coating is expected to involve 50% porosity and 112nm in thickness. The movement of the

transmittance spectra is mainly influenced by the film thickness and optical constants (refractive index, the absorption in visible range has been ignored). The spectra red or blue shift can be controlled by the adjustment of thickness while the adjustment of the refractive index can result in the spectra up and down movement, and also the red and blue shifting.

5.5 Summary

In this chapter, we obtained the refractive index of the soda-lime glass substrate referring to Cauchy dispersion physical model by spectroscopic ellipsometry, and the backside reflection has been efficiently eliminated by the utilization of scotch tape which matches well with glass in refractive index. More importantly, the theoretical discussion among several optical models involving Cauchy dispersion model, Bruggeman and Maxwell Garnett EMA models gave an idea for the modeling of porous silica layer on a glass substrate. Then, the Bruggeman EMA model was chosen for pre-study of the thickness and void effect on the Antireflective performance of the double-side coated porous silica soda-lime glass. It was found that the thickness of 112nm and void percentage of 50% is the optimal parameter for 99.99% transmittance at the wavelength of 550nm. This work has guiding significance for the further fabrication and improvement of porous silica AR coating on the glass.

Chapter 6 Fabrication of silica-based antireflection coatings and evaporation induced self-assembly behavior in dip coating

Referring to the simulation results in chapter 5, the achievement of ideal antireflection (> 99.99%) at a wavelength of 550nm for porous silica AR coating on the glass substrate requires precise control of thickness and porosity, which is determined to be ~112nm and around 50% respectively. Chapter 4 gave a demonstration that the silica particle size can be tailed well ranging from 10-90 nm in diameter, and the SEM characterization and BJH isotherm results provided the feasibility of the porosity control by solvent evaporation induced particle aggregation. Therefore, we decide to adopt the sol-gel combined dip-coating process to fabricate silica-based antireflection coatings on the glass substrate.

6.1 Experimental Procedures

Preparation of the AR Coating

The coating substrate is soda-lime glass slide (LIVINGSTONE MICROSCOPE), which was cleaned by deionized water and followed by 15mins UV irradiation on each side. Then the cleaned glass slide was coated with silica sol by the dip-coating method (ND-DC 11/1 300 Dip Coater, Nadetech Innovations), with 40-120mm/min withdraw speed (room temperature 25℃; relative humidity<40%). After the coating process, the coated glass was annealed at 180 ℃ on Forced Convection Oven (DKM300) for 3 hours.

Hydrophobic Modification Process

To obtain hydrophobic surface, PTOS was attached on the AR coating by a simple chemical vapor deposition (CVD).[205] The annealed coated glass slide was placed into

a Teflon container, and on the bottom of which was dropped 20ul PTOS, then the container was sealed in a stainless-steel autoclave. The sealed autoclave was heated at 120℃ on Forced Convection Oven (DKM300) for 3 hours. After the heat treatment, the coated glass slide was taken out from the container, heated at 120℃ for 1 hour to remove the unreacted PTOS molecules on the AR coating. Finally, the AR has attached PTOS molecules on both sides.

Characterization

Scanning electron microscopy (Nano-SEM 450, a field-emission scanning electron microscope) operated at 5.00 kV was used to observe the surface morphology coated with 5nm of gold-palladium or platinum at low vacuum. The Transmittance in the wave range of 380-1100nm of the coated glass was carried out using a PerkinElmer 950 UV/Vis Spectrophotometer with 4nm scanning interval. The surface topography and thickness of the coating were characterized by AFM (Bruker Dimension ICON SPM) operated in tapping mode and scan mode, respectively. The thickness and refractive index of the silica thin film on the soda-lime glass substrate were measured by ellipsometry (J A Woollam spectroscopic ellipsometer). The angle of incidence was fixed at 70° (from the normal), and the spectral range probed was 380-1100 nm. Moreover, to determine the accurate thickness of the silica thin film, the cross-section of the coating on the glass was made by high resolution focussed ion beam (FEI XT Nova NanoLab 200) and then measured by the Philips CM200 field emission transmission electron microscope.

6.2 Results and Discussion

6.2.1 Study of the particle size effect on Refractive index of the coating.

To study the refractive index of the coating from different silica sols, we covered one side of the soda-lime glass with polyimide film tape and then got one side coating by dip coater with 40mm/min withdraw speed, drying in Forced Convection Oven at 100 degrees for 3 hours. After that, we use spectroscopic ellipsometry to characterize the refractive index

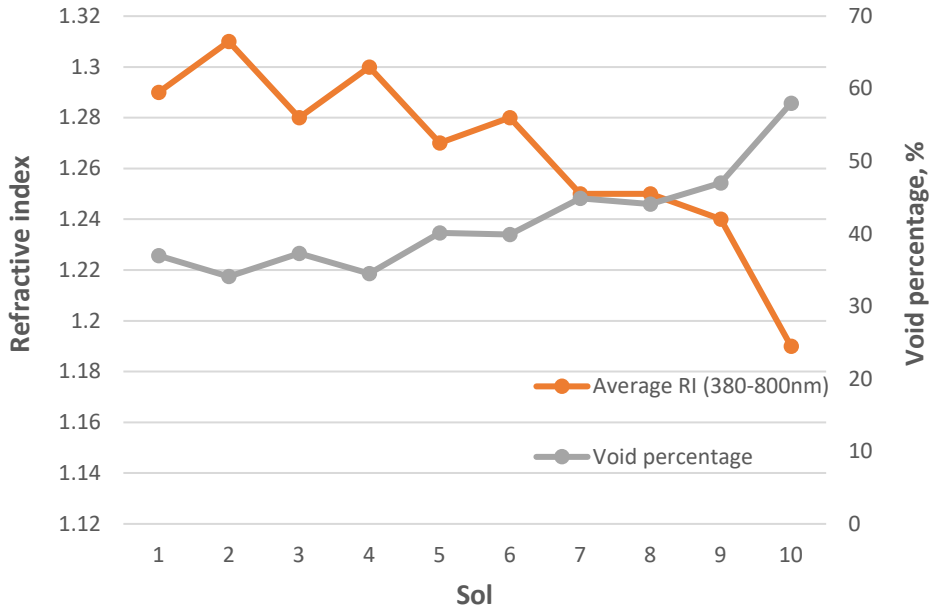

Figure 40. The ellipsometry fitting results of average refractive index (380-800nm) and void percentage of the thin film derived from various silica sol.

of the film and corresponding thickness, and porosity. To eliminate the backside reflection on the glass-air interference, we pulled the polyimide tape off and replaced with scotch tape, which is rough and has a similar refractive index as soda-lime glass[202]. The φ-Δ data from ellipsometry are fitted by using the VASE software (J.A Woollam Co.). Here we built two layers. The bottom layer represents the glass substrate, and the top layer is the silica film. The refractive index of glass layer can be obtained by

measuring corresponding φ-Δ data from ellipsometry and fitted by Cauchy mode ($n(\lambda)=A+B/\lambda^2+C/\lambda^4$) in the waveband of 380 to 800 nm. The effective medium approximation (EMA) layer was applied to simulate the porous silica layer coating on glass[195, 206]. The EMA layer is a homogenous layer made by two different materials,

Table 8. Fitting data from Ellipsometry (Void percentage, Average refractive index, Film thickness), Experimental results based on equation 1[3], Film thickness from AFM.

Sample	Sols	Ellipsometry			Calculated results	AFM
		Void percentage	Average RI (380-800nm)	Film thickness	Void percentage	Film thickness
S1W40	1	37.0%	1.29	87.0	41.0%	90.0
S2W40	2	34.1%	1.31	77.1	36.7%	63.7
S3W40	3	37.3%	1.28	63.8	43.6%	63.9
S4W40	4	34.5%	1.3	77.5	39.0%	63.2
S5W40	5	40.1%	1.27	64.7	45.8%	64.9
S6W40	6	39.9%	1.28	67.2	43.6%	69.0
S7W40	7	44.9%	1.25	64.6	50.0%	50.0
S8W40	8	44.1%	1.25	55.8	50.0%	50.0
S9W40	9	47.0%	1.24	63.2	52.0%	61.8
S10W40	10	58.0%	1.19	70.0	63.0%	78.3

the dense silica and void. Therefore, the fitting parameters include film thickness, the percentage of silica and void. The fitting results extracted from ellipsometer can be seen the Table 8. The void percentage of coating film presents a trend of rising, which can be seen in Figure 40, the coating film prepared from sol 10 wherein the silica particles size are the largest exhibits a high porosity of 58%. The average refractive index of the coating

film from sol 10 is 1.19 which is apparently lower than the film derived from sol 1 and 2 (1.29, 1.31 respectively.). The main difference among those sol is the silica particle size. Therefore, the changing of particle size does have a great effect on the film structure and refractive index.

6.2.2 Self-assembly of silica particle during the sol-gel combined dip-coating process

To understand the size effect on the deposited film structure on the substrate, we should give priority to the assemble behavior of the silica particle on the glass substrate during dip coating. The dip-coating process can be divided into several stages: Immersion & dwell time, Deposition & Drainage, Evaporation. Within the thinning coating, the silica sol is rapidly concentrated by gravitational draining with concurrent evaporation, leading to silica particle aggregation, gelation, and final drying to form deposited film[27], the progress has been shown in Figure 41. The SEM images in Figure 42 e-f-g shows the tilt-view and top-view of the silica coating, S1W40, S6W40, S10W40. The top-view SEM image of the coating built by multilayer silica particle as

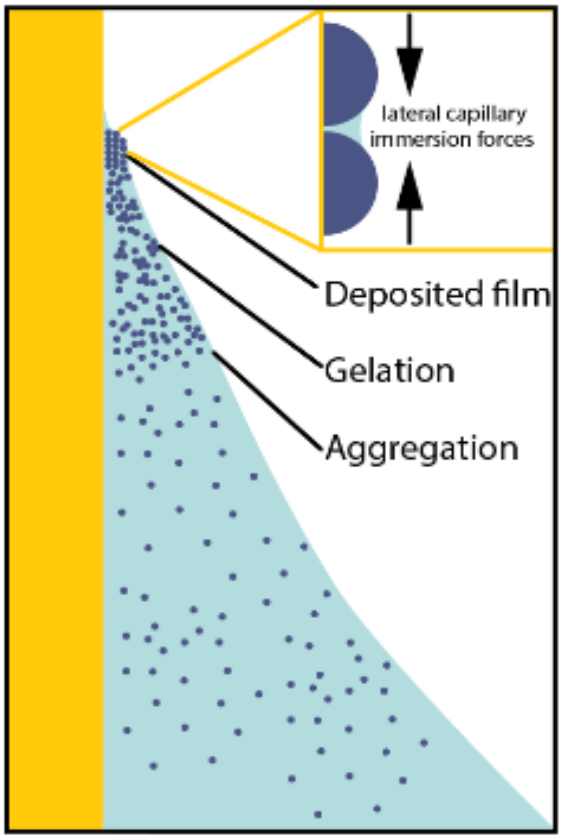

Figure 41. Schematic of the evaporation induced self-assembly dip-coating process, the inset shows the menisci shape between neighboring particles.

the tilt-view is shown. In the top-view SEM images, we can see Sample S1W40 reveals a dense silica coating whereas there are more pores in S6W40 and S10W40. It agrees well with the fitting results, which are 37%, 39.9%, 58% corresponding to S1W40, S6W40, S10W40 respectively. In our experiment, considering the high evaporation speed of the silica sol, which contains more than 80% ethanol, there is little time available for silica particles to "find" low energy configurations. Thus, the deposited film structure is dominated by physical gelation and drying steps, which are mainly driven first by evaporation and then by the capillary pressure[207]. The capillary pressure is a strong driving force to pull the neighboring particles closer as shown in the inset in Figure 41. Generally, the magnitude of the capillary pressure is estimated by the Laplace equation[169]:

$$P_C = \frac{2\gamma_{Lv}\cos(\theta)}{r_p} \tag{10}$$

Where Pc is the capillary pressure, γ_{Lv} is the liquid and vapor surface tension, θ is the wetting angle, and r_P is the pore size. With the evaporation of the solvent, the void percentage increases and causes the bulk modulus K to increase as a power law[170]. The final thickness and pore size of the film were established until the modulus of the film is high enough to balance the capillary pressure[207]. Therefore, the smaller pore size, the larger capillary pressure is, and the particle packing tends to be denser. Comprehensively considering the previous TEM, SEM results, and above analyzing, it was anticipated that the void percentage increases with the silica particle size, which results in lower RI of the coating film (Table 8). Another interesting finding is that the sol with larger particle size is more likely to obtain a monolayer particle array as the S10W40 tilt-view shows, this may be explained by the decrease of the lateral capillary forces which push the particles to stick together[208].

In general, there are two equations which can be used to simulate or predict the thickness of film during the dip-coating process, capillary regime equation[209] and Landau-Levich equation[210]. The plot of simulated thickness versus withdrawal speed has been illustrated in Figure 43A, which gives three lines: the blue dash line is given by capillary model, the red dash line represents for draining model, and the black line is the

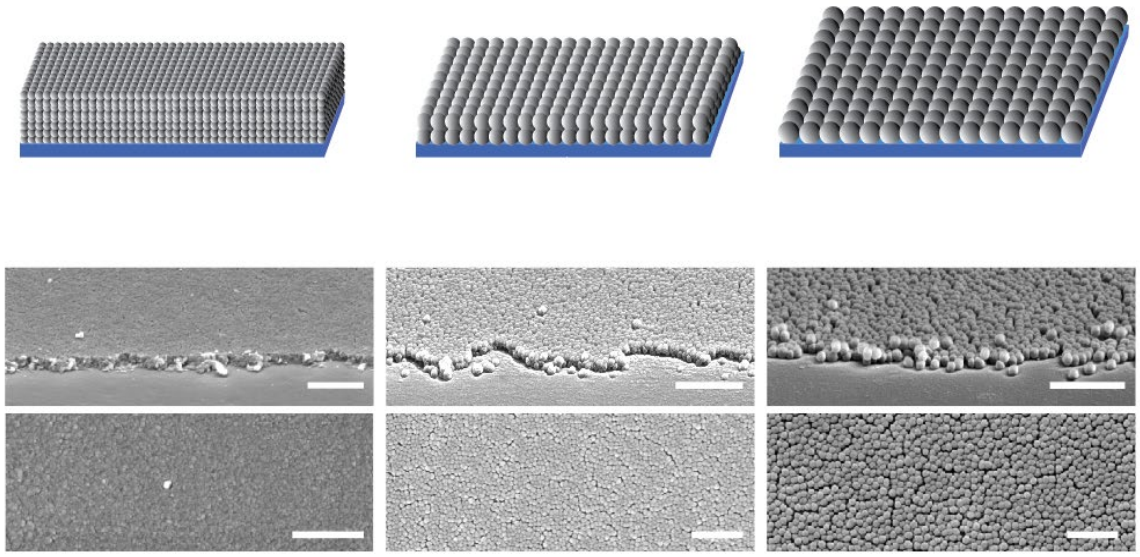

Figure 42. The model of multilayer(a), double layer(b), monolayer(c) silica coating on glass. The SEM images of deposited silica film derived from (e) sol 1, (f) sol 6, (g) sol 10, where the upper pane is the tilt view and the bottom pane is the top view, by dip c coating process at 40mm/min withdrawal speed. Scale bars 500 nm.

cooperation results unified of two models. Our experimental results showing the evolution of film thickness with withdrawal speed are given by Figure 43B. Apparently, the observed tendency of thickness with withdrawal speed fits better the draining model. Therefore, we prefer to think about the film thickness is mainly controlled by the draining

process. In addition, the thickness result got from AFM performed in scan mode closely matches the fitting data by WVASE software.

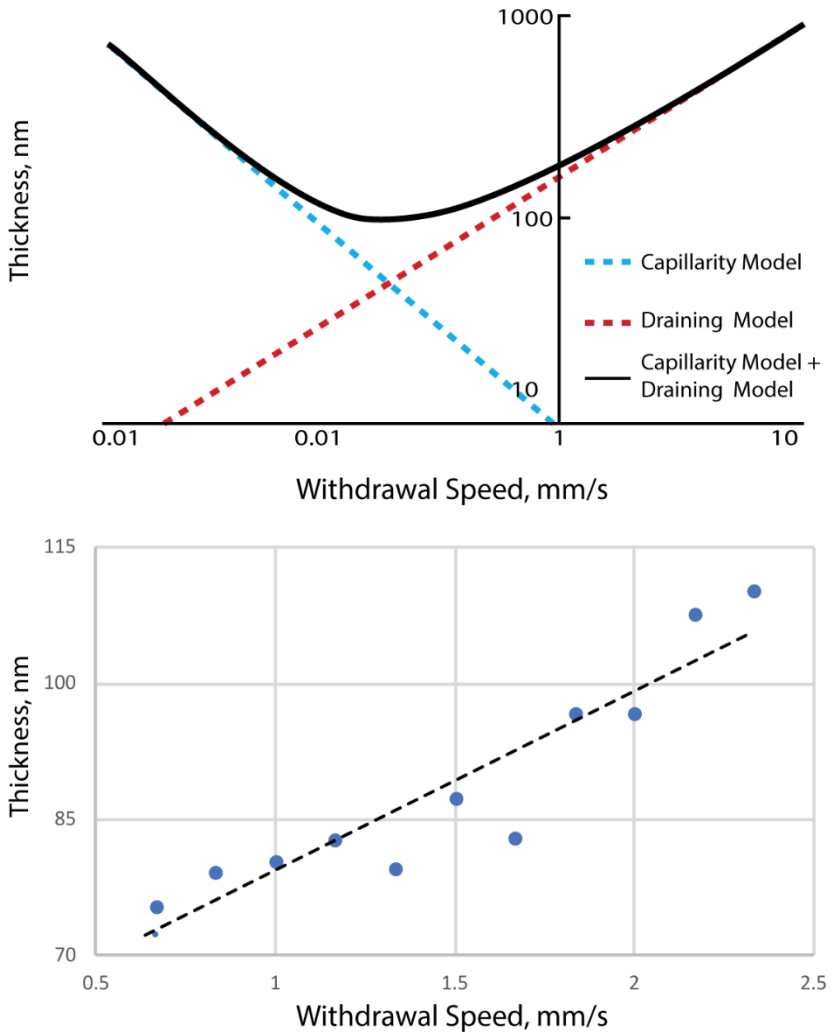

Figure 43. (A) The two models, based on capillary regime equation and the Landau-Levich equation respectively, generally applied into simulate the film thickness on dip coating process. (B) The relationship between the experimental thickness of silica film from sol 10 with withdrawal speed.

On the basis of the theoretical understanding, the refractive index, thickness (t), and the size (D) of the silica particle should have close relationships with their AR performance. Therefore, we prepared a series of silica coating with different thickness by controlling the withdrawal speed. T&RI&PS (thickness, refractive index, particle size)

mapping(Figure 44 a) built by spectroscopic ellipsometer analysis demonstrates the relationship among the thickness, particle size, refractive index of the silica coating. The dark red zone represents the coating with high refractive index (highest, 1.31) while the dark blue area is corresponding to the coating with a lower refractive index (lowest, 1.19). An interesting finding is that films assembled by small particles (10-20nm in diameter) have a high refractive index (~1.29-1.31), while films consisting of particles with diameter larger than 60nm tend to have a low refractive index (~1.19-1.25) which is increasing with the film thickness. This may be associated by the bottom layer particles tend to closer together in the thick film. Overall, the distribution of refractive index is a good response to our previous analysis and results about capillary dominated self-assembly of the silica particle.

6.2.3 The film with optimal AR properties at 550nm

According to Fresnel equation, to achieve theoretical 100% transmittance at 550 nm wavelength, the refractive index of the film is expected to be 1.23-1.25, and the thickness should be around 110nm considering the soda-lime glass substrate (RI=1.52). Here,

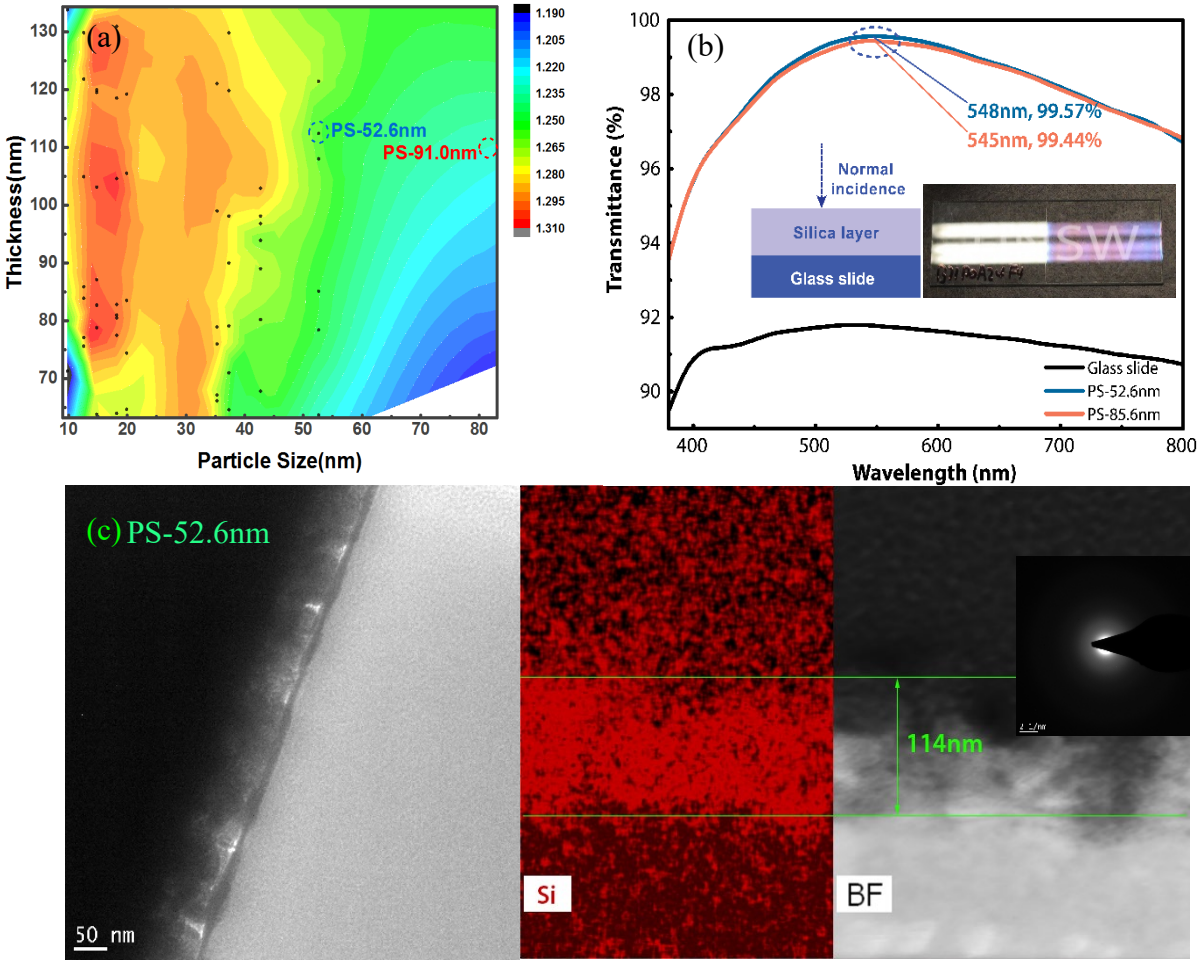

Figure 44. (a) Contours of weighted refractive index for a single-layer silica coating as a function of thickness and particle size. (b) The total transmittance spectra of glass slide, sample PS-52.6 and PS-91.0, inset is the image of sample PS52.6 (the right half side is with coating). (c) The TEM cross section image of sample PS-52.6, and corresponding silicon elemental mapping, inset is Electron diffraction pattern.

Samples PS-52.6 and PS-91.0, which meet the above condition, are extracted from T&RI&PS map(Figure 43a). Based on the EMA layer assisted simulation, we obtained

the fitting results of sample PS-52.6 and PS-91.0, the former silica layer has a thickness of 112nm and RI of 1.25, the silica layer thickness of the latter one is 110nm and corresponding RI is 1.23. Furthermore, the total transmittance spectra of these two samples are shown in Figure 44b, measured by spectroscopic ellipsometry with integrating sphere, and the inset image shows a sharp comparison of uncoated(left) and coated(right) area. The transmittance maxima of these two samples occurred at roughly the same wavelength (548nm for PS-52.6, 545nm for PS-91.0nm), which does respond well to the ellipsometry fitting results, indicating that the two-sample have very comparable silica coating thickness. The average transmittances over the visible wavelength range (380-800nm) are 98.18% and 98.11% for sample PS-52.6 and PS91.0 respectively, and the corresponding maximum transmittance is 99.57% and 99.44%. We expected that PS-91.0 would have a higher transmittance than PS-52.6 based on the fitting RI from ellipsometry. Instead, the results show that the latter has a higher transmittance. The reason probably is that the Mie scattering caused by the particle with a diameter larger than 100 nm decreases the transmittance to some degree[211]. Additionally, the instrument deviation of ±0.5% may also lead to the highest transmittance does not achieve 100%. The TEM image combined with silicon elemental map (Figure 45c) shows that the sample PS-52.6 has a thickness of 114nm, which matches perfectly with the fitting results of 112nm, from ellipsometry. The insert electron diffraction pattern confirmed the thin film is amorphous at current annealing temperature 550℃.

Transmittance haze measurement of these two coated glasses has been performed by UV-vis spectrometer, and the results were presented in Table 9. The transmittance haze can be derived by the following equation:

$$H = \left(\frac{T4}{T2} - \frac{T3}{T1}\right) \times 100\% \quad (11)$$

Where H is haze, T_{1-4} respectively represents the total intensity of incident light, total light transmitted through the glass sample, instrument diffusion, sample and instrument diffusion. Both sample PS-52.6 and PS-91 have low haze, 0.09%, and 0.26% separately. The former with relative lower haze value benefits from the small silica particle (52.6nm~550nm/10) which scattered light can be ignored in visible range referring to Rayleigh theory[212-214]. In another word, the latter comprising the larger particle (π91nm/550nm~0.52) results in relative stronger Mie scattering at a wider angle[215]. Nevertheless, the total transmittances of the two samples are roughly the same, 98.36% for PS-52.6 and 98.32 for PS-91. This can be explained that the ratio of forwarding scattered light to backward scattered light increases as the particle size increases and the forward scattered light became dominant[216].

Table 9. The Haze measurement results of sample PS-52.6 and PS-91.

Sample	T1	T2	T3	T4	H%
PS-52.6	100.09%	98.36%	0.32%	0.40%	0.09%
PS-91	100.09%	98.32%	0.32%	0.57%	0.26%

6.2.4 Annealing effect on the optical property

The optical property of Samples (PS-52.6nm) was investigated from two dimensions: different thickness arising from different dipping times and a series of withdrawing speed, and annealing temperatures (120, 550, 580 degrees in the air). The total transmittance spectra of these samples are summarized in Figure 45. Spectra of series of silica films annealed at 120 degrees in the air are shown in Figure 45a. The peak moves to more extended wavelength range as the increase of the withdrawal speed or twice dipping, and

this trend also coincides with the results on ellipsometry T&RI&PS map (Figure 44a) that higher withdrawal speed tends to deposit thicker silica film.

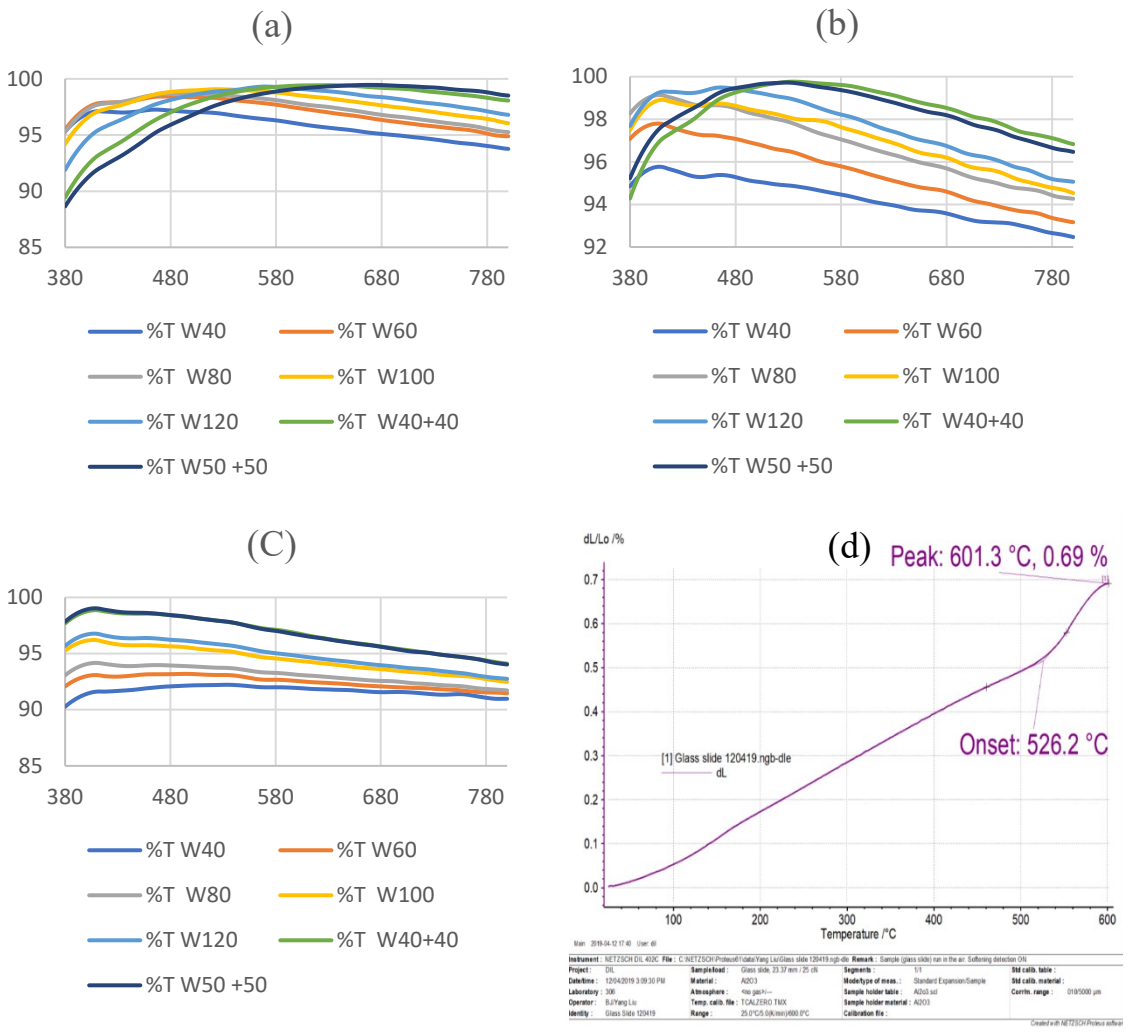

Figure 45 The transmittance spectra of sample PS-52.6 varying different thickness which controlled by the withdraw speed including 40-120mm/min, 40+40(twice coating with 40mm/min speed each time), 50+50(twice coating with 50mm/min speed each time). Images (a), (b), (c) corresponding three annealing temperature, 120, 550, 580 respectively. (d) Thermal Expansion Measurement of soda lime glass.

It is noticed that the highest transmittance is up to more than 99% with speed 100,120mm/min or dipping twice(40mm/min or 50mm/min each time), however, the films prepared with relative lower withdrawal speed(40, 60, 80mm/min) have a lower

transmittance peak(98.5%, 98%, 97%). Referring to the T&RI&PS mapping, it was focused on the particle size 52.6 nm zone, wherein the film thinner than 80 nm bears RI of 1.22 or lower. Therefore, it can be concluded that the thinner film derived from low withdrawal speed shows a relative lower transmittance peak in short-wavelength combining with the simulation results (Figure 37) which tell that the deviation from ideal RI of 1.23 leads to a lower left shifting of the transmittance spectra.

To estimate the impact of annealing temperature on the transmittance of the silica film, the spectra of the film was annealed at another two temperature, 550°C and 580°C. The three annealed temperatures were determined to avoid the unacceptable deformation of the glass substrate considering the softening point, 601.3°C of the soda-lime glass in Figure 45d. As can be seen in Figure 45bc, the spectra occur gradually blue shift at higher annealing temperature (550°C and 580°C) comparing the spectra in Figure 45a. For the thickest two films (40+40mm/min, 50+50mm/min), transmittance peaks can be stable above 99% with the movement to the shorter wavelength, from which it can be speculated that the silica films sustain highly porous structure but shrink in the direction perpendicular to the substrate. On the other side, the relatively thinner films (40-120mm/min) with highest transmittance peak shift to above 400nm wavelength at 550°C annealing temperature, and further decreased by 2-4% at 580°C. According to the movement of the spectra, it can be speculated that the dimension change occurs in the silica film with different annealing temperature and it is also applicable to control the antireflective performance in the selective wavelength range. However, the excessive temperature close to the glass substrate softening point will be counterproductive, which is inconsistent with the previous study[217].

To further confirm and analyze the shrinkage of silica film with increasing annealing temperature, SEM characterization of three samples which denoted as PS52.6T120,

PS52.6T550, PS52.6T580, corresponding with 120, 550, 580 ℃ annealing treatment, respectively were carried out. We can observe a large number of nanopores and crack on the silica film surface from Figure 46A-C, which represent for sample PS52.6T120, PS52.6T550, PS52.6T580, respectively. There is no significant change in the silica particle size, and the average thermal expansion coefficient of fused silica is $0.53*10^{-6}$ %•℃$^{-1}$ in the temperature range of 20-600 ℃[218]. In our case, the temperature effect on film thickness change coming from silica particle expansion can be ignored. Initially, we expected that the unavoidable crack on sample PS52.6T580 would be more severe than the sample treated at a lower temperature as the higher temperature may provide extra energy for the extension at the crack tip and lead to the spread of the crack [168]. However, it was noted that the distribution of the crack on three samples has no noticeable difference, even the crack growth is seemly more severe on sample PS52.6120(Figure 46A) compared with sample PS52.6T580 (Figure 46C). From the tilt (50 degrees) SEM images in Figure 46D, E, F, the interface between the film and glass substrate was clearly observed. The sample PS52.6T120 shows a two-layer of ordered silica particle spheres, the loose packing of the particle spheres introduced air and lower the refractive index, which is anticipated as the relatively low refractive index obtained from ellipsometry fitting results. The uneven bright patch and a little drifting of the image suffers from the low conductivity of the sample. With the annealing temperature increase to 550℃, the silica film in sample PS52.6T550 (Figure 46B) shows a relatively thinner layer which thickness is between one to two layer of close-packed silica particle sphere, and it gives

an acceptable explanation for the transmittance spectrum(Figure 45b) shifting to a lower wavelength range according to Fresnel theory. The transmittance peak values of sample PS52.6 are 99.44%, 628nm and 99.76%, 536nm at the annealing temperature of 120,

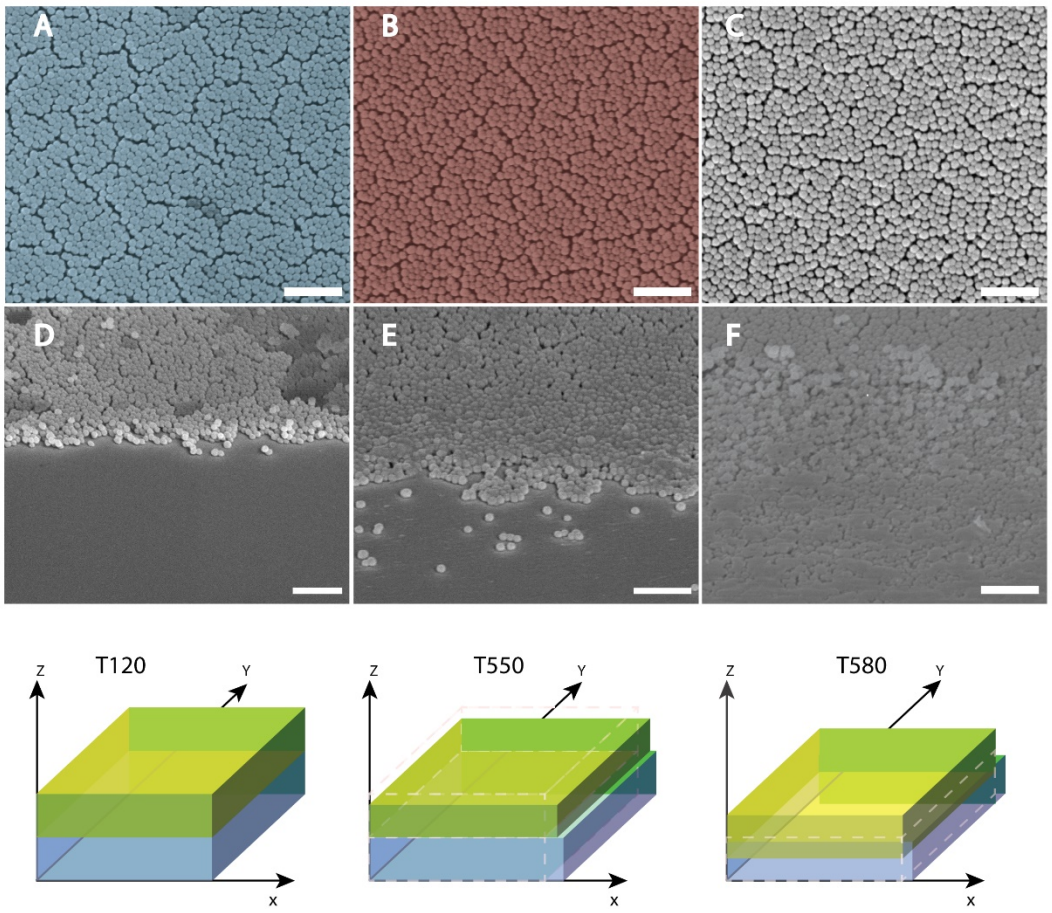

Figure 46. The SEM images of the sample PS52.6W40+40 at three annealing temperature, 120℃, 550℃, 580℃, which represented as PS52.6T120(A), PS52.6T550(B), PS52.6T580(C), respectively. Images(D-F) are the corresponding the tilt view (50°) Scale bars 500 nm. The bottom three illustrations give schematic models of the silica film (the green block) and glass substrate (the blue block) shrinkage with the increased annealing temperature. (Left to right are corresponding with temperature 120, 550, 580℃)

550℃ respectively. The max transmittance retained or became even higher after a higher temperature treatment. Therefore, the shrinkage at the temperature range of 120-550℃ mainly affects the film thickness rather than the porosity.

As we already excluded the effect from silica particle expansion, therefore, the reorientation of the silica particles is more likely to be the reason for thickness decrease. The schematic models of the silica film and glass substrate shrinkage was given by Figure 46. There are two blocks (the green one is silica film, the blue one for soda-lime glass substrate) in three-dimension rectangular coordinated. The glass substrate elongation in x-direction increased from 0.07% to 0.57% when the temperature rose continually from 120 to 550℃ (Figure 45d). The expansion of the substrate and loss of H_2O will induce the tensile stress in the x-y plane on the silica film. The heat and tensile stress may accelerate the reorientation of silica particle, and some of the particles tend to spread onto the glass surface and occupy a low energy status. In addition, with annealing temperature increase, the O-H and Si-OH will be decomposed and removed. Parrill et al. [219] found the stretch intensity of O-H and Si-OH decreases with the anneal temperature increased through Fourier transform infrared FIFR spectroscopy, and O-H content in silica film was indicated by the nonbridging Si-O stretch and the broad O-H stretch absorption between 3600-3200nm, the latter peak declined much in 500℃, and both two stretch peaks absent when temperature up to 900 and 1000 ℃. Therefore, the partial decomposition of O-H and Si-OH at 550℃ may sustain the refractive index. In Figure 46(F), it was observed that some part of the bottom silica particle diffused into the glass substrate, and the top surface was still deposited ordered silica particles. As a result, the effective antireflective silica layer thinner and refractive index increase, which gives a good explanation of the left downward shifting of transmittance(Figure 45C). Since it is expected that a film initially annealed at a higher temperature would be more resistant to higher temperatures, the films annealed at 550°C would be more practical to use. Nevertheless, to confirm the thickness and porosity change of the film, further ellipsometry analysis, and TEM cross-section observation are required.

6.3 Summary

The single-layer porous silica AR coating was successfully fabricated by the sol-gel combined dip-coating method. The porous structure derived low RI and $1/(4n)\lambda$ thickness leads to an excellent property in the visible range, with a maximum transmittance of 99.5% at 550nm wavelength and above 98% transmittance over the range of 380-800nm. It has been evaluated that the particle self-assembly behavior during dip coating was dominated by the capillary pressure based on the study of a range of silica particle size effect on the RI and nanostructure of the thin film prepared by dip-coating process. The RI of the silica layer can be tailored in the range of 1.19-1.31 by control over the particle size. Moreover, the annealing induced spectra shifting also provides a sensible strategy to achieve the right balance between the antireflective performance and mechanic performance. Future work focuses on the improvement of coating compatibility and durability for practical use, which involves long term wearability, high-performance scratch resistance, etc.

Chapter 7 Low-cost antireflection coating systems with wide-angle light-harvesting: Application on photovoltaic module

The antireflection coating has become an essential process on the solar cell application. In general, the top layer of solar cells will be a cover glass, which protects the solar cell from dust, space radiation, and other environmental aggressors. The topography of the cover glass in our research is shown in Figure 47. The reflection in the glass-air interface is up to 4% in practical, and depositing an antireflective layer on the cover glass can

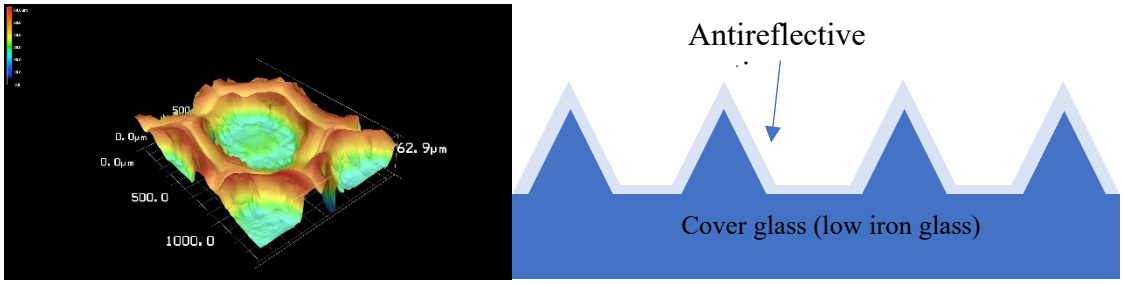

Figure 47. The topography of patterned glass and geometry of antireflective coating on the glass.

suppress the reflection and improve the overall power efficiency of the solar cell. However, the sunlight hits the surface of silicon cell from various angels during a day, and above 40% light will be reflected on a polished silicon surface when considering all angles of incidence(AOI) and the solar radiation spectrum [220]. Herein, single layer silica-based antireflection coating combined with patterned glass (low iron glass) was fabricated by a simple dip-coating process. Moreover, precise controlling the transmittance spectrum of the AR coated cover glass is essential to exact match with the solar cell response spectrum (External quantum efficiency curve, EQE), further realizing the maximize the output efficiency.

7.1 Experimental Procedures

Preparation of AR coating on the low iron patterned glass.

The silica-based antireflection coating on low iron glass was prepared using the sol-gel combined dip-coating method. The silica sol 10 was used as a dip coating source. After the coating process, the cover glass was annealed at 550-degree centigrade for 3 hours.

Optical properties.

Total transmittance and specular reflection at different AOI of the coatings were measured by Perkin Elmer Lambda 950 UV–vis spectrometer using an integrating sphere.

Freezing Test.

The samples were exposed to freezing temperatures, at −40 °C for 24 h. The total transmittance of the film was measured before and after the test to determine if freezing degrades or delaminates the coatings.

Environmental Exposure Tests.

The environmental exposure tests were performed at 60 °C and relative humidity of 80% for 120h referring to the previous work[217] at the environmental chamber (CAT 5200HS with a ramping rate of 2.00 °C min−1). The total transmittance measurement was carried out before and after the test by use of the Perkin Elmer 950.

Hot water fogging test.

The fogging test was accomplished by placing two glasses (coated and uncoated) on the top of a beaker filled with a certain amount of water at 90 degrees for 10 mins. Then, we compare the water condensation on the downsides of two glasses.

7.2 Results and Discussion

7.2.1 Silica AR coating combined with patterned glass

Different wavelength of sunlight has a different energy, and also the different number of photons. In the solar silicon cell, the conversion between photon energy and electricity at different wavelength can be reflected in the corresponding spectral response (EQE). In

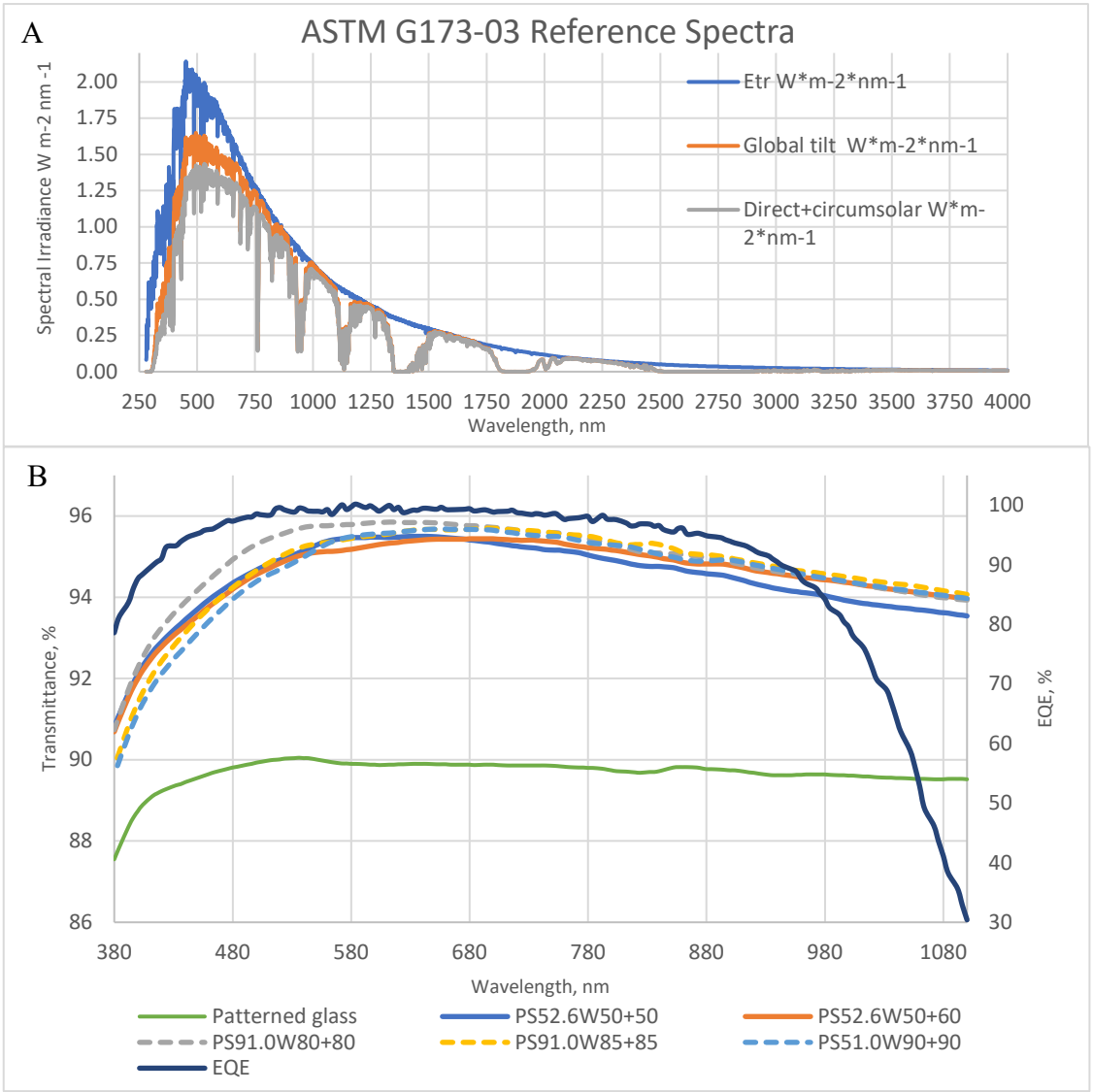

Figure 48. (A) reference solar spectral irradiance (ASTM G-173) [3] and the ideal transmission for solar thermal application. (B) The transmittance spectra of blank patterned glass, different coated glass samples and EQE curve for the solar cell module.

general, the range of spectral response is 380-1100nm, and the peak of response is 800-

900nm. Nevertheless, the solar radiation on the earth is referring to the AM1.5 solar radiation spectrum (see Figure 48A) in which the peak is above 500nm. Therefore, to optimize the output efficiency of silicon solar cell with optical coating, the AM1.5 solar radiation spectrum and silicon solar cell external quantum efficiency spectrum must be comprehensively considered.

Here, the solar cell photovoltaic module EQE spectrum was presented in Figure 48 B, which is measured from 380 nm as the power from the AM1.5 contained in lower wavelengths is low. The theoretical module output power can be calculated by equation (12), which combines AM1.5. solar radiation spectrum, solar cell EQE, and total transmittance. The total transmittance here equals absorption based on the assumption that whatever transmitted through the glass will be absorbed by the solar cell.

$$P = \int_{380nm}^{1100nm} S(\lambda) \cdot T(\lambda) \cdot \mathrm{EQE}(\lambda) \cdot \mathrm{d}\lambda \qquad (12)$$

Where S(λ) is solar radiation (AM 1.5), T(λ) is total transmittance.

The transmittance spectra of sample PS52.6(solid line) and PS91.0(Dash line) can be seen in Figure 48 B. The EQE retain a high value up to more than 99% in the range of 516-700nm. Moreover, the solar radiation in that range is also stronger compared with the rest wavelength range. Three PS91.0 samples maintain comparative advantage in transmittance in the whole range while two PS52.6 samples are bearing a relative lower transmittance. It is anticipated that the sample PS.0 provides the solar cell superior performance, which has been confirmed in Table 10, wherein the theoretical power has been calculated from the equation (12). The sample PS91.0W80+80 was expected to contribute the highest power 137.61 w*m^{-2}, 0.4% above the PS52.6W50+60, and 2.5% higher than the patterned glass without coating.

Figure 49 (a) shows the typical SEM image of moth-eye, and the antireflective performance is achieved by the subwavelength nipple array, which introduced a graded refractive index between the eye and air and the light tends to bend through progressively the eye[4]. The SEM images of PS91.0W80+80 coated patterned glass was presented in the Figure 49(c-d), from which we can observe an even layer across the silica particle on the glass surface. The tilted view reveals a silica particle array which is similar to the moth-eye structure (Figure 49a). Thus, the lower refractive index of the interface between the glass (RI=1.52) and air (RI=1) benefited from the nanoarray, wherein loose arranged silica particles were mixed with air.

Table 10. The average transmittance in the range of 380-1100nm and theoretical power calculated from equation (1).

Sample	Transmittance %	Theoretical Power W*m-2
Bare Patterned glass	89.68	129.86
PS52.6W50+50	94.48	137.02
PS52.6w50+60	94.59	137.06
PS91.0w80+80	94.88	137.61
PS91.0w85+85	94.72	137.26
PS91.0w90+90	94.59	137.07

Above transmittance measurements were all performed with normal incident light. In practical solar cell application, it must be considered the changing angle of incident sunlight during a day. Therefore, the total (specular and diffusive) reflection and specular

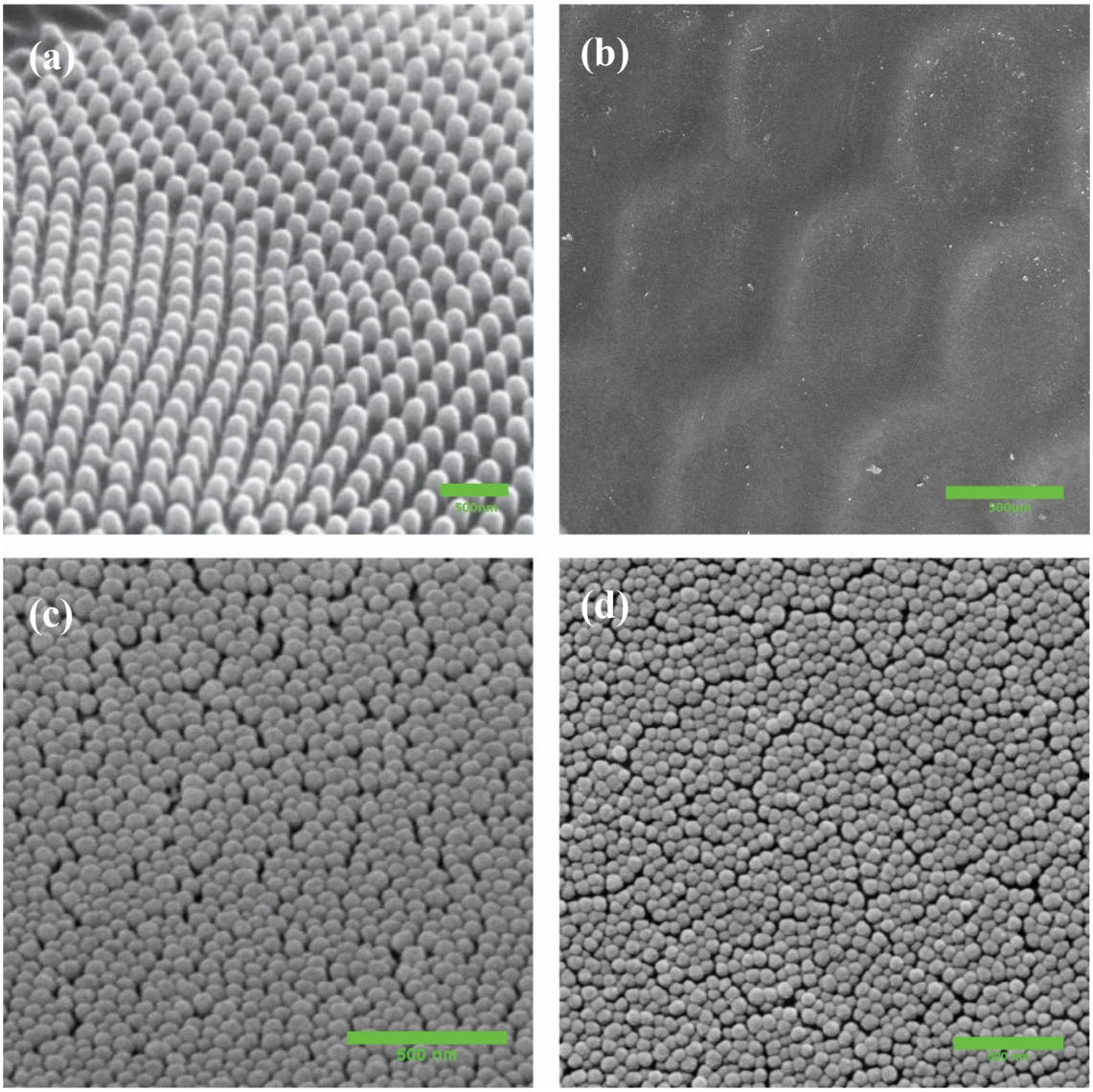

Figure 49. (a) SEM image showing the nipple array on moth's eye[1]. (b) The SEM image of coated patterned glass PS91.0W80+80. (c-d) The magnified SEM image of silica nanoarray on the Coated patterned glass PS91.0W80+80, tilted and top view respectively. Scale Bars, a, 500nm; b, 500μm; c, 500nm; d, 500nm.

reflection at three different AOI were obtained by Integrating Sphere and Universal Reflectance Accessories in PerkinElmer 950 UV-vis spectrometer. The summarized results and spectra can be seen in Figure 50and Figure 51(a-d), respectively. We observe

that the total reflectance of plane glass and patterned glass are almost the same while the specular reflectance difference is widening with the increase of AOI. The patterned glass can achieve lower reflection combining with a single layer of silica, more specifically, the total average reflection of PS91.0W80+80 on patterned glass is about 2.6%, and

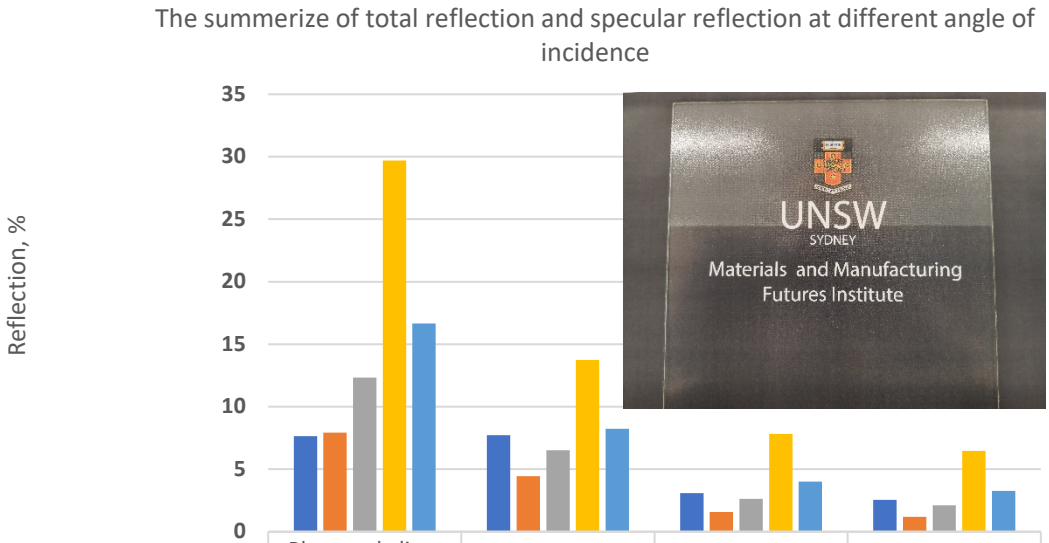

	Plane soda lime glass	Patterned glass	PS52.6W50+50	PS91.0W80+80
Total reflection	7.6394	7.732596685	3.07441989	2.554088398
8°	7.916354	4.444640884	1.570276243	1.195911602
45°	12.33099	6.52160221	2.629558011	2.113480663
68°	29.70972	13.75309392	7.822983425	6.476629834
Average specular reflection	16.65235467	8.239779006	4.007605893	3.262007366

Figure 50. The summarize of total reflection and specular reflection for plane soda-lime glass, blank patterned glass, coated patterned glasses (PS91.0W80+80 and PS56.2W50+50). Inset, the image of half part coated patterned glass with 210*210mm size (bottom side is coated area).

PS56.2W50+50 on patterned glass has a relatively high reflection which is 3.1%. This result indicates that the film built by 91.0nm particle performs better than a particle with a diameter of 52.6nm on patterned glass, which differs from that on the plane glass. The average specular reflection over the three AOI of coated patterned glass (PS91.0W80+80)

is 3.26%. Compared to 16.65% of uncoated plane glass, a decrease of 80% is visually evident from the inset in Figure 50.

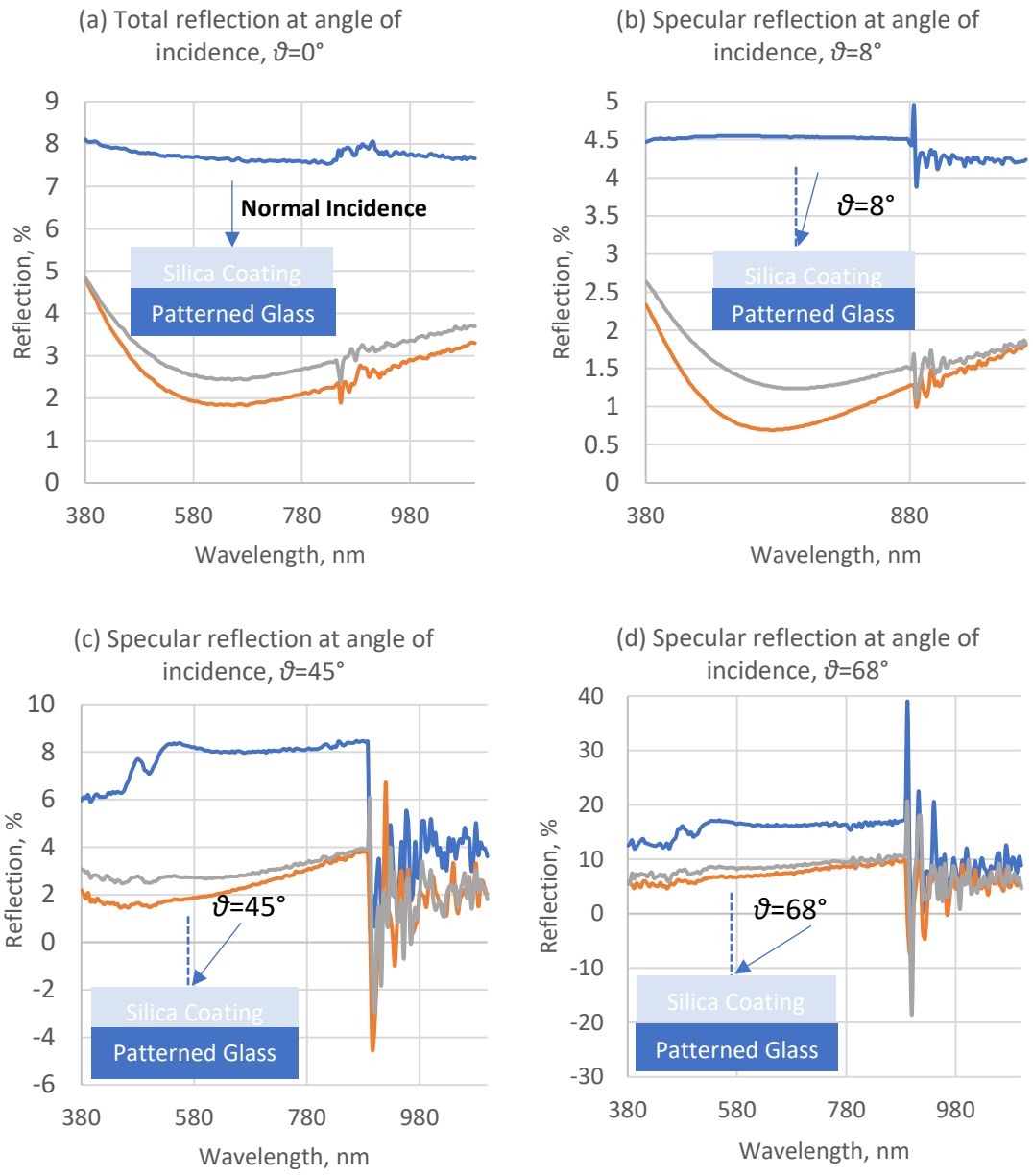

Figure 51. Measured reflection for blank patterned glass(blue line) and two coated glasses(Orange line for PS91.0W80+80, grey line corresponding to PS52.6W50+50) at various incidence angles, (a) total reflection at normal incidence, (b) specular reflection at angle of incidence of 8°, (c) specular reflection at angle of incidence of 45°, (d) specular reflection at angle of incidence of 68°.

7.2.2 Durability assessment

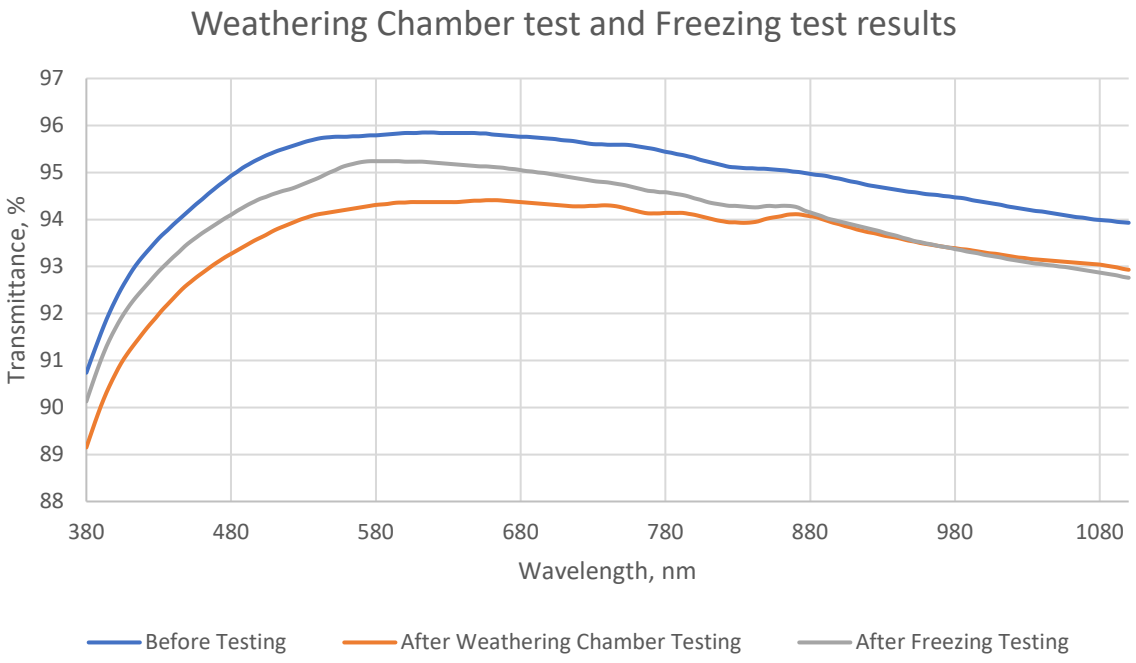

	Before Testing	After Weathering Chamber Testing	After Freezing Testing
Average Transmittance, %	94.8781768	93.57674033	94.03812155
ΔT, %	-	-1.40%	-0.88%

Figure 52. Chart presents the total transmittance spectra of sample PS90.0w80+80 before and after weathering Chamber test and Freezing testing. Table shows the average transmittance and transmittance changes before and after testing.

The sol-gel derived silica thin film easily absorb water molecular because there is a large number of hydroxyl groups left on the silica film surface. In our case, the silica coating glass was annealed at 550 ℃for three hours. Therefore, the water molecular is even more likely to be attached on the silica surface because the H_2O and OH- concentrations are more sensitive to the film after annealing evidenced by T. M. Parrill [219]. In addition, the capillary force induced moisture penetration may lead to porous structure collapse

because of the water surface tension. Thus, the transmittance will be affected. Therefore, the weathering chamber testing is crucial aspects for the evaluation of the AR coating in

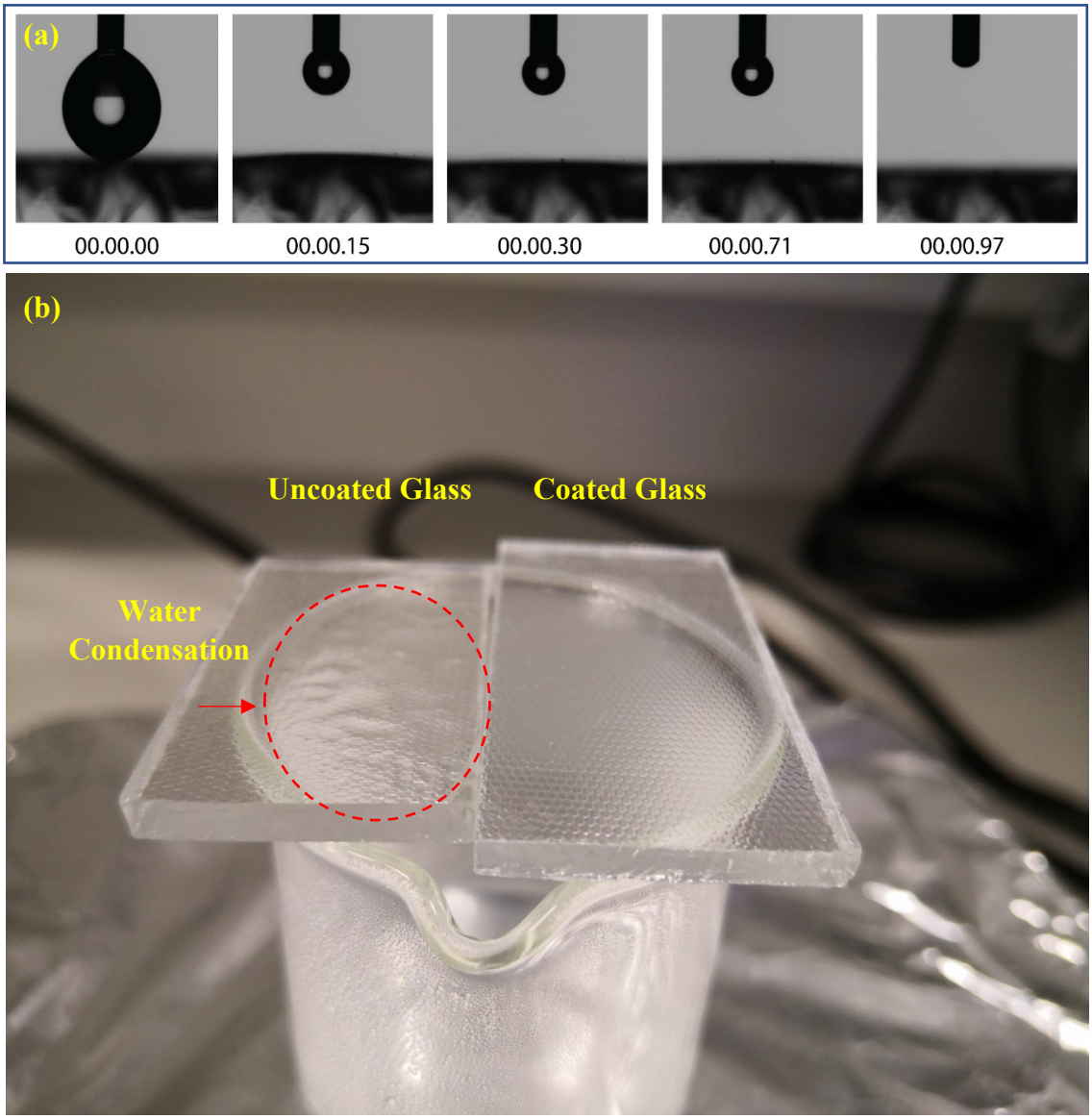

Figure 53. (a) Time-dependent changes in water contact angle, unit for s. (b) The antifogging test of uncoated glass and coated glass.

practical application. As Figure 52 shows, the total transmittance of the sample after the weathering chamber test shift down, and the average transmittance over the range of 380-1100nm decreases by 1.4% from 94.88% to 93.58%. Moreover, the sample experienced freeze testing at minus 43 ℃ for 24hrs shows better results (see Figure 52), 0.88% drop in average transmittance, which may suffer from the small cracks throughout the film.

These results show that the silica AR coating has good resistance to subzero temperatures, whereas the moisture-induced effect in transmittance cannot be ignored.

The surface property of the coated glass was characterized by Water Contact Angles (WCAs). The dynamic changing of WCAs was recorded as Figure 53a. The water drops (2μL) spread over the surface in a second. WCAs decrease to 5° within 0.15s, and nearly declines to 0° after 0.97s, which reflects the super hydrophilicity of the surface. The instantaneous spreading renders the glass with excellent anti-fogging performance. As the hot water fogging test (Figure 53b) shows, there appears heavy water condensation on the down surface of the uncoated glass, and these droplets will cause light scattering. However, the coated glass remains clear.

7.3 Summary

In conclusion, the work in this chapter realized the beneficial combination of silica nanoparticle array as AR coating and patterning on the solar cell cover glass. The coated sample PS91.0W80+80 was expected to contribute 2.5% increment of output power efficiency, referring to the patterned glass without coating. The average specular reflectance across a wide angle of incidence (0-68°) lower to about 3.3% compared with the 16.6% of plane glass. The AR coating demonstrated good stability through accelerated environmental test and freeze test. Besides, super hydrophilicity of the coating makes it have the characteristics of antifogging. Therefore, the combination of silica antireflective coating and patterned glass is a promising way of developing low-cost, high-efficient, and omnidirectional solar applications in the future.

Chapter 8 Conclusions and Future work

8.1 Conclusions

We prepared a batch of uniform and stable silica sol via a base-catalyzed sol-gel method, and results establish that the silica nanoparticle with narrow size distributions is tunable from 9.8 to 91.0nm in diameter under precisely controlled molar ratio n_{NH4+}/n_{TEOS}. Furthermore, the initial pH value, adjusted by the mole ratio n_{NH4+}/n_{TEOS}, played a critical role in stabilizing the dispersion of the nano-silica particle in the sol. The mole ratio n_{NH4+}/n_{TEOS} 0.33-0.98 proved to be the acceptable range that can obtain a stable sol system, sustaining for longer than 60 days considering the aging effect on the particle aggregation.

A single layer silica AR coating, the sample PS91.0W80+80 with void percentage 52% (simulation results based on Bruggeman Effective Medium Approximations) or 50% (calculation based on BJH pore volume), had the best transmittance 99.5% at 550nm and above 98% transmittance over the range 380-800nm, using sol-gel combined dip-coating process. The refractive index of the coating can be adjusted from 1.19-1.31 by control of the particle size. It was also discussed that, in the Ethanol solution system, the capillary pressure determines the assembly of silica nanoparticle when dip coating process is ongoing. As a result, the smaller silica particles were likely to pack closer and lead to a higher refractive index, and the effect was reversed for the larger particle. Additionally, it was observed that the annealing temperature affected the spectrum shifting, and the temperature should be able to control below the soft point of substrate glass to avoid the shrink or deformation derived AR performance degradation.

A scientific combination of the patterning on the cover glass and silica nanoarray coating (plays role as AR coating) with synthetically considering the solar radiation spectrum,

solar cell response spectrum and the transmittance spectrum of coated glass, realized a wide-angle (3.3% average specular reflection at Angle of incidence, 0-68°) light-harvesting PV system which is expected to get a higher output efficiency. The theoretic calculation gives that Sample PS91.0W80+80 coated patterned glass is estimated to contribute 2.5% power increment to the PV system comparing to the system with uncoated patterned glass. Therefore, the tolerability and optimization of the silica AR coating lend itself to the cooperation into the PV module device for application-specific requirements.

8.2 Future work

Through the analysis of the experimental results and conclusion, there are some insufficiencies that need to be pointed out. In the meantime, we consider that there remains room for AR technology based on the sol-gel process to further development:

1. To confirm our observation and qualitatively study the catalyst effect on the formation of silica sol and the conversion from suspension to sol or gel, further spectroscopic investigation (NMR, FTIR) needs to be carried out.
2. The inadequacy of chapter 7 is the lack of quantitative analysis of the capillary pressure, which plays a dominant role in the assembly of the particle during dip coating.
3. The evaluation of the solar cell performance enhancement demands a more precise characterization of quantum efficiency and current-voltage of the solar cell module with a coated and uncoated cover glass.
4. To stably produce a high-quality anti-reflection coating on a large area through the dip-coating process, there are still many practical problems to be solved, which

involves the gravity-induced thickness inhomogeneity, the mechanical stresses derived crack.

5. Further improve the coating compatibility and durability, which involves long term wearability, high-performance scratch resistance, etc.
6. Explore how to effectively control the pore distribution and obtain a silica layer with a graded refractive index. The sol-gel process, combined with electrophoretic deposition method, has the potential to realize accurate control of the thickness while achieving the graded pore distribution.

Reference

1. Valliant, E.M. and J.R. Jones, *Softening bioactive glass for bone regeneration: sol–gel hybrid materials.* Soft Matter, 2011. **7**(11): p. 5083-5095.
2. Rayleigh, L., *On reflection of vibrations at the confines of two media between which the transition is gradual.* Proceedings of the London Mathematical Society, 1879. **1**(1): p. 51-56.
3. Macleod, H.A., *Thin-Film Optical Filters*, ed. R.G.W.B. E. Roy Pike. 2001.
4. Clapham, P. and M. Hutley, *Reduction of lens reflexion by the "Moth Eye" principle.* Nature, 1973. **244**(5414): p. 281-282.
5. Choi, K., et al., *Nano‐tailoring the surface structure for the monolithic high‐performance antireflection polymer film.* Advanced Materials, 2010. **22**(33): p. 3713-3718.
6. Yoldas, B.E., *Investigations of porous oxides as an antireflective coating for glass surfaces.* APPLIED OPTICS, 1980.
7. Yao, Y., et al., *Porous Nanomaterials for Ultrabroadband Omnidirectional Anti‐Reflection Surfaces with Applications in High Concentration Photovoltaics.* Advanced Energy Materials, 2017. **7**(7).
8. Li, X., et al., *Porous Polymer Films with Gradient‐Refractive‐Index Structure for Broadband and Omnidirectional Antireflection Coatings.* Advanced Functional Materials, 2010. **20**(2): p. 259-265.
9. Raut, H.K., et al., *Anti-reflective coatings: A critical, in-depth review.* Energy & Environmental Science, 2011. **4**(10).
10. Taylor, H.D., *A method of increasing the brilliancy of the images formed by lenses.* British patent, 1904. **29561**.
11. Rubio, F., et al., *Sputtered Ta2O5 antireflection coatings for silicon solar cells.* Thin Solid Films, 1982. **90**(4): p. 405-408.
12. Henning Nagel*, A.G.A.a.R.H., *Optimised Antire¯ection Coatings for Planar Silicon Solar Cells using Remote PECVD Silicon Nitride and Porous Silicon Dioxide.* PROGRESS IN PHOTOVOLTAICS: RESEARCH AND APPLICATIONS, 1999.
13. Xi, J.-Q., et al., *Optical thin-film materials with low refractive index for broadband elimination of Fresnel reflection.* Nature Photonics, 2007. **2**(2): p. 76-76.
14. Pargellis, A., *Evaporating and sputtering: Substrate heating dependence on deposition rate.* Journal of Vacuum Science & Technology A: Vacuum, Surfaces, and Films, 1989. **7**(1): p. 27-30.
15. *10mm Sq., 2mm Thick, MgF2 Coated λ/4 N-BK7 Window | Edmund Optics.* . 2019.
16. Li, X., et al., *Increased laser-damage resistance of sol–gel silica coating by structure modification.* The Journal of Physical Chemistry C, 2012. **116**(34): p. 18367-18371.
17. Li, W., et al., *Ordered Mesoporous Materials Based on Interfacial Assembly and Engineering.* Advanced Materials, 2013. **25**(37): p. 5129-5152.
18. Zou, L., et al., *An abrasion-resistant and broadband antireflective silica coating by block copolymer assisted sol–gel method.* Langmuir, 2014. **30**(34): p. 10481-10486.
19. Li, Y.Y., et al., *Preparation of porous silica films in a binary template system for double-layer broadband antireflective coatings.* RSC Advances, 2015.

20. Xiao, B., et al., *Sol–gel preparation of double-layer tri-wavelength antireflective coating.* Journal of Sol-Gel Science and Technology, 2012. **64**(2): p. 276-281.
21. Sun, J., et al., *A broadband antireflective coating based on a double-layer system containing mesoporous silica and nanoporous silica.* 2015.
22. Tao, C., et al., *Detailed analysis and formation mechanism of superhydrophobic antireflective coatings with adjustable refractive index from trimethylsilanized silica nanoparticles.* Journal of Sol-Gel Science and Technology, 2016. **80**(1): p. 10-18.
23. Brinker, C.J., et al., *Evaporation‐induced self‐assembly: nanostructures made easy.* Advanced materials, 1999. **11**(7): p. 579-585.
24. Grosso, D., et al., *An in situ study of mesostructured CTAB− silica film formation during dip coating using time-resolved SAXS and interferometry measurements.* Chemistry of Materials, 2002. **14**(2): p. 931-939.
25. Cagnol, F., et al., *Humidity-controlled mesostructuration in CTAB-templated silica thin film processing. The existence of a modulable steady state.* Journal of Materials Chemistry, 2003. **13**(1): p. 61-66.
26. Bindini, E., et al., *Critical role of the atmosphere in dip-coating process.* The Journal of Physical Chemistry C, 2017. **121**(27): p. 14572-14580.
27. Brinker, C., et al., *Fundamentals of sol-gel dip coating.* Thin solid films, 1991. **201**(1): p. 97-108.
28. Grosso, D., C. Boissière, and C. Sanchez, *Ultralow-dielectric-constant optical thin films built from magnesium oxyfluoride vesicle-like hollow nanoparticles.* Nature materials, 2007. **6**(8): p. 572-575.
29. Bao, L., et al., *Design and preparation of broadband antireflective coatings with excellent mechanical properties.* Materials Letters, 2016. **185**: p. 464-467.
30. Bernhard, C., *Structural and functional adaptation in a visual system.* Endeavour, 1967. **26**: p. 79-84.
31. Huang, Y.-F., et al., *Improved broadband and quasi-omnidirectional anti-reflection properties with biomimetic silicon nanostructures.* Nature nanotechnology, 2007. **2**(12): p. 770-774.
32. Walheim, S., et al., *Nanophase-separated polymer films as high-performance antireflection coatings.* Science, 1999. **283**(5401): p. 520-522.
33. Ibn-Elhaj, M. and M. Schadt, *Optical polymer thin films with isotropic and anisotropic nano-corrugated surface topologies.* Nature, 2001. **410**(6830): p. 796-799.
34. Hiller, J., J.D. Mendelsohn, and M.F. Rubner, *Reversibly erasable nanoporous anti-reflection coatings from polyelectrolyte multilayers.* Nat Mater, 2002. **1**(1): p. 59-63.
35. Krogman, K.C., T. Druffel, and M.K. Sunkara, *Anti-reflective optical coatings incorporating nanoparticles.* Nanotechnology, 2005. **16**(7): p. S338-43.
36. Druffel, T., K. Geng, and E. Grulke, *Mechanical comparison of a polymer nanocomposite to a ceramic thin-film anti-reflective filter.* Nanotechnology, 2006. **17**(14): p. 3584.
37. Wu, Z., et al., *Deformable antireflection coatings from polymer and nanoparticle multilayers.* Advanced Materials, 2006. **18**(20): p. 2699-2702.
38. Ting, C.-J., et al., *Low cost fabrication of the large-area anti-reflection films from polymer by nanoimprint/hot-embossing technology.* Nanotechnology, 2008. **19**(20): p. 205301.
39. Xue, L., J. Zhang, and Y. Han, *Phase separation induced ordered patterns in thin polymer blend films.* Progress in Polymer Science, 2012. **37**(4): p. 564-594.

40. Li, X., X. Yu, and Y. Han, *Polymer thin films for antireflection coatings.* Journal of Materials Chemistry C, 2013. **1**(12): p. 2266-2285.
41. Raut, H.K., et al., *Robust and durable polyhedral oligomeric silsesquioxane-based anti-reflective nanostructures with broadband quasi-omnidirectional properties.* Energy & Environmental Science, 2013. **6**(6).
42. Schulz, U., et al., *Breakthroughs in Photonics 2013: Organic Nanostructures for Antireflection.* IEEE Photonics Journal, 2014. **6**(2): p. 1-5.
43. Lim, J.H., J.W. Leem, and J.S. Yu, *Solar power generation enhancement of dye-sensitized solar cells using hydrophobic and antireflective polymers with nanoholes.* RSC Advances, 2015. **5**(75): p. 61284-61289.
44. Gan, X., et al., *Polymer-coated graphene films as anti-reflective transparent electrodes for Schottky junction solar cells.* J. Mater. Chem. A, 2016. **4**(36): p. 13795-13802.
45. Chuang, C.-H., et al., *Antireflective polymer films via roll to roll UV nanoimprint lithography using an AAO mold.* Microsystem Technologies, 2017.
46. Peng, Y.-J., H.-X. Huang, and H. Xie, *Rapid fabrication of antireflective pyramid structure on polystyrene film used as protective layer of solar cell.* Solar Energy Materials and Solar Cells, 2017. **171**: p. 98-105.
47. So, S., et al., *Fabrication of PEDOT Nanocone Arrays with Electrochemically Modulated Broadband Antireflective Properties.* J Phys Chem Lett, 2017. **8**(3): p. 576-579.
48. Schulz, U., et al., *Gradient index antireflection coatings on glass containing plasma-etched organic layers.* Optical Materials Express, 2015. **5**(6): p. 1259-1265.
49. J. Fraunhofer, in Gesammelte Schriften, edited by F. Hommel (Munich, 1887).
50. GoCHO, T., *Chemical Vapor Deposition of Anti-Reflective Layer Film for Excimer Laser Lithography.* Japanese Journal of Applied Physics, 1994.
51. Chen, J., et al., *Facile fabrication of antifogging, antireflective, and self-cleaning transparent silica thin coatings.* Colloids and Surfaces A: Physicochemical and Engineering Aspects, 2016. **509**: p. 149-157.
52. Choi, M.-J., et al., *Enhanced Anti-reflective Effect of SiNx/SiOx/InSnO Multi-layers using Plasma Enhanced Chemical Vapor Deposition System with Hybrid Plasma Source.* Applied Science and Convergence Technology, 2016. **25**(4): p. 73-76.
53. Xi, J.-Q., et al., *Very low-refractive-index optical thin films consisting of an array of SiO 2 nanorods.* Optics letters, 2006. **31**(5): p. 601-603.
54. Chhajed, S., et al., *Nanostructured multilayer graded-index antireflection coating for Si solar cells with broadband and omnidirectional characteristics.* Applied Physics Letters, 2008. **93**(25): p. 251108.
55. Kim, J.K., et al., *Light‐extraction enhancement of GaInN light‐emitting diodes by graded‐refractive‐index indium tin oxide anti‐reflection contact.* Advanced materials, 2008. **20**(4): p. 801-804.
56. Yeo, C.I., et al., *A single-material graded refractive index layer for improving the efficiency of III–V triple-junction solar cells.* Journal of Materials Chemistry A, 2015. **3**(14): p. 7235-7240.
57. Rehmer, A., K. Scheurell, and E. Kemnitz, *Formation of nanoscopic CaF 2 via a fluorolytic sol–gel process for antireflective coatings.* Journal of Materials Chemistry C, 2015. **3**(8): p. 1716-1723.
58. Huang, Q.Z., et al., *Study on sodium water glass-based anti-reflective film and its application in dye-sensitized solar cells.* Thin Solid Films, 2016. **610**: p. 19-25.

59. Karthik, D., et al., *High performance broad band antireflective coatings using a facile synthesis of ink-bottle mesoporous MgF 2 nanoparticles for solar applications.* Solar Energy Materials and Solar Cells, 2017. **159**: p. 204-211.
60. Liu, Z., et al., *Sol–gel SiO 2/TiO 2 bilayer films with self-cleaning and antireflection properties.* Solar Energy Materials and Solar Cells, 2008. **92**(11): p. 1434-1438.
61. Yao, L. and J. He, *Recent progress in antireflection and self-cleaning technology–From surface engineering to functional surfaces.* Progress in Materials Science, 2014. **61**: p. 94-143.
62. Jannat, A., et al., *Low cost sol–gel derived SiC–SiO 2 nanocomposite as anti reflection layer for enhanced performance of crystalline silicon solar cells.* Applied Surface Science, 2016. **369**: p. 545-551.
63. Hovel, H., *TiO2 antireflection coatings by a low temperature spray process.* Journal of the Electrochemical Society, 1978. **125**(6): p. 983-985.
64. Uzum, A., et al., *Sprayed and Spin-Coated Multilayer Antireflection Coating Films for Nonvacuum Processed Crystalline Silicon Solar Cells.* International Journal of Photoenergy, 2017. **2017**.
65. Liu, L.Q., et al., *Broadband and omnidirectional, nearly zero reflective photovoltaic glass.* Advanced Materials, 2012. **24**(47): p. 6318-6322.
66. Jang, S.J., et al., *Structural and optical properties of silicon by tilted angle evaporation.* Surface and Coatings Technology, 2010. **205**: p. S447-S450.
67. R. C. Jayasinghe, A.G.U.P., *Optical properties of nanostructured TiO2 thin films and their application as antireflection coatings on infrared detectors.* OPTICS LETTERS, 2012. **37**.
68. Xinxiang Zhang, H.Y., *Sol-Gel Preparation of PDMS/Silica Hybrid Antireflective Coatings with Controlled Thickness and Durable Antireflective Performance.* J. Phys. Chem. C, 2010.
69. Wang, X. and J. Shen, *A review of contamination-resistant antireflective sol–gel coatings.* Journal of sol-gel science and technology, 2012. **61**(1): p. 206-212.
70. X Wang, J.S., *A review of contamination-resistant antireflective sol–gel coatings.* Journal of sol-gel science and technology, 2012. **45**(7): p. 1608-1618.
71. Nguyen, C.V., et al., *Low-dielectric, nanoporous organosilicate films prepared via inorganic/organic polymer hybrid templates.* Chemistry of materials, 1999. **11**(11): p. 3080-3085.
72. Kim, H.C., et al., *Fabrication of multilayered nanoporous poly (methyl silsesquioxane).* Advanced Materials, 2002. **14**(22): p. 1637-1639.
73. Yang, S., et al., *Nanoporous ultralow dielectric constant organosilicates templated by triblock copolymers.* Chemistry of materials, 2002. **14**(1): p. 369-374.
74. Lee, B., et al., *Ultralow-k nanoporous organosilicate dielectric films imprinted with dendritic spheres.* Nature materials, 2005. **4**(2): p. 147-150.
75. Kim, S., J. Cho, and K. Char, *Thermally stable antireflective coatings based on nanoporous organosilicate thin films.* Langmuir, 2007. **23**(12): p. 6737-6743.
76. Lalanne, P. and G.M. Morris. *Design, fabrication and characterization of subwavelength periodic structures for semiconductor anti-reflection coating in the visible domain*. in *Proc. SPIE*. 1996.
77. Lalanne, P. and G.M. Morris, *Antireflection behavior of silicon subwavelength periodic structures for visible light.* Nanotechnology, 1997. **8**(2): p. 53.
78. Kanamori, Y., M. Sasaki, and K. Hane, *Broadband antireflection gratings fabricated upon silicon substrates.* Optics letters, 1999. **24**(20): p. 1422-1424.

79. Min, W.L., B. Jiang, and P. Jiang, *Bioinspired Self‐Cleaning Antireflection Coatings.* Advanced Materials, 2008. **20**(20): p. 3914-3918.
80. Li, Y., et al., *Bioinspired silicon hollow-tip arrays for high performance broadband anti-reflective and water-repellent coatings.* Journal of Materials Chemistry, 2009. **19**(13).
81. Kanamori, Y., et al., *Subwavelength antireflection gratings for GaSb in visible and near-infrared wavelengths.* Japanese journal of applied physics, 2003. **42**(6S): p. 4020.
82. Xi, J.-Q., J.K. Kim, and E.F. Schubert, *Silica nanorod-array films with very low refractive indices.* Nano letters, 2005. **5**(7): p. 1385-1387.
83. Ting, C.-J., et al., *Fabrication of an antireflective polymer optical film with subwavelength structures using a roll-to-roll micro-replication process.* Journal of Micromechanics and Microengineering, 2008. **18**(7).
84. Xie, G., et al., *The fabrication of subwavelength anti-reflective nanostructures using a bio-template.* Nanotechnology, 2008. **19**(9): p. 095605.
85. Chao, Y.-C., et al., *Light scattering by nanostructured anti-reflection coatings.* Energy & Environmental Science, 2011. **4**(9): p. 3436-3441.
86. Hattori, H., *Anti‐reflection surface with particle coating deposited by electrostatic attraction.* Advanced Materials, 2001. **13**(1): p. 51-54.
87. Erbil, H.Y., et al., *Transformation of a simple plastic into a superhydrophobic surface.* Science, 2003. **299**(5611): p. 1377-1380.
88. Thomas, I.M., *Method for the preparation of porous silica antirelection coatings varying in refractive index from 1.22 to 1.44.* Applied optics, 1992.
89. Per Nostella, Arne Roosa, BjoÈrn Karlssonb, *optical and mechanical properties of sol-gel antireflective films for solar energy applications.* Thin Solid Films 1999. **170-175**.
90. Sun, C.-H., et al., *Templated fabrication of large area subwavelength antireflection gratings on silicon.* Applied Physics Letters, 2007. **91**(23): p. 231105.
91. Xiao, J., et al., *Reflectivity of porous-pyramids structured silicon surface.* Applied Surface Science, 2010. **257**(2): p. 472-475.
92. Raut, H.K., et al., *Fabrication of highly uniform and porous MgF2 anti-reflective coatings by polymer-based sol–gel processing on large-area glass substrates.* Nanotechnology, 2013. **24**(50): p. 505201.
93. Mahadik, D.B., R. Lakshmi, and H.C. Barshilia, *High performance single layer nano-porous antireflection coatings on glass by sol–gel process for solar energy applications.* Solar Energy Materials and Solar Cells, 2015. **140**: p. 61-68.
94. Moghal, J., et al., *High-performance, single-layer antireflective optical coatings comprising mesoporous silica nanoparticles.* ACS applied materials & interfaces, 2012. **4**(2): p. 854-859.
95. Rahman, A., et al., *Sub-50-nm self-assembled nanotextures for enhanced broadband antireflection in silicon solar cells.* Nature communications, 2015. **6**.
96. Lee, Y.-J., et al., *ZnO nanostructures as efficient antireflection layers in solar cells.* Nano letters, 2008. **8**(5): p. 1501-1505.
97. Hawker, C.J. and T.P. Russell, *Block copolymer lithography: Merging "bottom-up" with "top-down" processes.* MRS bulletin, 2005. **30**(12): p. 952-966.
98. Wydeven, T. and R. Kubacki, *Antireflection coating prepared by plasma polymerization of perfluorobutene-2.* Applied optics, 1976. **15**(1): p. 132-136.
99. Kaless, A., et al., *NANO-motheye antireflection pattern by plasma treatment of polymers.* Surface and Coatings Technology, 2005. **200**(1): p. 58-61.

100. Hadobas, K., et al., *Reflection properties of nanostructure-arrayed silicon surfaces.* Nanotechnology, 2000. **11**(3): p. 161.
101. Han, K.-S., et al., *Enhanced performance of solar cells with anti-reflection layer fabricated by nano-imprint lithography.* Solar Energy Materials and Solar Cells, 2011. **95**(1): p. 288-291.
102. Yan, X., et al., *Enhanced Omnidirectional Photovoltaic Performance of Solar Cells Using Multiple‐Discrete‐Layer Tailored‐and Low‐Refractive Index Anti‐Reflection Coatings.* Advanced Functional Materials, 2013. **23**(5): p. 583-590.
103. Askar, K., et al., *Self-assembled nanoparticle antiglare coatings.* Optics letters, 2012. **37**(21): p. 4380-4382.
104. Andersen, N.K. and R. Taboryski, *Multi-height structures in injection molded polymer.* Microelectronic Engineering, 2015. **141**: p. 211-214.
105. Guan, W.-S., H.-X. Huang, and A.-F. Chen, *Tuning 3D topography on biomimetic surface for efficient self-cleaning and microfluidic manipulation.* Journal of Micromechanics and Microengineering, 2015. **25**(3): p. 035001.
106. Chen, A.-F. and H.-X. Huang, *Rapid Fabrication of T-Shaped Micropillars on Polypropylene Surfaces with Robust Cassie–Baxter State for Quantitative Droplet Collection.* The Journal of Physical Chemistry C, 2016. **120**(3): p. 1556-1561.
107. Jiang, B.-y., et al., *Fabrication of nanopillar arrays by combining electroforming and injection molding.* The International Journal of Advanced Manufacturing Technology, 2016. **86**(5-8): p. 1319-1328.
108. Mielonen, K., M. Suvanto, and T. Pakkanen, *Curved hierarchically micro–micro structured polypropylene surfaces by injection molding.* Journal of Micromechanics and Microengineering, 2016. **27**(1): p. 015025.
109. Schneider, L., et al., *The influence of structure heights and opening angles of micro-and nanocones on the macroscopic surface wetting properties.* Scientific reports, 2016. **6**: p. 21400.
110. Reiter, G., *Unstable thin polymer films: rupture and dewetting processes.* Langmuir, 1993. **9**(5): p. 1344-1351.
111. Novak, B.M., *Hybrid nanocomposite materials—between inorganic glasses and organic polymers.* Advanced Materials, 1993. **5**(6): p. 422-433.
112. Allcock, H.R., *Inorganic—organic polymers.* Advanced Materials, 1994. **6**(2): p. 106-115.
113. Kickelbick, G., *Concepts for the incorporation of inorganic building blocks into organic polymers on a nanoscale.* Progress in polymer science, 2003. **28**(1): p. 83-114.
114. Mammeri, F., et al., *Mechanical properties of hybrid organic–inorganic materials.* Journal of Materials Chemistry, 2005. **15**(35-36): p. 3787-3811.
115. Wang, Y.-W. and W.-C. Chen, *Synthesis, properties, and anti-reflective applications of new colorless polyimide-inorganic hybrid optical materials.* Composites Science and Technology, 2010. **70**(5): p. 769-775.
116. *Reflection reducing coating having a gradually increasing index of refraction*. 1947, Google Patents.
117. Philippe F. Belleville, H.G.F., *Ammonia hardening of porous silica antireflective coatings.* Sol-Ge! Optics III, 1994.
118. Kourtakis, K., et al., *Novel thermal and photo curable anti-reflective coatings using fluoroelastomer nanocomposites and self-assembly of nanoparticles.* Journal of Coatings Technology and Research, 2016. **13**(5): p. 753-762.

119. Chen, C.-H., et al., *Scratch-resistant zeolite anti-reflective coating on glass for solar applications.* Solar Energy Materials and Solar Cells, 2011. **95**(7): p. 1694-1700.
120. Naik, S.P., A.S. Chiang, and R. Thompson, *Synthesis of zeolitic mesoporous materials by dry gel conversion under controlled humidity.* The Journal of Physical Chemistry B, 2003. **107**(29): p. 7006-7014.
121. Shu, G., et al., *Transparent zeolite films with regular surface patterns.* Advanced Materials, 2006. **18**(2): p. 185-189.
122. Marshall, K., et al. *Contamination resistant sol-gel coatings for high peak power laser applications*. in *published in the Proceedings of the OSA Topical Meeting on Optical Interference Coatings, Tucson, AZ*. 2007.
123. Marshall, K., et al. *Vapor-phase-deposited organosilane coatings as 'hardening'agents for high-peak-power laser optics*. in *Proc. SPIE*. 2007.
124. Wu, G., et al., *Strengthening mechanism of porous silica films derived by two-step catalysis.* Journal of Physics D: Applied Physics, 2001. **34**(9): p. 1301.
125. Lin, C.-Y., et al., *Self-assembled hemispherical nanowell arrays for superhydrophobic antireflection coatings.* Journal of colloid and interface science, 2017. **490**: p. 174-180.
126. Xu, Y., et al., *Sol–gel broadband anti-reflective single-layer silica films with high laser damage threshold.* Thin Solid Films, 2003. **440**(1-2): p. 180-183.
127. Bautista, M. and A. Morales, *Silica antireflective films on glass produced by the sol–gel method.* Solar energy materials and solar cells, 2003. **80**(2): p. 217-225.
128. Stillwagon, L., R. Larson, and G. Taylor, *Planarization of substrate topography by spin coating.* Journal of the Electrochemical Society, 1987. **134**(8): p. 2030-2037.
129. Wu, J.J., H.C. Wu, and C.Z. Zhao, *Low Cost Anti-Reflection Coating for Photovoltaic Application.* Advanced Materials Research, 2012. **538-541**: p. 414-418.
130. Arnou, P., et al., *Hydrazine-free solution-deposited CuIn (S, Se) 2 solar cells by spray deposition of metal chalcogenides.* ACS applied materials & interfaces, 2016. **8**(19): p. 11893-11897.
131. Porcel, C., et al., *Ultrathin coatings and (poly (glutamic acid)/polyallylamine) films deposited by continuous and simultaneous spraying.* Langmuir, 2005. **21**(2): p. 800-802.
132. Choy, K., *Chemical vapour deposition of coatings.* Progress in materials science, 2003. **48**(2): p. 57-170.
133. Yu, J., et al., *Improved opto-electronic properties of silicon heterojunction solar cells with SiO x /Tungsten-doped indium oxide double anti-reflective coatings.* Japanese Journal of Applied Physics, 2017. **56**(8S2).
134. Robbie, K. and M. Brett, *Sculptured thin films and glancing angle deposition: Growth mechanics and applications.* Journal of Vacuum Science & Technology A: Vacuum, Surfaces, and Films, 1997. **15**(3): p. 1460-1465.
135. Kennedy, S.R. and M.J. Brett, *Porous broadband antireflection coating by glancing angle deposition.* Applied optics, 2003. **42**(22): p. 4573-4579.
136. Hawkeye, M.M. and M.J. Brett, *Glancing angle deposition: fabrication, properties, and applications of micro-and nanostructured thin films.* Journal of Vacuum Science & Technology A: Vacuum, Surfaces, and Films, 2007. **25**(5): p. 1317-1335.
137. Barranco, A., et al., *Perspectives on oblique angle deposition of thin films: From fundamentals to devices.* Progress in Materials Science, 2016. **76**: p. 59-153.

138. Robbie, K., J. Sit, and M. Brett, *Advanced techniques for glancing angle deposition.* Journal of Vacuum Science & Technology B: Microelectronics and Nanometer Structures Processing, Measurement, and Phenomena, 1998. **16**(3): p. 1115-1122.
139. Tait, R., T. Smy, and M. Brett, *Modelling and characterization of columnar growth in evaporated films.* Thin Solid Films, 1993. **226**(2): p. 196-201.
140. Pearton, S., *High ion density dry etching of compound semiconductors.* Materials Science and Engineering: B, 1996. **40**(2-3): p. 101-118.
141. Jiao, F., et al., *Enhanced performance for solar cells with moth-eye structure fabricated by UV nanoimprint lithography.* Microelectronic Engineering, 2013. **103**: p. 126-130.
142. Li, J., et al. *Anti-reflective sub-wavelength structures at a wavelength of 441.6 nm for phase masks of near-field lithography*. in *Holography, Diffractive Optics, and Applications VII*. 2016. International Society for Optics and Photonics.
143. Zhang, J. and B. Yang, *Patterning colloidal crystals and nanostructure arrays by soft lithography.* Advanced Functional Materials, 2010. **20**(20): p. 3411-3424.
144. del Campo, A. and E. Arzt, *Fabrication approaches for generating complex micro-and nanopatterns on polymeric surfaces.* Chemical reviews, 2008. **108**(3): p. 911-945.
145. Acikgoz, C., et al., *Polymers in conventional and alternative lithography for the fabrication of nanostructures.* European Polymer Journal, 2011. **47**(11): p. 2033-2052.
146. Ahn, S.H. and L.J. Guo, *High‐speed roll‐to‐roll nanoimprint lithography on flexible plastic substrates.* Advanced materials, 2008. **20**(11): p. 2044-2049.
147. Cannavale, A., et al., *Multifunctional bioinspired sol-gel coatings for architectural glasses.* Building and Environment, 2010. **45**(5): p. 1233-1243.
148. Kanamori, Y., et al., *100 nm period silicon antireflection structures fabricated using a porous alumina membrane mask.* Applied Physics Letters, 2001. **78**(2): p. 142-143.
149. *House Windows - Self-cleaning*. Available from: http://uk.saint-gobain-glass.com/function/233/363/self-cleaning.
150. Cai, J. and L. Qi, *Recent advances in antireflective surfaces based on nanostructure arrays.* Materials Horizons, 2015. **2**(1): p. 37-53.
151. Ali, K., S.A. Khan, and M.M. Jafri, *Effect of double layer (SiO 2/TiO 2) anti-reflective coating on silicon solar cells.* Int. J. Electrochem. Sci, 2014. **9**: p. 7865-7874.
152. Nadeem, M., W. Ahmed, and M. Wasiq, *ZnS thin films–an overview.* Journal of research science, 2005. **16**: p. 105-112.
153. Bouhafs, D., et al., *Design and simulation of antireflection coating systems for optoelectronic devices: Application to silicon solar cells.* Solar Energy Materials and Solar Cells, 1998. **52**(1): p. 79-93.
154. Hecht, E., *Optics, 4th.* International edition, Addison-Wesley, San Francisco, 2002. **3**.
155. Olifierczuk, M. and J. Zielinski, *Significance of reflection reduction in a TN display for colour visualisation.* OPTOELECTRONICS REVIEW, 2002(1): p. 35-38.
156. Wada, T., et al., *Anti-Reflection (AR) Coating Meter*. 1999, SAE Technical Paper.
157. Rahman, I.A. and V. Padavettan, *Synthesis of silica nanoparticles by sol-gel: size-dependent properties, surface modification, and applications in silica-polymer nanocomposites—a review.* Journal of Nanomaterials, 2012. **2012**: p. 8.

158. Ciriminna, R., et al., *The sol–gel route to advanced silica-based materials and recent applications.* Chemical reviews, 2013. **113**(8): p. 6592-6620.
159. HARRINGTON, C.J.B.a.M.S., *SOL-GEL DERIVED ANTIREFLECTIVE COATINGS FOR SILICON.* Solar Energy Materials and Solar Cells, 1981. **5**.
160. Flory, P.J., *Principles of polymer chemistry*. 1953: Cornell University Press.
161. Tobler, D.J., S. Shaw, and L.G. Benning, *Quantification of initial steps of nucleation and growth of silica nanoparticles: An in-situ SAXS and DLS study.* Geochimica et Cosmochimica Acta, 2009. **73**(18): p. 5377-5393.
162. Rahman, I., et al., *An optimized sol–gel synthesis of stable primary equivalent silica particles.* Colloids and Surfaces A: Physicochemical and Engineering Aspects, 2007. **294**(1-3): p. 102-110.
163. Aelion, R., A. Loebel, and F. Eirich, *Hydrolysis of ethyl silicate.* Journal of the American Chemical Society, 1950. **72**(12): p. 5705-5712.
164. Matsoukas, T. and E. Gulari, *Monomer-addition growth with a slow initiation step: a growth model for silica particles from alkoxides.* Journal of Colloid and Interface Science, 1989. **132**(1): p. 13-21.
165. Bogush, G. and C. Zukoski Iv, *Studies of the kinetics of the precipitation of uniform silica particles through the hydrolysis and condensation of silicon alkoxides.* Journal of Colloid and Interface Science, 1991. **142**(1): p. 1-18.
166. Rao, K.S., et al., *A novel method for synthesis of silica nanoparticles.* Journal of colloid and interface science, 2005. **289**(1): p. 125-131.
167. Park, S.K., K. Do Kim, and H.T. Kim, *Preparation of silica nanoparticles: determination of the optimal synthesis conditions for small and uniform particles.* Colloids and Surfaces A: Physicochemical and Engineering Aspects, 2002. **197**(1-3): p. 7-17.
168. Brinker, C.J. and G.W. Scherer, *Sol-gel science: the physics and chemistry of sol-gel processing*. 2013: Academic press.
169. Princen, H., *In Surface and Colloid Science (ed. E. Matijevic), vol. 2*. 1969, Interscience.
170. Scherer, G.W., *Recent progress in drying of gels.* Journal of non-crystalline solids, 1992. **147**: p. 363-374.
171. Sing, K.S., *Reporting physisorption data for gas/solid systems with special reference to the determination of surface area and porosity (Recommendations 1984).* Pure and applied chemistry, 1985. **57**(4): p. 603-619.
172. Brunauer, S., P.H. Emmett, and E. Teller, *Adsorption of gases in multimolecular layers.* Journal of the American chemical society, 1938. **60**(2): p. 309-319.
173. Groen, J.C., L.A. Peffer, and J. Pérez-Ramírez, *Pore size determination in modified micro-and mesoporous materials. Pitfalls and limitations in gas adsorption data analysis.* Microporous and mesoporous materials, 2003. **60**(1-3): p. 1-17.
174. Sing, K.S. and R.T. Williams, *Physisorption hysteresis loops and the characterization of nanoporous materials.* Adsorption Science & Technology, 2004. **22**(10): p. 773-782.
175. Puziy, A., et al., *Synthetic carbons activated with phosphoric acid: I. Surface chemistry and ion binding properties.* Carbon, 2002. **40**(9): p. 1493-1505.
176. Bailey, A., et al., *Low pressure hysteresis in the adsorption of organic vapours by porous carbons.* Transactions of the Faraday Society, 1971. **67**: p. 231-243.
177. Silvestre-Albero, A.M., et al., *Low-pressure hysteresis in adsorption: an artifact?* The Journal of Physical Chemistry C, 2012. **116**(31): p. 16652-16655.

178. Kruk, M., M. Jaroniec, and A. Sayari, *Application of large pore MCM-41 molecular sieves to improve pore size analysis using nitrogen adsorption measurements.* Langmuir, 1997. **13**(23): p. 6267-6273.
179. Kruk, M. and M. Jaroniec, *Gas adsorption characterization of ordered organic–inorganic nanocomposite materials.* Chemistry of materials, 2001. **13**(10): p. 3169-3183.
180. Buckley, A. and M. Greenblatt, *The sol-gel preparation of silica gels.* journal of chemical education, 1994. **71**(7): p. 599.
181. Brinker, C.J. and G.W. Scherer, *Sol→gel→glass: I. Gelation and gel structure.* Journal of Non-Crystalline Solids, 1985. **70**(3): p. 301-322.
182. Zarzycki, J., M. Prassas, and J. Phalippou, *Synthesis of glasses from gels: the problem of monolithic gels.* Journal of materials science, 1982. **17**(11): p. 3371-3379.
183. Levit, A.B. and R.L. Rowell, *Time dependence of the size distribution, number concentration and surface area in La Mer sulfur sols.* Journal of Colloid and Interface Science, 1975. **50**(1): p. 162-169.
184. Iler, R., *The Chemistry of Silica: solubility, polymerization, colloid and surface and surface properties, and biochemistry.* 1979.
185. Harris, M.T., R.R. Brunson, and C.H. Byers, *The base-catalyzed hydrolysis and condensation reactions of dilute and concentrated TEOS solutions.* Journal of Non-Crystalline Solids, 1990. **121**(1-3): p. 397-403.
186. Van Blaaderen, A., J. Van Geest, and A. Vrij, *Monodisperse colloidal silica spheres from tetraalkoxysilanes: particle formation and growth mechanism.* Journal of colloid and interface science, 1992. **154**(2): p. 481-501.
187. Zhang, J., F. Huang, and Z. Lin, *Progress of nanocrystalline growth kinetics based on oriented attachment.* Nanoscale, 2010. **2**(1): p. 18-34.
188. Takahashi, R., K. Nakanishi, and N. Soga, *Insight on Structural Change in Sol–Gel-Derived Silica Gel with Aging under Basic Conditions for Mesopore Control.* Journal of sol-gel science and technology, 2005. **33**(2): p. 159-167.
189. Lazaro, A., et al., *The influence of process conditions and Ostwald ripening on the specific surface area of olivine nano-silica.* Microporous and Mesoporous Materials, 2013. **181**: p. 254-261.
190. Matsoukas, T. and E. Gulari, *Dynamics of growth of silica particles from ammonia-catalyzed hydrolysis of tetra-ethyl-orthosilicate.* Journal of colloid and interface science, 1988. **124**(1): p. 252-261.
191. Bogush, G. and C. Zukoski Iv, *Uniform silica particle precipitation: an aggregative growth model.* Journal of colloid and interface science, 1991. **142**(1): p. 19-34.
192. Glunz, S.W. and F. Feldmann, *SiO2 surface passivation layers–a key technology for silicon solar cells.* Solar Energy Materials and Solar Cells, 2018. **185**: p. 260-269.
193. Aberle, A.G., *Surface passivation of crystalline silicon solar cells: a review.* Progress in Photovoltaics: Research and Applications, 2000. **8**(5): p. 473-487.
194. Tompkins, H. and E.A. Irene, *Handbook of ellipsometry*. 2005: William Andrew.
195. Aspnes, D., J. Theeten, and F. Hottier, *Investigation of effective-medium models of microscopic surface roughness by spectroscopic ellipsometry.* Physical Review B, 1979. **20**(8): p. 3292.
196. Bruggeman, V.D., *Berechnung verschiedener physikalischer Konstanten von heterogenen Substanzen. I. Dielektrizitätskonstanten und Leitfähigkeiten der*

Mischkörper aus isotropen Substanzen. Annalen der physik, 1935. **416**(7): p. 636-664.
197. Maxwell-Garnett, J. *Philos. Trans. R. Soc. London*. in *Ser. A*. 1904.
198. Garnett, J.M., *XII. Colours in metal glasses and in metallic films.* Philosophical Transactions of the Royal Society of London. Series A, Containing Papers of a Mathematical or Physical Character, 1904. **203**(359-371): p. 385-420.
199. Braun, M.M. and L. Pilon, *Effective optical properties of non-absorbing nanoporous thin films.* Thin Solid Films, 2006. **496**(2): p. 505-514.
200. Jellison Jr, G., et al., *Spectroscopic ellipsometry of thin film and bulk anatase (TiO 2).* Journal of Applied Physics, 2003. **93**(12): p. 9537-9541.
201. Richards, B., *Single-material TiO2 double-layer antireflection coatings.* Solar Energy Materials and Solar Cells, 2003. **79**(3): p. 369-390.
202. Synowicki, R., *Suppression of backside reflections from transparent substrates.* physica status solidi c, 2008. **5**(5): p. 1085-1088.
203. Herzinger, C., et al., *Ellipsometric determination of optical constants for silicon and thermally grown silicon dioxide via a multi-sample, multi-wavelength, multi-angle investigation.* Journal of Applied Physics, 1998. **83**(6): p. 3323-3336.
204. Khardani, M., M. Bouaïcha, and B. Bessaïs, *Bruggeman effective medium approach for modelling optical properties of porous silicon: comparison with experiment.* physica status solidi c, 2007. **4**(6): p. 1986-1990.
205. Li, Y., L. Li, and J. Sun, *Bioinspired self‐healing superhydrophobic coatings.* Angewandte Chemie, 2010. **122**(35): p. 6265-6269.
206. Bruggeman, D., *Dielectric constant and conductivity of mixtures of isotropic materials.* Ann. Phys.(Leipzig), 1935. **24**: p. 636-679.
207. Brinker, C.J., *Dip coating*, in *Chemical Solution Deposition of Functional Oxide Thin Films*. 2013, Springer. p. 233-261.
208. Dimitrov, A.S. and K. Nagayama, *Continuous convective assembling of fine particles into two-dimensional arrays on solid surfaces.* Langmuir, 1996. **12**(5): p. 1303-1311.
209. Faustini, M., et al., *Preparation of sol− gel films by dip-coating in extreme conditions.* The Journal of Physical Chemistry C, 2010. **114**(17): p. 7637-7645.
210. Landau, L. and B. Levich, *Dragging of a liquid by a moving plate*, in *Dynamics of Curved Fronts*. 1988, Elsevier. p. 141-153.
211. Lockwood, D.J., *Rayleigh and Mie Scattering*, in *Encyclopedia of Color Science and Technology*, M.R. Luo, Editor. 2016, Springer New York: New York, NY. p. 1097-1107.
212. Hulst, H.C. and H.C. van de Hulst, *Light scattering by small particles*. 1981: Courier Corporation.
213. Karunakaran, R.G., et al., *Highly transparent superhydrophobic surfaces from the coassembly of nanoparticles (⩽ 100 nm).* Langmuir, 2011. **27**(8): p. 4594-4602.
214. Li, F., et al., *A facile, multifunctional, transparent, and superhydrophobic coating based on a nanoscale porous structure spontaneously assembled from branched silica nanoparticles.* Advanced Materials Interfaces, 2015. **2**(13): p. 1500201.
215. Penndorf, R., *Angular mie scattering.* JOSA, 1962. **52**(4): p. 402-408.
216. Saleh, B.E. and M.C. Teich, *Fundamentals of photonics*. 2019: John Wiley & Sons.
217. Jorgensen, G.J., et al. *Durability testing of antireflection coatings for solar applications*. in *Solar Optical Materials XVI*. 1999. International Society for Optics and Photonics.

218. McSkimin, H., *Measurement of elastic constants at low temperatures by means of ultrasonic waves–data for silicon and germanium single crystals, and for fused silica.* Journal of applied physics, 1953. **24**(8): p. 988-997.
219. Parrill, T., *Heat treatment of spun-on acid-catalyzed sol-gel silica films.* Journal of materials research, 1994. **9**(3): p. 723-730.
220. Wang, H.-P., et al., *Periodic Si nanopillar arrays fabricated by colloidal lithography and catalytic etching for broadband and omnidirectional elimination of Fresnel reflection.* Langmuir, 2010. **26**(15): p. 12855-12858.

Supporting information

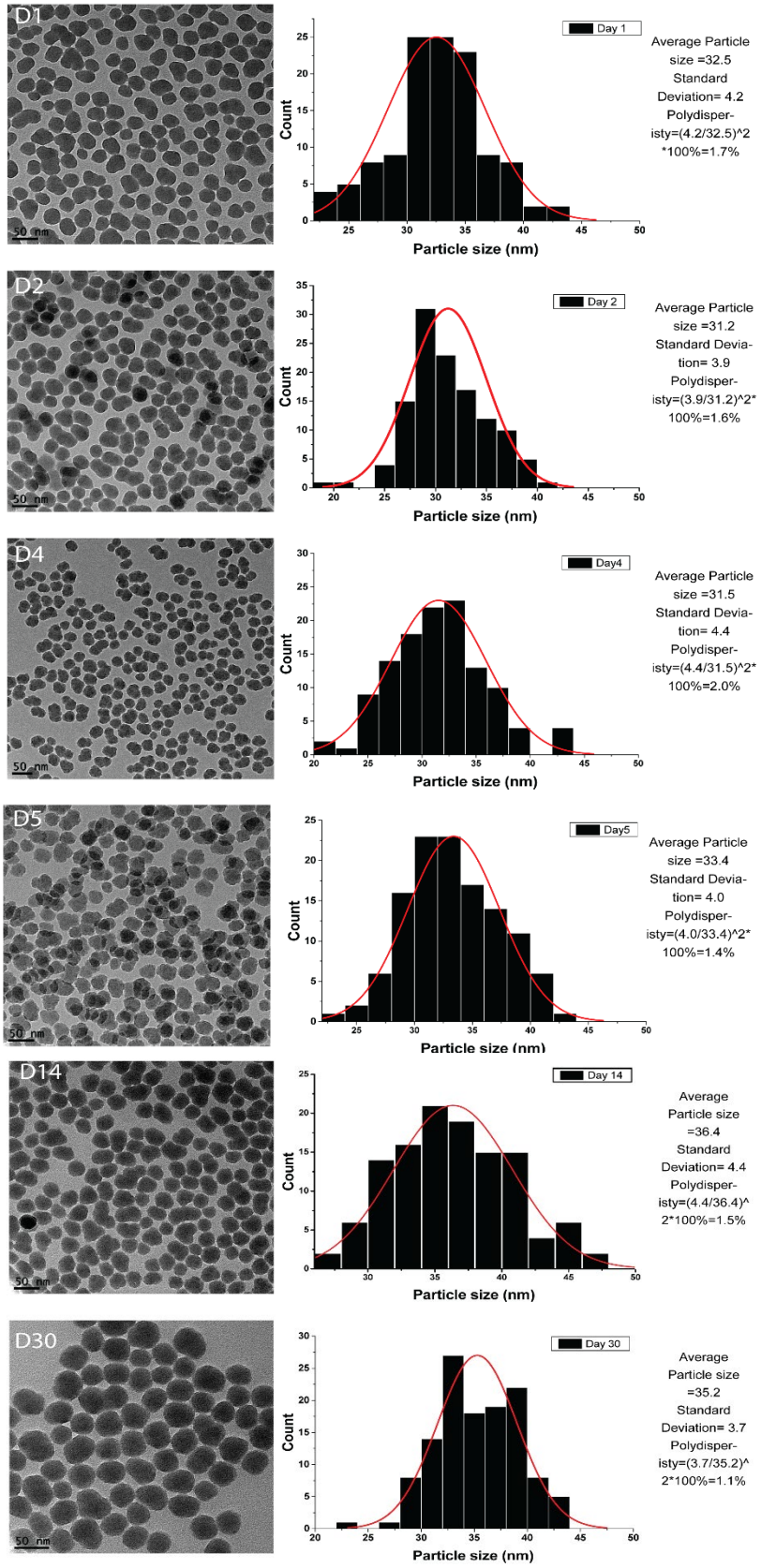

Figure S 1. The TEM images of sol 6 for different aging days and corresponding diameters distributions by ImageJ and origin pro 2015.